Taking shape: The path to myosin activation in the *Drosophila* ventral furrow

By

Natalie C. Heer
A.B., Harvard University (2012)

Submitted to the Department of Biology
in Partial Fulfillment of the Requirements for the Degree of

Doctor of Philosophy
at the
Massachusetts Institute of Technology

February 2018

Signature of Author: Signature redacted

Department of Biology
December 18, 2017

Certified by: Signature redacted

Adam C. Martin
Associate Professor of Biology
Thesis Advisor

Accepted by: Signature redacted

Amy E. Keating
Professor of Biology
Chair, Biology Graduate Committee

Taking shape: The path to myosin activation in the *Drosophila* ventral furrow

by

Natalie C. Heer

Submitted to the Department of Biology on December 31st, 2017, in Partial Fulfillment of the Requirements for the Degree of Doctor of Philosophy in Biology

Abstract

Creating biological form requires the generation of forces to rearrange tissues, as well as the patterning and organizational control of those forces to create the correct shapes. Force generation by actomyosin networks is a major driver of morphogenesis across many systems. The organization of actomyosin networks across multiple length scales is critical in generating biological form, including the *Drosophila melanogaster* ventral furrow. Using quantitative microscopy to measure the pattern of transcription, signaling, myosin activation, and cell shape in the *Drosophila* mesoderm, I found that cells within the ventral domain accumulate different amounts of active apical non-muscle myosin 2 depending on their distance from the ventral midline. This gradient in active myosin depends on a newly quantified gradient in upstream signaling proteins, including the transcription factor Twist. Experimental broadening of the myosin domain *in vivo* disrupts tissue curvature where active myosin is uniform. From this data, I argue that apical contractility gradients are important for tissue folding. Finally, I found that the gradient in active myosin is shaped by inhibitors of RhoA signaling downstream of the Twist gradient. This work improves our of understanding how actomyosin activity at the tissue level in the *Drosophila* ventral furrow is organized and how that organization impacts biological form.

Thesis Supervisor: Adam C. Martin
Title: Associate Professor of Biology

Acknowledgments

I would like to thank my advisor, Professor Adam Martin, for being an excellent mentor. Thank you for all of your patience with me during my graduate career, and for always being generous with your time and encouragement. Your excitement about my science was always extremely encouraging. I always left my meetings with you feeling more inspired and motivated. I am also grateful for your attention to my scientific and career growth; you always made sure that I was seeking out opportunities that would lead to my success. I could not have asked for a better advisor in graduate school.

Thank you as well to my thesis committee members, Professors Bob Horvitz and Piyush Gupta, for your excellent advice and encouragement. Thank you for providing critical feedback on my project over the years, and for pushing me to be the best scientist I could be. I always appreciated the support you gave me, and the care you took to make sure I was on the right track. Thank you as well to Professor Angela DePace for joining my committee and for your time and feedback.

Thank you to the members of the Dunkel Group at MIT, Professor Jörn Dunkel, Dr. Norbert Stoop, and Pearson Miller. Collaborating with you has been a fantastic experience. The opportunity to have such close collaboration between experimental and theoretical groups was truly special.

Thank you to current and former members of the Martin Lab. You have helped to make my graduate experience fun as well as science-filled. Thank you to Mike Tworoger for your endless patience in teaching me scientific techniques, for being there when I needed help, and for all of your life wisdom. Thank you to Dr. Soline Chanet for being an excellent rotation mentor, a superb experimentalist, and for providing me with a stepping stone to do the research presented in this work. Thank you to Frank Mason for your thoughtful advice and help with my work. Thank you to Dr. Jeanne Jodoin for being an excellent role model; I learned so much from you about how to get stuff done, which is a critical skill for a graduate student. Thank you to Drs. Claudia Vasquez, Mimi Xie, and Jonathan Coravos for being my role models, for blazing the trail for future Martin Lab graduate students, and for always being available to answer my questions, even after your graduated. Finally, I would like to thank current Martin Lab members for continuing to create a supportive and creative environment.

Thank you to the MIT Biology community, and especially to my graduate classmates, for your support and for going through this process with me. I learned so much from all of you. Thank you also to my friends outside of MIT for keeping me involved and engaged in activities and hobbies outside of grad school, and for always listening to me.

Thank you to my parents, Jody Copp and John Heer, for setting me on the path to become a scientist. I would not be where I am today if not for my early lessons on electric circuits and human genetics drawn on napkins at the dinner table. And thank you to my sister Julia, who I knew would always be there for me and who I never needed to impress.

Finally, thank you to my partner, Jeremy Cushman. You were my best resource in graduate school both for life and scientific advice. Thank you for the countless hours you spent disabusing me of my self-doubt and catching my grammar mistakes. Thank you for your love and support. I could not have done this without you.

Table of Contents

Chapter 1. Tension, Contraction, and Tissue Morphogenesis

Natalie C. Heer and Adam C. Martin

Portions of this chapter were published as: Heer, N. C. & Martin, A. C. Tension, contraction, and tissue morphogenesis. *Development* **144**, 4249–4260 (2017). The published paper was conceived and edited jointly by NCH and ACM. ACM was primarily responsible for drafting most parts of section 1.2. NCH was primarily responsible for drafting all other sections.

One hundred years ago, in his seminal work *On Growth and Form*, D'Arcy Wentworth Thompson proposed that an organism's form is a "diagram of the forces" that have acted and continue to act upon it (Thompson, 1917). When Thompson was writing, what those forces were and how they were generated was a mystery, but Thompson's work has inspired generations of biologists to think quantitatively about the creation of biological form. The discovery of the types of forces influencing morphogenesis has relied on the inference of force from individual cell shapes or from direct measurements of force through manipulation of the tissue. A number of factors have been implicated in generating these types of forces. In particular, genetic screens identifying mutations that disrupt morphogenesis have revealed that a critical driver of morphogenesis is the actomyosin cytoskeleton, which is composed of actin (that can polymerize into filaments) and myosin (a molecular motor) that together compose networks that generate contractile force (Quintin et al., 2008). The actomyosin cytoskeleton generates the force required to drive ventral furrow formation in the *Drosophila* embryo.

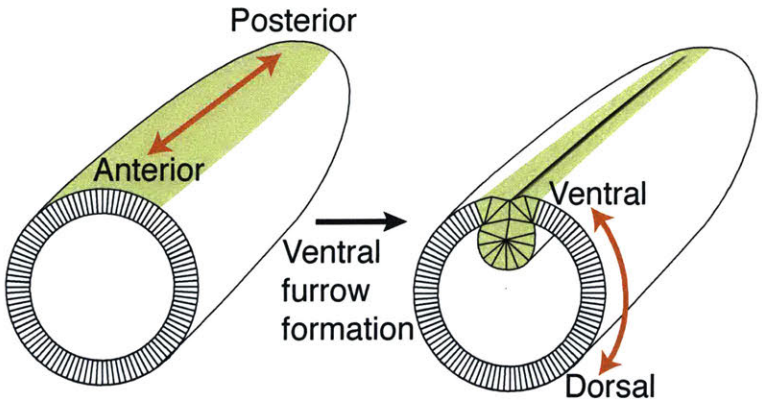

Figure 1.1: Diagram of a *Drosophila* embryo before and after ventral furrow formation. The anterior portion of the embryo is cut away to show the cross-sectional view. The ventral domain of the embryo is colored in green. The anterior-posterior and dorsal-ventral axes are marked.

Drosophila ventral furrow formation is one of the first major tissue rearrangements in the embryo. As part of *Drosophila* gastrulation, it is the folding event along the anterior-posterior (long) axis of the embryo that results in the internalization of the mesodermal precursor cells (**Fig. 1.1**) (Leptin and Grunewald, 1990). As an overview, the first section of the review will discuss how contractile forces are generated, from the molecular to the tissue level. The second section will discuss examples of tissue morphogenesis that illustrate how patterns of contractility sculpt tissues, from single cell ingression to compartment boundary maintenance. The final section will present an overview of the previous understanding of the patterning of the *Drosophila* embryo that is required for ventral furrow formation.

1.1. Contractile force generation: From molecules to tissues

While D'Arcy Thompson dismissed "the many theories and speculations which would connect the phenomena of surface-tension with contractility [and] muscular movement" (Thompson, 1917), we now understand that this connection is paramount. However, the tension at cell surfaces is not driven by surface tension, as Thompson understood it, but by tension in the cortical actin layer[1]. Below, I begin with an overview of the molecular components of contractile

[1] When D'Arcy Thompson referred to "surface tension" at cell boundaries he equated it to the

networks that underlie this tension. I then discuss advances in our understanding of the subcellular organization of these networks and how they generate contractile force, thus increasing cortical tension. Next, I discuss how these networks are connected between cells and the role these networks play in shaping the mechanical properties of the tissue.

To illustrate the fundamental mechanisms of actomyosin based contractility, I focus on two systems of actomyosin based contractile systems. Most obviously, the *Drosophila* ventral furrow, because in addition to being the system in which the experiments in this thesis were performed, it has also been the system instrumental for recent advances in our understanding of contractility generated by non-muscle, actomyosin networks in multicellular organisms. On the cellular level in the *Drosophila* ventral furrow, actomyosin contractility drives the constriction of the apical side of polarized epithelial cells. Fission yeast is the second system which has significantly contributed to recent advances in our understanding of actomyosin based force generation on the molecular level. In fission yeast cytokinesis, a contractile actomyosin ring assembles at the equator of the yeast cell and constricts, separating the daughter cells. The fission yeast contractile ring is arguably the best-understood model of non-muscle actomyosin-based contractile force generation.

---

surface tension at an air-liquid or liquid-liquid interface. This surface tension is driven by the minimization of the interface to realize the most energetically preferable arrangement of molecules in a liquid drop. While the plasma membrane does have an inherent surface tension, the forces we discuss in this review are primarily, although not exclusively, the result of forces generated by an actomyosin network in the cell cortex underlying the plasma membrane. Going forward we will refer to this form of "effective surface tension" as cortical tension. This is also consistent with work showing that the contribution of membrane tension to the effective surface tension is often negligible (Krens et al., 2017, Maitre et al., 2012, Steinberg, 1963). In the systems we discuss, relative cortical tension can be measured without determining the source of the stress in the tissue and often without generating an absolute measurement of force. Because cortical tension and surface tension drive similar changes in shape, many of the *in silico* models discussed here model cortical tension as surface or line tension.

1.1.1. Molecular level: the importance of myosin motor function

Our understanding of the role of physical forces in generating organism and tissue form is predicated on our understanding the molecular mechanisms that convert chemical energy to kinetic energy. There are many mechanisms for biological systems to generate force, including more than one mechanism to generate contractile force (Vale and Milligan, 2000). There is evidence that all of the systems presented in this work generate force through the actomyosin cytoskeleton. Actin and myosin are the two primary components of the actomyosin cytoskeleton, both of which convert chemical energy to force generation. Actin networks are regulated by proteins that control the rate of polymerization and depolymerization of individual actin filaments (F-actin). In addition, a host of other proteins control actin network architecture by crosslinking F-actin together, by bundling actin filaments into cables, and by regulating the stability or formation of dendritic branches that are formed by the Arp2/3 complex (Pollard, 2007). Myosin (non-muscle myosin 2 in this case) is primarily regulated through phosphorylation of the myosin regulatory light chain, which controls motor activity and the formation of bipolar filaments important for contractile function (Heissler and Sellers, 2016). Note that some myosin 2 proteins, such as that in fission yeast, do not form a typical minifilament, but form other types of oligomers (Laplante et al., 2016). Regulation of cell contractility through transcriptional regulation of myosin and actin regulators has also been observed (Calvo et al., 2013; Pollard, 2007). Mechanisms of actomyosin based contraction can be roughly classified as being dependent on or independent of myosin 2 motor activity. Evidence suggests that both such modes of contractility exist in cells (Ma et al., 2012; Vicente-Manzanares et al., 2007). Thus, one or both modes could be important for tissue-level forces.

The classical model of contractile force generation has myosin 2 functioning as a motor,

converting energy from ATP hydrolysis into directed motion and cytoskeletal network contraction. This contractile model relies on active myosin 2 forming higher-order structures, or oligomers (Fenix et al., 2016; Laplante et al., 2016). The most common type of oligomer is a bipolar myosin filament whose formation is regulated by phosphorylation of the myosin 2 regulatory light chain by various kinases (e.g., Rho Kinase, ROCK and Citron kinase) (Fig. 1.2A) (Amano et al., 1996; Heissler and Sellers, 2014; Yamashiro et al., 2003). In bipolar myosin filaments, motor heads at both ends of the myosin filament are able to interact with and walk along distinct actin filaments (F-actin) towards the barbed or plus end (Fig. 1.2A, green arrows). In striated muscle, a stereotyped version of this interaction slides antiparallel F-actin networks together (Huxley and Hanson, 1954). One prediction of this model is that the speed of contraction is correlated with the ATPase activity of the motor (and more specifically ADP release), which has been observed experimentally when compared to both muscle contraction rates and *in vitro* motility assays (Barany, 1967; Yengo et al., 2012). This prediction is important for distinguishing between the motor dependent and independent models of contractility.

Alternatively, myosin 2 and other proteins can function as crosslinkers, allowing depolymerization of actin filaments to drive contraction (Fig. 1.2B) (Sun et al., 2010). This type of myosin motor-independent contraction has been shown to operate in ring closure for cytokinetic events in several organisms (Ma et al., 2012; Mendes Pinto et al., 2012; Xue and Sokac, 2016). In the early *Drosophila* embryo, there is a mass ring-closure event during which all cells are separated from a central yolk compartment. Interestingly, this process occurs in two stages, one of which depends on myosin motor activity, and another that is myosin-independent and depends on actin depolymerization (Xue and Sokac, 2016). This suggests that these two mechanisms could be used individually or in combination to effect contraction.

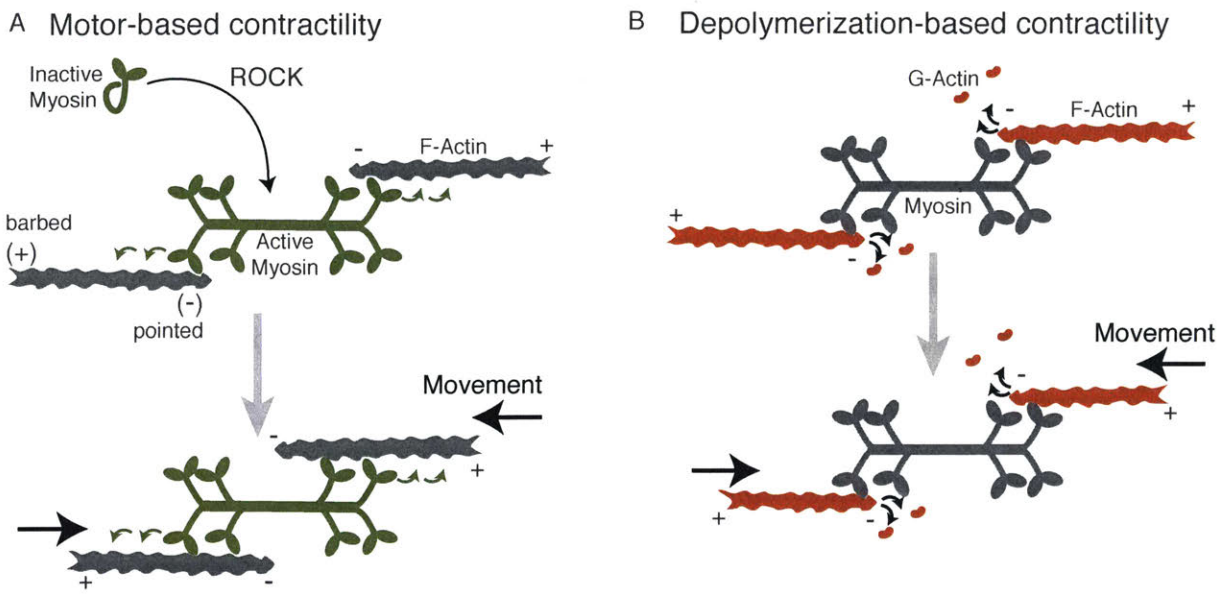

Figure 1.2: Diagram of the two models by which networks of actin and myosin can generate contractile forces. (A) Myosin is activated by ROCK and polymerizes into a bipolar filament (green). Contractility (black arrows) is generated by the motor activity of myosin as it walks along antiparallel actin filaments (green arrows). (B) Contractility (black arrows) is driven by F-actin depolymerization into G-actin (red). In this case, myosin (gray) would act as one of potentially many crosslinkers between neighboring filaments. Plus and minus ends of the F-actin filaments are denoted. Note that here, for illustrative purposes, we denote actin subunits depolymerizing from the filament end, but in reality proteins that mediate depolymerization (i.e., Cofilin) cause filament severing (Andrianantoandro and Pollard, 2006).

It is difficult to determine whether contractile events *in vivo* depend on the motor function of myosin 2. This is because it is difficult to distinguish whether myosin motor or crosslinking function is required. Common methods to inhibit myosin 2, such as Rho-Kinase (ROCK) inhibition, disrupt both motor and crosslinking functions because they prevent phosphorylation and, thus, the conformational changes that are required for bipolar filament assembly (Craig et al., 1983). Another myosin inhibitor, blebbistatin locks the actin-binding domain of myosin 2 in a weak actin binding state, which has similar affinity to actin as unphosphorylated myosin even though the myosin is filamentous (Kovacs et al., 2004; Ramamurthy et al., 2004). Therefore, testing for myosin's motor activity requires mutants that only disrupt this activity. For example, mutants of the myosin heavy chain that are known to

disrupt motor activity have been used for this purpose (Ma et al., 2012; Vicente-Manzanares et al., 2007). In addition, some mutations in the *Drosophila* myosin regulatory light chain decrease motor activity without overtly affecting bipolar filament formation (Vasquez et al., 2016).

1.1.2. Cell level: the importance of actomyosin network organization

In striated muscle, contraction relies on a stereotypic antiparallel organization of F-actin arrays within a sarcomere, with bipolar myosin filaments in the center (Fig. 1.2A). However, models of contraction with purified components demonstrate that unstructured networks can also contract, and this is thought to correspond to the situation in the cortex of smooth muscle and nonmuscle cells (Koenderink et al., 2009; Murrell and Gardel, 2012; Soares e Silva et al., 2011). Here we discuss findings that demonstrate the importance of network organization for contracting cells, even in what were previously considered unstructured networks. The reconstitution of contractility with purified components and defined F-actin architectures has shown that maximizing the antiparallel organization of actin networks enhances myosin-based constriction velocity (Reymann et al., 2012). This suggests that antiparallel F-actin networks are more efficient at generating contractile forces. Further supporting the importance of actin network organization in producing contractile force, modeling of fission yeast cytokinesis finds that actomyosin rings in which myosin is oriented nearer to F-actin minus ends—a more sarcomere-like organization—are able to generate higher tension (Fig. 1.3A, see inset) (Stachowiak et al., 2014). Though the organization of the actomyosin network is important for contractile force generation in these *in vitro* and *in silico* experiments, it is often unclear whether such organization exists and how it is generated in nonmuscle tissues.

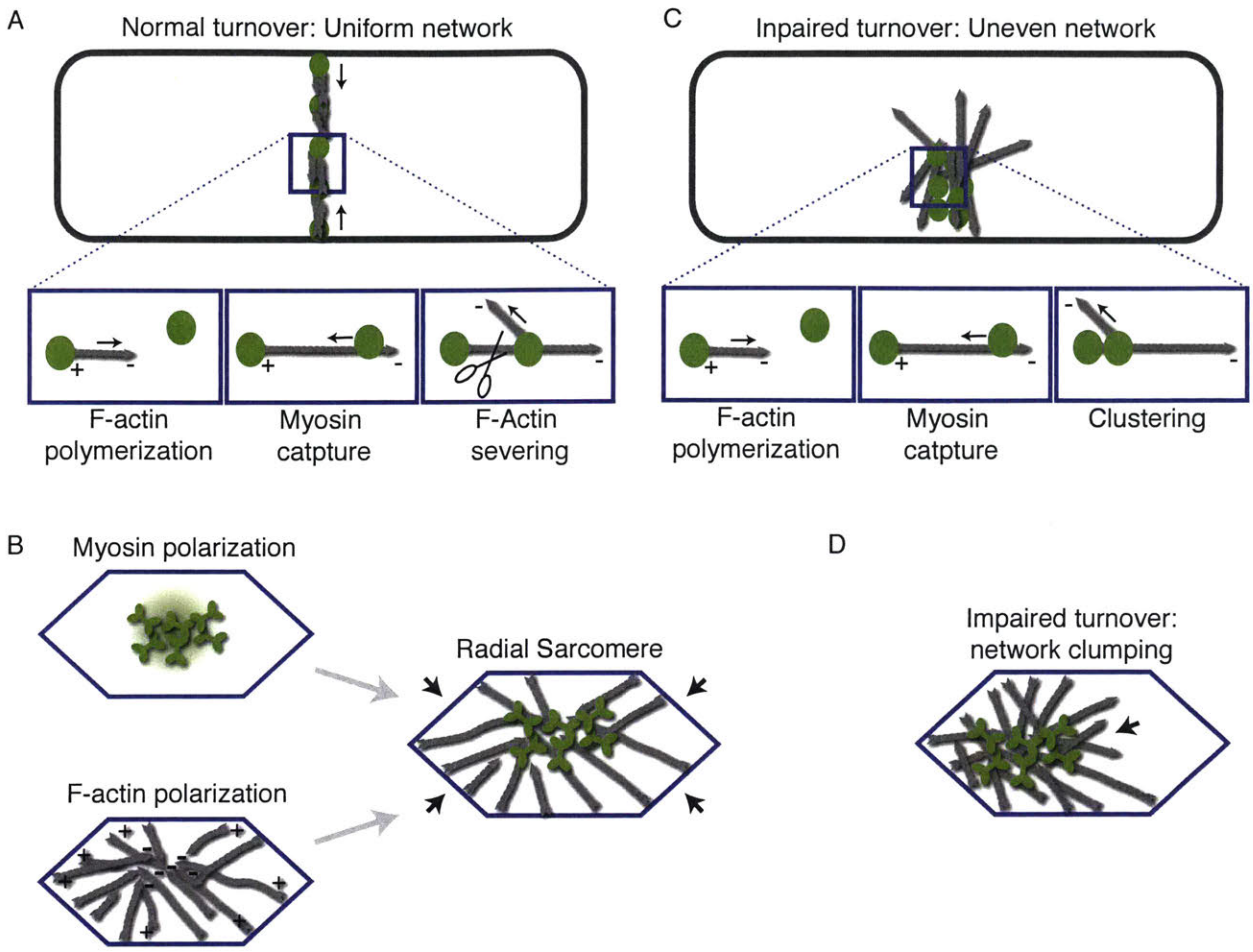

Figure 1.3: Diagram of actomyosin network organization in *Drosophila* ventral furrow cells and fission yeast contractile ring. (A) Diagram of the organization of a normal contractile ring. Inset shows actin polymerizing from a node structure that contains myosin and an F-actin elongating formin, capturing a second myosin node, and being severed to maintain the correct density of actin. F-actin is in gray and myosin oligomers are in green. There is not a net polarity to this network, but within the network myosin captures polymerizing F-actin near the minus end and pulls on it. **(B)** The actomyosin network in the *Drosophila* ventral furrow is organized in a manner that resembles a sarcomere, but is radially arranged. The myosin (green) is activated at the center of the apical cell surface. Actin organization is depicted in gray. The organization of each component is depicted separately and together. **(C)** Diagram of a contractile ring with actin turnover inhibited. F-actin is in gray and myosin-containing nodes are in green. Myosin nodes aggregate because they are never detached from each other. (D) Diagram of the actin network in a *Drosophila* ventral furrow cell that has impaired turnover. The network aggregates and separates from junctions on one side of the cell.

Epithelia have properties that might enable organized actomyosin networks to form at a cellular level as has been found to be the case in the *Drosophila* embryo. Adherens junctions around the apical circumference of epithelial cells serve as platforms in which F-actin is both assembled and anchored (Michael and Yap, 2013). In ventral furrow cells of the *Drosophila*

embryo, F-actin plus ends are enriched at the adherens junctions at the boundaries of the apical surface and F-actin minus ends are enriched in the apical center (Fig. 1.3B) (Coravos and Martin, 2016). In many contracting epithelial cells, including salivary gland cells, amnioserosa, and follicle cells, active RhoA, ROCK, and myosin have been found to accumulate at the center of the apical or basal cortex (referred to as medial myosin accumulation) (Chung et al., 2017; Coravos and Martin, 2016; Mason et al., 2013; Mason et al., 2016; Qin et al., 2017). Thus, ventral furrow cells, and possibly these other cell types, have a cytoskeletal organization that resembles a muscle sarcomere, except that it is radially arranged. Disrupting this organized structure by activating myosin across the entire apical surface inhibits apical constriction, suggesting that this network organization is critical for contraction (Coravos and Martin, 2016). Consistent with a sarcomere-like (i.e., motor-dependent) mode of constriction in ventral furrow cells, mutants in the myosin regulatory light chain that decrease myosin's motor/ATPase activity result in a proportionate decrease in apical constriction and tissue folding rate (Vasquez et al., 2016). Thus, in some cases, non-muscle cells require spatially organized myosin motor activity to contract cells and tissues. Future research is needed to determine whether mammalian nonmuscle cell types also have this type of cytoskeletal organization or if this is an adaptation to support the rapid embryonic development of insects or other invertebrates.

1.1.3. Transmitting force between cells: the importance of actin network turnover

The creation of many biological forms requires the propagation of forces across tissues. This is seen in the morphogenesis of the *Drosophila* pupal wing, the folding of the neural tube, and the formation of the *Drosophila* ventral furrow. In the pupal wing, the tissue must be anchored on the distal end to the extracellular matrix and on the other to the wing hinge, which

contracts, for the epithelium to expand correctly (Aigouy et al., 2010). This suggests that forces are propagated across the full length of the wing as hinge contraction stretches the wing into shape (Etournay et al., 2015; Ray et al., 2015). Recent work on mammalian neural tube closure has also shown that forces are propagated across the neuroepithelium as it folds (Galea et al., 2017). This propagation involves supracellular actomyosin cables, which in vertebrate gastrulation form across the cell surface and in neurulation at cell-cell interfaces. These supracellular cables are linked through intercellular adhesions to form a larger network (Galea et al., 2017; Pfister et al., 2016). The folding of the neural tube is a particularly important example given that defects in neural tube closure result in a serious and relatively common birth defect, spina bifida (Wallingford et al., 2013). We speculate that the following discussion will be relevant to understanding causes of spina bifida.

For tissues to transmit forces, the individual cells that make up the tissue must be mechanically linked. In epithelial tissues this often occurs at adherens junctions, which contain the self-binding adhesion receptor E-Cadherin (Lecuit and Yap, 2015). However, cells in some tissue types can be connected through an integrin-ECM-integrin attachment (e.g., a myotendinous junction) (Goody et al., 2015). In addition to maintaining extracellular attachment, to transmit force and maintain tissue integrity, the junctional proteins in the cytoplasm need to be robustly coupled to the actomyosin cortex as the cortex constricts and/or remodels (Roh-Johnson et al., 2012). In the case of myosin-motor-driven contraction, this attachment is thought to depend on actin-adhesion receptor interactions through adaptor proteins such as α-catenin and β-catenin (Ladoux et al., 2015). In addition, other F-actin-binding proteins such as vinculin and afadin can also be recruited to intercellular junctions and are important for junction functionality (Choi et al., 2016; Huveneers et al., 2012). Interestingly,

in less complex metazoans, such as the sea anemone, the interaction between α-catenin and F-actin is constitutive (Clarke et al., 2016). However, in mammals strong binding between α-catenin and F-actin depends on applied force, suggesting a catch-bond like behavior (Buckley et al., 2014). In an *in vitro* system, actin binding by *G. gallus* vinculin responds asymmetrically to applied force (i.e. force towards the F-actin minus end results in a maximally stable bond) (Huang et al., 2017). Such an asymmetry could result in a long-range polarity in the actin cytoskeletal network. Intriguingly, this asymmetry could help drive the sarcomere-like configuration of the actin network observed in ventral furrow cells (Fig. 1.3B). The additional layer of feedback in the mammalian system impacts the ability of cells to transmit forces and should be taken into account when analyzing these systems.

One lesson about the mechanism of intercellular force transmission ironically comes from studies of unicellular fission yeast. This lesson involves the importance of actin turnover (i.e., actin filament assembly and disassembly) in mediating the coupling between the actomyosin cortex and the adherens junction. Models of contractile ring formation in fission yeast have shown that actin disassembly and remodeling are required to generate a uniform contractile ring network. Actin turnover counterbalances the clustering/aggregation of the network that happens as the myosin motor contracts it (Fig. 1.3A) (Stachowiak et al., 2014; Vavylonis et al., 2008). Disrupting actin turnover causes actomyosin to aggregate unevenly, not only in the contractile ring, but also in contractile ventral furrow cells (Fig. 1.3C,D) (Chen and Pollard, 2011; Jodoin et al., 2015). Continuous actin turnover during contraction explains why the density of the actin network is constant as the network contracts in both the fission yeast contractile ring and cells of the *Drosophila* ventral furrow (Mason et al., 2013; Wu and Pollard, 2005). In addition, early work on sea urchin cytokinesis has demonstrated that the volume of the contractile ring

decreased with constriction, suggesting that ring components are disassembled during contraction (Schroeder, 1972). In the ventral furrow, F-actin disassembly and the renewal of the apical actin meshwork are important for the stable coupling of that apical network to the adherens junctions; in the absence of robust actin turnover actomyosin aggregates and separates from the junction (Fig. 1.3D) (Jodoin et al., 2015).

In the context of neural tube closure, this mechanism of actin turnover propagating forces across a tissue could possibly explain the role of Cofilin, an actin depolymerase, in neural tube defects. Single nucleotide polymorphisms (SNPs) in the CFL1 gene, which encodes the non-muscle Cofilin, are associated with human spina bifida, although it is not clear whether or how these SNPs impact Cofilin function (Zhu et al., 2007). In addition, Cofilin mutants result in neural tube defects in mice (Escuin et al., 2015; Gurniak et al., 2005). Disruption of actin turnover also affects the establishment of planar cell polarity and this role for actin turnover may also play a role in the neural tube defect (Mahaffey et al., 2013). Although it is still debated whether neural tube closure is driven by myosin 2 motor-dependent contractility (Escuin et al., 2015), it is possible that actin turnover contributes to morphogenesis by enabling stable connections of actomyosin networks to intercellular junctions. For future studies of neural tube closure, it will be important to use live imaging to determine whether actin networks aggregate and separate from junctions in Cofilin mutants.

1.1.4. Actomyosin contractile systems regulate tissue stiffness

In addition to generating contractility, actomyosin networks contribute to the material properties of cells and tissues, which impacts how tissues respond to contractile forces during development. The details of actin network mechanics have been reviewed elsewhere (Gardel et

al., 2008). Briefly, the elastic properties of actin networks depend on the actin and crosslinker concentration and on the amount of network stress, all of which are tightly regulated in the cell (Gardel et al., 2004; Xu et al., 2000). In actomyosin networks reconstituted from purified proteins, the effect of myosin activity on the properties of the actin network can vary. In the case of high ATP levels, myosin can fluidize the network; however, myosin can stiffen the network at low ATP levels, where the myosin motor heads will remain bound to F-actin for longer (Gardel et al., 2008).

Actomyosin contractility is also important for regulating tissue stiffness in developing organisms. This was observed in the context of axis elongation in the *Xenopus* embryo, where tissue stiffness was decreased when ROCK was inhibited (Zhou et al., 2009). The stiffness may be important for development as it increases over the course of axis elongation. One role for the increase in stiffness may be to allow the elongating tissue to push against neighboring tissues. In tissue explants of the *Xenopus* neural plate, actomyosin contractility was required for elongation when the tissue was cultured in agarose, which provides resistance to elongation, but not when the explant was cultured in liquid medium (Zhou et al., 2015). Additionally, during elongation of the *C. elegans* embryo, the actomyosin cortex plays a role in maintaining the anisotropic stiffness that is thought to drive tissue elongation (Vuong-Brender et al., 2017). In this sense, regulation of myosin activity and the organization of the actin network can affect morphogenesis without necessarily generating tissue contraction. The implication of this dual role for actomyosin networks in generating contractility and also regulating the mechanical properties of the same or neighboring tissues is that inhibiting myosin and F-actin may simultaneously block contractility and change the mechanical properties of the surrounding tissue making it difficult to interpret resulting mutant phenotypes.

Relaxation of cortical tension through the negative regulation of myosin also plays an important role in certain morphogenetic processes, including the expansion of the ventricle lumen in the zebrafish hindbrain and processes of tissue elongation that include zebrafish epiboly and *Drosophila* dorsal closure. The expansion or inflation of the zebrafish hindbrain requires the epithelium surrounding the ventricle lumen to relax through the activity of myosin phosphatase, an inhibitor of myosin activation (Gutzman and Sive, 2010). Mutation of myosin phosphatase causes a smaller ventricle than wildtype, presumably because the surrounding epithelium has high cortical tension or stiffness and cannot deform. In a recent paper, it was shown that an Arf guanine nucleotide exchange factor, known as cytohesin, is required to downregulate actomyosin contractility to enable tissue elongation in both zebrafish and *Drosophila* (West et al., 2017). Thus, the regulation of stiffness through modulation of actomyosin contractility appears to be a strategy by which organisms restrict or permit tissue deformations.

1.2. Tissue level organization of contractility and form

The next step in understanding how biological form is created is to understand how different tissue-level organizations of actomyosin contractility generate different biological forms. The following section discusses a few simple developmental systems in which the relationship between tissue level organization of actomyosin contractility and the resulting biological form are beginning to be understood. In many of the cases I have chosen, our understanding of the process has been enhanced with the help of minimal mechanical models. Many of these models approximate actomyosin contractility with general increases in surface tension. While surface tension and energy minimization in the manner of soap bubbles is not consistent with our current understanding of the energy-consuming mechanisms governing cell shape, energy

models, such as vertex models, are often useful for modeling morphogenetic systems (Farhadifar et al., 2007; Fletcher et al., 2014). Furthermore, the investigation of how contractility drives morphogenesis is often accompanied by measurements of cortical tension. However, it should be noted that, in addition to actomyosin-based contractility, tissue surface tension is influenced by cell-cell adhesion and cell osmotic pressure (Krens et al., 2017; Maitre et al., 2012; Steinberg, 1963).

The first examples presented are simple examples in which individual cells have elevated levels of cortical tension with respect to their neighbors. In general, these systems all use a conserved force-generating module, the actomyosin cytoskeleton. In many cases, the exact nature and organization of the actomyosin cytoskeleton has yet to be established. However, the arrangement of contracting cells influences where forces are balanced, which ultimately affects the resulting form.

1.2.1. Differential tension driving epithelial cell ingression

Cell ingression is the process by which single or multiple cells leave an epithelial layer. Cell ingression from an epithelium is important for regulating growth and homeostasis and is also important for tissue architecture. In numerous examples, from *C. elegans* to the mouse, it has been shown that cell ingression is associated with elevated contractility and cortical tension in the ingressing cell. The tension differential between ingressing and neighboring cells during the ingression processes is often dependent on actomyosin accumulation in the ingressing cell or at the boundary between the ingressing cell and non-ingressing cells (Fig. 1.4A,B).

In early development, cell ingression is important to physically separate cells with

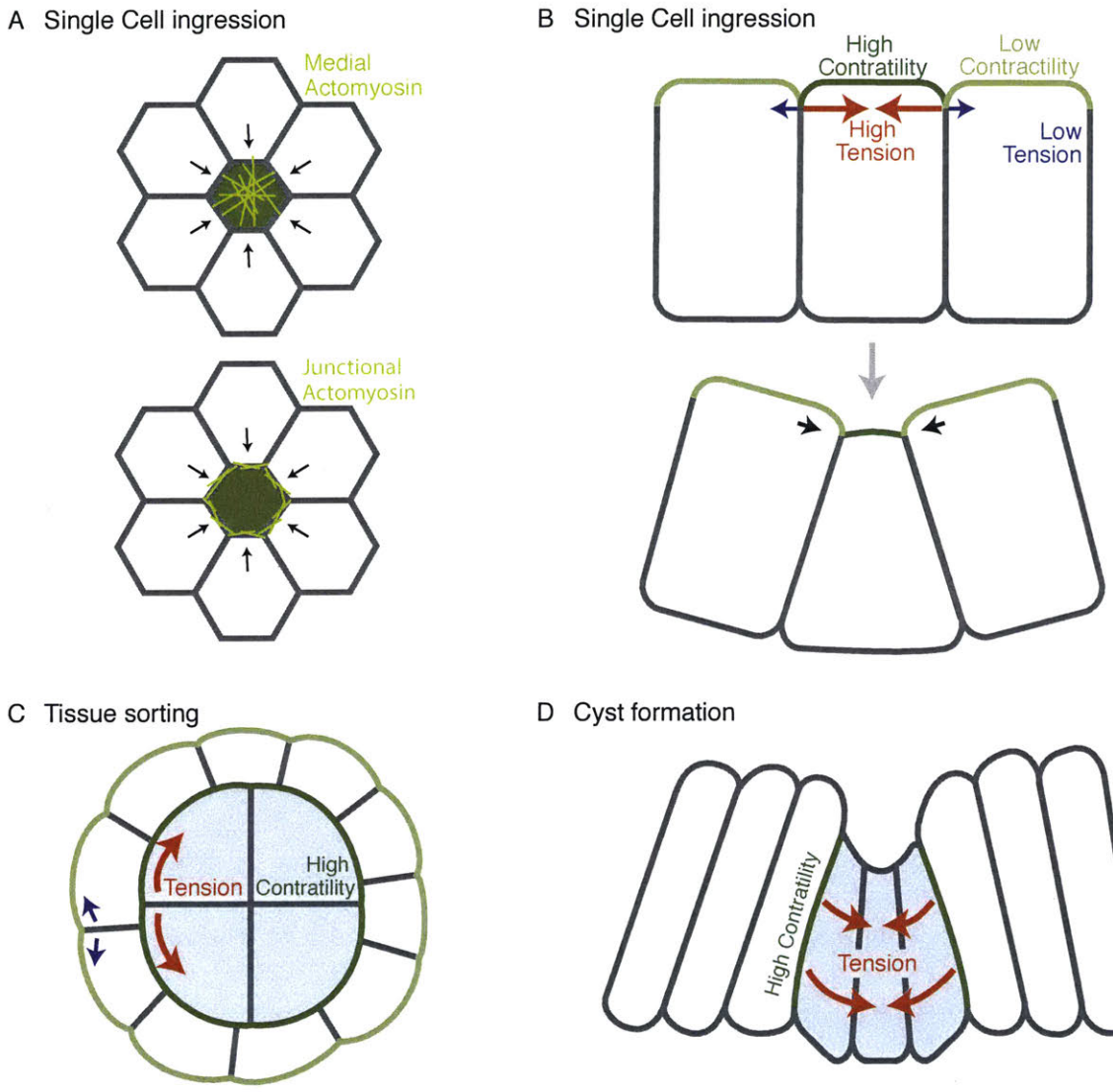

Figure 1.4: Differential contractility can cause ingression, cell sorting, and morphological changes. (A) *en face* view of an epithelial cell experiencing higher cortical tension levels than neighboring cells illustrating the difference between medial localization of the actomyosin network (top) and junctional localization (bottom). Actomyosin networks are illustrated in yellow. (B) Apical-basal cross-section of ingressing cell before (top) and during (bottom) ingression. Cortical tension is denoted in green. (C) Diagram of sorting between two cell types: white cells (lower tension) and gray cells (higher tension). Relative cortical tension is denoted in green, with darker green indicating higher tension. (D) Diagram of cyst formation due to high tension at clone boundaries and resulting inward pressure. (A-D) Red arrows denote the direction of high tension force and blue arrows denote direction of low tension force. Black arrows denote movement.

different fates. During *C. elegans* gastrulation, two of the cells fated to be endoderm ingress from the surface layer (Lee and Goldstein, 2003). In mouse, the cells that will form the fetus come from the inner cell mass, a collection of cells that are internalized early in development (Johnson

and Ziomek, 1981). Cell ingression has recently been shown drive internalization for those cells that are not internalized by asymmetric cell division (Maitre et al., 2016; Samarage et al., 2015). In both the *C. elegans* and mouse examples, cells gradually reduce their surface area (in both cases an apical surface) until they are completely enveloped by the remaining cells of the embryo. Laser ablations have shown that internalizing cells have higher cortical tension at the apical surface than do the neighboring cells, and that the higher levels of tension depend on actomyosin contractility (Roh-Johnson et al., 2012; Samarage et al., 2015). The imbalance in cortical tension between neighboring cells is likely critical for driving ingression. For instance, prior to inner cell mass ingression in the mouse embryo there is a universal increase in cortical tension. This universal increase in cortical tension at the embryo surface does not result in ingression, but rather compaction of the embryo, such that cells become pressed tightly together (Maitre et al., 2015). Compaction also depends on the extension of filopodia from some of the cells onto neighboring cells (Fierro-Gonzalez et al., 2013). These filopodia may also be required to generate cortical tension (Fierro-Gonzalez et al., 2013).

It is interesting to note that actomyosin exhibits different organizations in these different systems. In *C. elegans*, an apical actomyosin cortex contracts centripetally to generate tension and reduce apical surface area (Roh-Johnson et al., 2012). In contrast, ingressing inner cell mass cells have a prominent actomyosin belt at intercellular junctions that appears to drive ingression (Samarage et al., 2015). During compaction, the surface actomyosin cortex undergoes pulsatile or wave-like contractions (Maitre et al., 2015). When *Drosophila* neuroblasts delaminate from the surface ectoderm, another example of cell ingression, both junctional actomyosin accumulation and pulses of apical myosin accompany ingression (An et al., 2017; Simoes et al., 2017). Disruption of the myosin pulsing disrupted invagination although myosin depletion experiments

have not indicated a critical role for myosin and it is possible other processes are also critical for neuroblast ingression (An et al., 2017; Simoes et al., 2017). Despite the different spatio-temporal organizations of myosin in these divergent systems, overall it appears that elevated cortical tension in and around a single cell can drive cell ingression.

In general, the model that cell ingression is driven by differential regulation of cortical tension through actomyosin contractility and thus, force imbalance, seems to hold for a variety of systems. Apoptotic cells are extruded from epithelia in a system that parallels cell ingression. This process also depends on increased cortical tension and actomyosin contractility, but in both the apoptotic cell and neighboring cells (Kuipers et al., 2014; Rosenblatt et al., 2001; Slattum et al., 2009; Toyama et al., 2008). It seems clear that high cortical tension is driven by actomyosin activity, but it is also clear that there a diversity of ways in which actomyosin can produce force (i.e., medial vs. junctional and autonomous vs. non-autonomous). In addition, other mechanisms, such as changes in basolateral contractility could also drive ingression (Jodoin and Martin, 2016; Wu et al., 2014). An interesting future avenue of research is to address why apical constriction sometimes results in ingression and other times does not.

1.2.2. Tension between different populations of cells

Cell types can exhibit intrinsic differences in levels of cortical tension, and it has been shown that cortical tension can be regulated at the boundaries of different cell types (Bielmeier et al., 2016). As we discussed previously, cortical tension is also often differentially regulated at cell-medium (often apical) vs cell-cell (often baso-lateral) interfaces. These imbalances can lead to cell sorting behavior (Fig. 1.4C), as well as changes to tissue shape (Fig. 1.4D) (Harris, 1976; Krieg et al., 2008).

Cultured aggregates of zebrafish endoderm, mesoderm, and ectoderm cells sort into clusters of distinct cell types due to difference in cortical tension between cell types (Krieg et al., 2008). The cells with the higher cortical tension will cluster and the cell type with lower tension will envelop them (Fig. 1.4C, gray vs white cells). This event depends on myosin activity as well as low osmotic pressure to create the difference in cortical tension between groups of cells (Krens et al., 2017; Krieg et al., 2008). This cell sorting can be explained using a Cellular Potts Model, which predicts that correct cell sorting depends not only on a difference in cortical tension between the two cell populations, but also a difference in cortical tension between the cortex at the cell-medium interface and the cortex at the cell-cell interface (Krieg et al., 2008; Maitre et al., 2012). There are three levels of cortical tension in this system and both the subcellular restriction of high tension to the tissue surface and the tension differential between the two cell types are required for generating a multilayered structure with high-tension cells at the interior.

Another example of cell sorting is the formation of cysts in epithelial tissues (Fig. 1.4D). It has been demonstrated that cancer cells are able to form cysts that separate them from non-cancerous cells (Cortina et al., 2007). In addition, cysts containing cells of one cell fate have been shown to separate from background cells of a different fate. An example of this has been observed in the *Drosophila* wing imaginal disc; cysts of wild-type cells develop in the wing epithelium where the majority of cells are misexpressing a cell-fate-specifying transcription factor (Bielmeier et al., 2016). The formation of these cysts is yet another example of a mechanism whereby contraction drives tissue shape change. Clones of cells that differentially express a gene regulating cell fate accumulate myosin and F-actin along basolateral cell surfaces contacting the neighboring wild-type tissue, suggesting activation of the actomyosin contractile cortex (Bielmeier et al., 2016). No tension measurements were made in this system, but an in silico

vertex model that assumed increased cortical tension at the contact boundaries between different cell types was able to recapitulate bending of the clone into a cyst-like bulge.

Both of the previous examples involve increased cortical tension at the boundaries of the two cell types, but different shapes emerge. The commonality is that differential cortical tension at an interface results in physical separation of cell types. In each of the systems discussed, the cells are able to respond to increases in tension without clear directional constraints. We next discuss the role of tissue stiffness and resistance in modifying the effects of contractility on tissue shape.

1.2.3. Balance versus imbalance at intercellular junctions

Whether contractile forces are organized such that they are balanced or not at junctions is also important for tissue shape and organization. During tissue extension, actomyosin cables can be enriched along specific intercellular junctions due to planar cell polarity (Bertet et al., 2004; Shindo and Wallingford, 2014; Zallen and Wieschaus, 2004). Actomyosin enrichment at junctions in these cases is associated with tension and junctional shrinkage, suggesting that there is unbalanced contractile force (Fig. 1.5A) (Fernandez-Gonzalez et al., 2009; Rauzi et al., 2008). This anisotropic tension operates in tandem with polarized basal cell migration to promote axis extension (Sun et al., 2017). Medial, not junctional, actomyosin contractility appears to elongate new cell contacts after the old contact has disappeared (Fig. 1.5A) (Collinet et al., 2015; Yu and Fernandez-Gonzalez, 2016). The consequence of polarized actomyosin contractility and cell crawling is that cells converge along the dorsal-ventral axis, resulting in an anterior-posterior extension.

Alternatively, balanced forces along junctional interfaces have been shown to resist cell

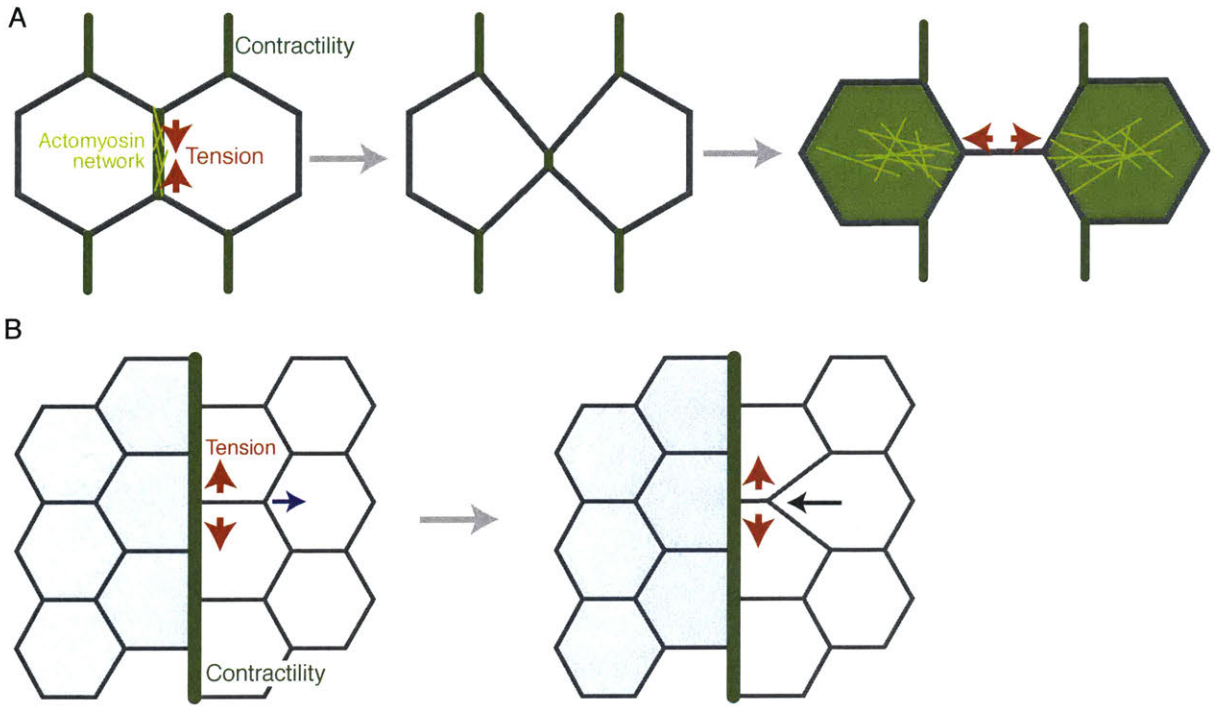

Figure 1.5: Diagram of polarized junctional actomyosin contractility during tissue extension and at compartment boundaries. (A) Diagram of neighbor exchange during tissue extension. Actomyosin is planar polarized to the vertical junction. This actomyosin network leads to apical junction shrinkage either through contraction or by directionally stabilizing fluctuations in junction length (Rauzi et al., 2010). The junction is then expanded in the horizontal direction by medial actomyosin contractility in green cells. (B) Diagram of forces at a compartment boundary that inhibit cell rearrangement. When a rearrangement happens near the boundary the boundary resists deformation. For example, the shrinking horizontal junction shrinks from one end so that the boundary remains straight. Regions of contractility are depicted in green, with network organization diagramed in yellow. Red arrows denote the direction of contractile tension.

movement and mixing. In both development and homeostasis, different cell types are segregated from each other in what are known as compartments (Batlle and Wilkinson, 2012). Recent studies have shown that actomyosin contractility is often activated at cell interfaces of the compartment boundary (Landsberg et al., 2009; Major and Irvine, 2006; Monier et al., 2010), in a similar manner to the process described for cyst formation in the wing (Bielmeier et al., 2016) In this case, balanced myosin contractility and the resulting high tension maintains a straight compartment boundary and prevents cell mixing between compartments (Fig. 1.5B). Activation of myosin has also been shown to inhibit cell mixing and maintain boundaries between different

cell types in *Xenopus* (Fagotto et al., 2013). In *Drosophila* epithelia, high tension at boundaries resists the local deformations from cell division as well as to bias cell intercalation so as to prevent cell movement across the boundary (Fig. 1.5B), and the mixing of cells of different fates (Monier et al., 2010; Umetsu et al., 2014). Thus, similar to examples of apical actomyosin cortex contraction, unbalanced junctional tension drives tissue shape change whereas balanced forces resist movement.

In conclusion, these examples illustrate the variety of ways in which different patterns of contractility and resulting tensions can sculpt the myriad of animal tissue shapes observed in nature. These examples illustrate the importance of considering tissue context and force balance when thinking about how biological form is created. I have focused on systems where there is knowledge of 'active' molecular mechanisms that underlie the resulting forces and/or material properties, there are many other systems whose analysis is likely to unearth new principles by which cells and tissues regulate their growth and form.

1.3. Establishment of the ventral domain in the *Drosophila* embryo

The development of *Drosophila melanogaster* embryos is incredibly efficient, resulting in a fully formed larvae in just 24 hours. Much of the speed with which the embryo develops can be attributed to the enormous amount of resources and information deposited in the embryo maternally. After it is laid, the embryo undergoes 13 rounds of synchronous syncytial divisions (i.e., the nuclei divide without any cytokinetic events). After the ninth division, the nuclei move to the periphery of the embryo where they remain until cellularization, the process in which the nuclei are partitioned into individual cells by an ingression of the plasma membrane surrounding the embryo. Cellularization directly precedes ventral furrow formation and results in the

formation of a single epithelial sheet that surrounds the entire embryo. At this stage, the epithelium has the classic apical-basal polarity, with the apical surface of the cells creating the outer surface of the embryo. This epithelium is unique in that it lacks a basement membrane.

The ventral domain of *Drosophila* is defined as part of the dorsal-ventral patterning process in the embryo. The dorsal-ventral axis is defined by the activation of the maternal morphogen Dorsal in a gradient (Steward et al., 1988). Dorsal is deposited maternally as both mRNA and protein and translated everywhere in the embryo, but it is activated in a gradient along the dorsal-ventral axis by a Toll-based signaling pathway. This signaling pathway promotes nuclear translocation of Dorsal, a transcription factor. Nuclear levels of Dorsal are proportional to the amount of Toll signaling; the evidence for this is nicely summarized in (Reeves and Stathopoulos, 2009). This signaling gradient is set up during oogenesis by signaling between the embryo and the maternal follicle cells that surround the embryo. A protease cascade is activated between the vitelline membrane and the embryo surface in a gradient along the dorsal-ventral axis of the embryo as well (Cho et al., 2012; Hong and Hashimoto, 1995; Konrad et al., 1998; Steen et al., 2010). This protease cascades leads to the processing and activation of the Toll ligand Spätzle (Spz) (DeLotto and DeLotto, 1998). The protease cascade is also spatially restricted to a gradient by the protease inhibitor Serpin27A (Hashimoto et al., 2003; Ligoxygakis et al., 2003).

High levels of nuclear Dorsal activate the transcription of two embryonic transcription factors in the ventral domain, Twist and Snail, that are required for mesodermal cell fate (Thisse et al., 1987). While Twist is thought to generally function as an activator, and Snail as a repressor, there is evidence that they both can act in either capacity (Kolsch et al., 2007; Manning et al., 2013; Rembold et al., 2014). Twist and Snail are both required for normal

ventral furrow formation, and, interestingly, their mammalian homologues have been implicated in cancer metastasis (Yang et al., 2004).

Twist plays a role in both patterning the ventral domain and inducing apical constriction in the embryo. *twist* is required for mesodermal cell fate, and is required to activate the transcription of *snail*. Prior to this work, the distribution of *twist* mRNA had not been quantified with respect to the ventral furrow. Twist is thought to induce ventral furrow formation through two transcriptional targets, *T48* and *folded gastrulation* (*fog*) (Costa et al., 1994; Kolsch et al., 2007). Fog is thought to act as a ligand for a G-protein coupled receptor (GPCR), which activates a heterotrimeric G protein (Kanesaki et al., 2013; Manning et al., 2013). The Gα, *concertina*, is required for normal ventral furrow formation and thought to be activated by Fog binding to a GPCR receptor (Dawes-Hoang et al., 2005). DRhoGEF2 is also required for ventral furrow formation, and is thought to be activated by both the Gα and the Twist target, T48 (Barrett et al., 1997; Hacker and Perrimon, 1998; Kolsch et al., 2007). DRhoGEF2 is then able to activate actomyosin contractility through the RhoA/ROCK pathway discussed earlier in this chapter.

There are two known mechanisms by which Snail is thought to promote ventral furrow formation. The first is possibly through the activation of the transcription of the GPCR *mist*, a receptor for the Fog ligand (Manning et al., 2013). Mist is thought to act in parallel with Smog, a maternally-deposited GPCR (Kerridge et al., 2016). Snail is required for the apical movement of the adherens junctions in the ventral furrow that precedes furrow formation (Dawes-Hoang et al., 2005; Leptin and Grunewald, 1990). This movement depends on the repression of the *bearded* genes by Snail in the ventral domain (Chanet and Schweisguth, 2012). It was recently discovered that the *bearded* genes repress an independent factor promoting actomyosin

contractility in the mesoderm, Neuralized, an E3 ubiquitin ligase (Perez-Mockus et al., 2017). It is not yet understood how Neuralized promotes myosin contractility in the mesoderm. Snail thus activates ventral furrow formation by repressing a repressor of a contractility-promoting factor in the ventral domain.

1.3.1. Resistance: the interplay of tension and stiffness

In the *Drosophila* ventral furrow, actomyosin networks function both to generate and resist contractility. This is determined by the patterning of the myosin activation in the ventral domain of the embryo. Because the embryo is an ellipsoid (Fig. 1.1A), there are more cells activating actomyosin contractility along the anterior-posterior axis then along the dorsal-ventral axis. This results in higher tension along the anterior posterior axis (Chanet et al., 2017; Martin et al., 2010), which causes the cells to constrict less along the anterior-posterior axis. When cells in the ventral domain are mechanically isolated, they constrict uniformly in all directions. Thus, actomyosin contractility causes cells to constrict along the dorsal-ventral axis, but due to the patterning of contractility across the tissue, actomyosin also serves to restrict constriction along the anterior-posterior axis.

Cells along the dorsal-ventral axis do not behave in a uniform manner. Cells closest to the ventral midline constrict earlier and possibly more rapidly than cells further away (Oda and Tsukita, 2001; Sweeton et al., 1991). The region of constricting cells is less than region of cells expressing *twist* (Leptin, 1991; Sweeton et al., 1991). The Twist target *fog* was known to be expressed in a more restricted domain that corresponded more closely with the domain of apical constriction (Costa et al., 1994). The main questions answered in the following chapters are: 1) What causes cells closest to the ventral midline to constrict more? And 2) Is this difference in

cell behavior important for tissue folding?

1.4. References

Aigouy, B., Farhadifar, R., Staple, D.B., Sagner, A., Roper, J.C., Julicher, F., Eaton, S., 2010. Cell flow reorients the axis of planar polarity in the wing epithelium of *Drosophila*. *Cell* 142, 773-786.

Amano, M., Ito, M., Kimura, K., Fukata, Y., Chihara, K., Nakano, T., Matsuura, Y., Kaibuchi, K., 1996. Phosphorylation and activation of myosin by Rho-associated kinase (Rho-kinase). *J Biol Chem* 271, 20246-20249.

An, Y., Xue, G., Shaobo, Y., Mingxi, D., Zhou, X., Yu, W., Ishibashi, T., Zhang, L., Yan, Y., 2017. Apical constriction is driven by a pulsatile apical myosin network in delaminating *Drosophila* neuroblasts. *Development*.

Andrianantoandro, E., Pollard, T.D., 2006. Mechanism of actin filament turnover by severing and nucleation at different concentrations of ADF/cofilin. *Mol Cell* 24, 13-23.

Barany, M., 1967. ATPase activity of myosin correlated with speed of muscle shortening. *J Gen Physiol* 50, Suppl:197-218.

Barrett, K., Leptin, M., Settleman, J., 1997. The Rho GTPase and a putative RhoGEF mediate a signaling pathway for the cell shape changes in *Drosophila* gastrulation. *Cell* 91, 905-915.

Batlle, E., Wilkinson, D.G., 2012. Molecular mechanisms of cell segregation and boundary formation in development and tumorigenesis. *Cold Spring Harb Perspect Biol* 4, a008227.

Bertet, C., Sulak, L., Lecuit, T., 2004. Myosin-dependent junction remodelling controls planar cell intercalation and axis elongation. *Nature* 429, 667-671.

Bielmeier, C., Alt, S., Weichselberger, V., La Fortezza, M., Harz, H., Julicher, F., Salbreux, G., Classen, A.K., 2016. Interface Contractility between Differently Fated Cells Drives Cell Elimination and Cyst Formation. *Curr Biol* 26, 563-574.

Buckley, C.D., Tan, J., Anderson, K.L., Hanein, D., Volkmann, N., Weis, W.I., Nelson, W.J., Dunn, A.R., 2014. Cell adhesion. The minimal cadherin-catenin complex binds to actin filaments under force. *Science* 346, 1254211.

Calvo, F., Ege, N., Grande-Garcia, A., Hooper, S., Jenkins, R.P., Chaudhry, S.I., Harrington, K., Williamson, P., Moeendarbary, E., Charras, G., Sahai, E., 2013. Mechanotransduction and YAP-dependent matrix remodelling is required for the generation and maintenance of cancer-associated fibroblasts. *Nat Cell Biol* 15, 637-646.

Chanet, S., Miller, C.J., Vaishnav, E.D., Ermentrout, B., Davidson, L.A., Martin, A.C., 2017. Actomyosin meshwork mechanosensing enables tissue shape to orient cell force. *Nat Commun* 8, 15014.

Chanet, S., Schweisguth, F., 2012. Regulation of epithelial polarity by the E3 ubiquitin ligase Neuralized and the Bearded inhibitors in *Drosophila*. *Nat Cell Biol* 14, 467-476.

Chen, Q., Pollard, T.D., 2011. Actin filament severing by cofilin is more important for assembly than constriction of the cytokinetic contractile ring. *J Cell Biol* 195, 485-498.

Cho, Y.S., Stevens, L.M., Sieverman, K.J., Nguyen, J., Stein, D., 2012. A ventrally localized protease in the *Drosophila* egg controls embryo dorsoventral polarity. *Curr Biol* 22, 1013-1018.

Choi, W., Acharya, B.R., Peyret, G., Fardin, M.A., Mege, R.M., Ladoux, B., Yap, A.S., Fanning, A.S., Peifer, M., 2016. Remodeling the zonula adherens in response to tension and the role of afadin in this response. *J Cell Biol* 213, 243-260.

Chung, S., Kim, S., Andrew, D.J., 2017. Uncoupling apical constriction from tissue invagination. *Elife* 6.

Clarke, D.N., Miller, P.W., Lowe, C.J., Weis, W.I., Nelson, W.J., 2016. Characterization of the Cadherin-Catenin Complex of the Sea Anemone Nematostella vectensis and Implications for the Evolution of Metazoan Cell-Cell Adhesion. *Mol Biol Evol* 33, 2016-2029.

Collinet, C., Rauzi, M., Lenne, P.F., Lecuit, T., 2015. Local and tissue-scale forces drive oriented junction growth during tissue extension. *Nat Cell Biol* 17, 1247-1258.

Coravos, J.S., Martin, A.C., 2016. Apical Sarcomere-like Actomyosin Contracts Nonmuscle *Drosophila* Epithelial Cells. *Dev Cell* 39, 346-358.

Cortina, C., Palomo-Ponce, S., Iglesias, M., Fernandez-Masip, J.L., Vivancos, A., Whissell, G., Huma, M., Peiro, N., Gallego, L., Jonkheer, S., Davy, A., Lloreta, J., Sancho, E., Batlle, E., 2007. EphB-ephrin-B interactions suppress colorectal cancer progression by compartmentalizing tumor cells. *Nat Genet* 39, 1376-1383.

Costa, M., Wilson, E.T., Wieschaus, E., 1994. A putative cell signal encoded by the folded gastrulation gene coordinates cell shape changes during *Drosophila* gastrulation. *Cell* 76, 1075-1089.

Craig, R., Smith, R., Kendrick-Jones, J., 1983. Light-chain phosphorylation controls the conformation of vertebrate non-muscle and smooth muscle myosin molecules. *Nature* 302, 436-439.

Dawes-Hoang, R.E., Parmar, K.M., Christiansen, A.E., Phelps, C.B., Brand, A.H., Wieschaus, E.F., 2005. folded gastrulation, cell shape change and the control of myosin localization. *Development* 132, 4165-4178.

DeLotto, Y., DeLotto, R., 1998. Proteolytic processing of the *Drosophila* Spatzle protein by easter generates a dimeric NGF-like molecule with ventralising activity. *Mech Dev* 72, 141-148.

Escuin, S., Vernay, B., Savery, D., Gurniak, C.B., Witke, W., Greene, N.D., Copp, A.J., 2015. Rho-kinase-dependent actin turnover and actomyosin disassembly are necessary for mouse spinal neural tube closure. *J Cell Sci* 128, 2468-2481.

Etournay, R., Popovic, M., Merkel, M., Nandi, A., Blasse, C., Aigouy, B., Brandl, H., Myers, G., Salbreux, G., Julicher, F., Eaton, S., 2015. Interplay of cell dynamics and epithelial tension during morphogenesis of the *Drosophila* pupal wing. *Elife* 4, e07090.

Fagotto, F., Rohani, N., Touret, A.S., Li, R., 2013. A molecular base for cell sorting at embryonic boundaries: contact inhibition of cadherin adhesion by ephrin/ Eph-dependent contractility. *Dev Cell* 27, 72-87.

Farhadifar, R., Roper, J.C., Aigouy, B., Eaton, S., Julicher, F., 2007. The influence of cell mechanics, cell-cell interactions, and proliferation on epithelial packing. *Curr Biol* 17, 2095-2104.

Fenix, A.M., Taneja, N., Buttler, C.A., Lewis, J., Van Engelenburg, S.B., Ohi, R., Burnette, D.T., 2016. Expansion and concatenation of non-muscle myosin IIA filaments drive cellular contractile system formation during interphase and mitosis. *Mol Biol Cell.*

Fernandez-Gonzalez, R., Simoes Sde, M., Roper, J.C., Eaton, S., Zallen, J.A., 2009. Myosin II dynamics are regulated by tension in intercalating cells. *Dev Cell* 17, 736-743.

Fierro-Gonzalez, J.C., White, M.D., Silva, J.C., Plachta, N., 2013. Cadherin-dependent filopodia control preimplantation embryo compaction. *Nat Cell Biol* 15, 1424-1433.

Fletcher, A.G., Osterfield, M., Baker, R.E., Shvartsman, S.Y., 2014. Vertex models of epithelial morphogenesis. *Biophys J* 106, 2291-2304.

Galea, G.L., Cho, Y.J., Galea, G., Mole, M.A., Rolo, A., Savery, D., Moulding, D., Culshaw, L.H., Nikolopoulou, E., Greene, N.D.E., Copp, A.J., 2017. Biomechanical coupling facilitates spinal neural tube closure in mouse embryos. *Proc Natl Acad Sci U S A.*

Gardel, M.L., Kasza, K.E., Brangwynne, C.P., Liu, J., Weitz, D.A., 2008. Chapter 19: Mechanical response of cytoskeletal networks. *Methods Cell Biol* 89, 487-519.

Gardel, M.L., Shin, J.H., MacKintosh, F.C., Mahadevan, L., Matsudaira, P., Weitz, D.A., 2004. Elastic behavior of cross-linked and bundled actin networks. *Science* 304, 1301-1305.

Goody, M.F., Sher, R.B., Henry, C.A., 2015. Hanging on for the ride: adhesion to the extracellular matrix mediates cellular responses in skeletal muscle morphogenesis and disease. *Dev Biol* 401, 75-91.

Gurniak, C.B., Perlas, E., Witke, W., 2005. The actin depolymerizing factor n-cofilin is essential for neural tube morphogenesis and neural crest cell migration. *Dev Biol* 278, 231-241.

Gutzman, J.H., Sive, H., 2010. Epithelial relaxation mediated by the myosin phosphatase regulator Mypt1 is required for brain ventricle lumen expansion and hindbrain morphogenesis.

Development 137, 795-804.
Hacker, U., Perrimon, N., 1998. DRhoGEF2 encodes a member of the Dbl family of oncogenes and controls cell shape changes during gastrulation in *Drosophila*. *Genes Dev* 12, 274-284.
Harris, A.K., 1976. Is Cell sorting caused by differences in the work of intercellular adhesion? A critique of the Steinberg hypothesis. *J Theor Biol* 61, 267-285.
Hashimoto, C., Kim, D.R., Weiss, L.A., Miller, J.W., Morisato, D., 2003. Spatial regulation of developmental signaling by a serpin. *Dev Cell* 5, 945-950.
Heissler, S.M., Sellers, J.R., 2014. Myosin light chains: Teaching old dogs new tricks. *Bioarchitecture* 4, 169-188.
Heissler, S.M., Sellers, J.R., 2016. Various Themes of Myosin Regulation. *J Mol Biol* 428, 1927-1946.
Hong, C.C., Hashimoto, C., 1995. An unusual mosaic protein with a protease domain, encoded by the nudel gene, is involved in defining embryonic dorsoventral polarity in *Drosophila*. *Cell* 82, 785-794.
Huang, D.L., Bax, N.A., Buckley, C.D., Weis, W.I., Dunn, A.R., 2017. Vinculin forms a directionally asymmetric catch bond with F-actin. *Science* 357, 703-706.
Huveneers, S., Oldenburg, J., Spanjaard, E., van der Krogt, G., Grigoriev, I., Akhmanova, A., Rehmann, H., de Rooij, J., 2012. Vinculin associates with endothelial VE-cadherin junctions to control force-dependent remodeling. *J Cell Biol* 196, 641-652.
Huxley, H., Hanson, J., 1954. Changes in the cross-striations of muscle during contraction and stretch and their structural interpretation. *Nature* 173, 973-976.
Jodoin, J.N., Coravos, J.S., Chanet, S., Vasquez, C.G., Tworoger, M., Kingston, E.R., Perkins, L.A., Perrimon, N., Martin, A.C., 2015. Stable Force Balance between Epithelial Cells Arises from F-Actin Turnover. *Dev Cell* 35, 685-697.
Jodoin, J.N., Martin, A.C., 2016. Abl suppresses cell extrusion and intercalation during epithelium folding. *Mol Biol Cell* 27, 2822-2832.
Johnson, M.H., Ziomek, C.A., 1981. The foundation of two distinct cell lineages within the mouse morula. *Cell* 24, 71-80.
Kanesaki, T., Hirose, S., Grosshans, J., Fuse, N., 2013. Heterotrimeric G protein signaling governs the cortical stability during apical constriction in *Drosophila* gastrulation. *Mech Dev* 130, 132-142.
Kerridge, S., Munjal, A., Philippe, J.M., Jha, A., de las Bayonas, A.G., Saurin, A.J., Lecuit, T., 2016. Modular activation of Rho1 by GPCR signalling imparts polarized myosin II activation during morphogenesis. *Nat Cell Biol* 18, 261-270.
Koenderink, G.H., Dogic, Z., Nakamura, F., Bendix, P.M., MacKintosh, F.C., Hartwig, J.H., Stossel, T.P., Weitz, D.A., 2009. An active biopolymer network controlled by molecular motors. *Proc Natl Acad Sci U S A* 106, 15192-15197.
Kolsch, V., Seher, T., Fernandez-Ballester, G.J., Serrano, L., Leptin, M., 2007. Control of *Drosophila* gastrulation by apical localization of adherens junctions and RhoGEF2. *Science* 315, 384-386.
Konrad, K.D., Goralski, T.J., Mahowald, A.P., Marsh, J.L., 1998. The gastrulation defective gene of *Drosophila* melanogaster is a member of the serine protease superfamily. *Proc Natl Acad Sci U S A* 95, 6819-6824.
Kovacs, M., Toth, J., Hetenyi, C., Malnasi-Csizmadia, A., Sellers, J.R., 2004. Mechanism of blebbistatin inhibition of myosin II. *J Biol Chem* 279, 35557-35563.
Krens, S.F.G., Veldhuis, J.H., Barone, V., Capek, D., Maitre, J.L., Brodland, G.W., Heisenberg, C.P., 2017. Interstitial fluid osmolarity modulates the action of differential tissue surface tension in progenitor cell segregation during gastrulation. *Development* 144, 1798-1806.
Krieg, M., Arboleda-Estudillo, Y., Puech, P.H., Kafer, J., Graner, F., Muller, D.J., Heisenberg, C.P., 2008. Tensile forces govern germ-layer organization in zebrafish. *Nat Cell Biol* 10, 429-436.
Kuipers, D., Mehonic, A., Kajita, M., Peter, L., Fujita, Y., Duke, T., Charras, G., Gale, J.E., 2014. Epithelial repair is a two-stage process driven first by dying cells and then by their neighbours. *J*

Cell Sci 127, 1229-1241.
Ladoux, B., Nelson, W.J., Yan, J., Mege, R.M., 2015. The mechanotransduction machinery at work at adherens junctions. *Integr Biol (Camb)* 7, 1109-1119.
Landsberg, K.P., Farhadifar, R., Ranft, J., Umetsu, D., Widmann, T.J., Bittig, T., Said, A., Julicher, F., Dahmann, C., 2009. Increased cell bond tension governs cell sorting at the *Drosophila* anteroposterior compartment boundary. *Curr Biol* 19, 1950-1955.
Laplante, C., Huang, F., Tebbs, I.R., Bewersdorf, J., Pollard, T.D., 2016. Molecular organization of cytokinesis nodes and contractile rings by super-resolution fluorescence microscopy of live fission yeast. *Proc Natl Acad Sci U S A* 113, E5876-E5885.
Lecuit, T., Yap, A.S., 2015. E-cadherin junctions as active mechanical integrators in tissue dynamics. *Nat Cell Biol* 17, 533-539.
Lee, J.Y., Goldstein, B., 2003. Mechanisms of cell positioning during C. elegans gastrulation. *Development* 130, 307-320.
Leptin, M., 1991. twist and snail as positive and negative regulators during *Drosophila* mesoderm development. *Genes Dev* 5, 1568-1576.
Leptin, M., Grunewald, B., 1990. Cell shape changes during gastrulation in *Drosophila*. *Development* 110, 73-84.
Ligoxygakis, P., Roth, S., Reichhart, J.M., 2003. A serpin regulates dorsal-ventral axis formation in the *Drosophila* embryo. *Curr Biol* 13, 2097-2102.
Ma, X., Kovacs, M., Conti, M.A., Wang, A., Zhang, Y., Sellers, J.R., Adelstein, R.S., 2012. Nonmuscle myosin II exerts tension but does not translocate actin in vertebrate cytokinesis. *Proc Natl Acad Sci U S A* 109, 4509-4514.
Mahaffey, J.P., Grego-Bessa, J., Liem, K.F., Jr., Anderson, K.V., 2013. Cofilin and Vangl2 cooperate in the initiation of planar cell polarity in the mouse embryo. *Development* 140, 1262-1271.
Maitre, J.L., Berthoumieux, H., Krens, S.F., Salbreux, G., Julicher, F., Paluch, E., Heisenberg, C.P., 2012. Adhesion functions in cell sorting by mechanically coupling the cortices of adhering cells. *Science* 338, 253-256.
Maitre, J.L., Niwayama, R., Turlier, H., Nedelec, F., Hiiragi, T., 2015. Pulsatile cell-autonomous contractility drives compaction in the mouse embryo. *Nat Cell Biol* 17, 849-855.
Maitre, J.L., Turlier, H., Illukkumbura, R., Eismann, B., Niwayama, R., Nedelec, F., Hiiragi, T., 2016. Asymmetric division of contractile domains couples cell positioning and fate specification. *Nature* 536, 344-348.
Major, R.J., Irvine, K.D., 2006. Localization and requirement for Myosin II at the dorsal-ventral compartment boundary of the *Drosophila* wing. *Dev Dyn* 235, 3051-3058.
Manning, A.J., Peters, K.A., Peifer, M., Rogers, S.L., 2013. Regulation of epithelial morphogenesis by the G protein-coupled receptor mist and its ligand fog. *Sci Signal* 6, ra98.
Martin, A.C., Gelbart, M., Fernandez-Gonzalez, R., Kaschube, M., Wieschaus, E.F., 2010. Integration of contractile forces during tissue invagination. *J Cell Biol* 188, 735-749.
Mason, F.M., Tworoger, M., Martin, A.C., 2013. Apical domain polarization localizes actin-myosin activity to drive ratchet-like apical constriction. *Nat Cell Biol* 15, 926-936.
Mason, F.M., Xie, S., Vasquez, C.G., Tworoger, M., Martin, A.C., 2016. RhoA GTPase inhibition organizes contraction during epithelial morphogenesis. *J Cell Biol* 214, 603-617.
Mendes Pinto, I., Rubinstein, B., Kucharavy, A., Unruh, J.R., Li, R., 2012. Actin depolymerization drives actomyosin ring contraction during budding yeast cytokinesis. *Dev Cell* 22, 1247-1260.
Michael, M., Yap, A.S., 2013. The regulation and functional impact of actin assembly at cadherin cell-cell adhesions. *Semin Cell Dev Biol* 24, 298-307.
Monier, B., Pelissier-Monier, A., Brand, A.H., Sanson, B., 2010. An actomyosin-based barrier inhibits cell mixing at compartmental boundaries in *Drosophila* embryos. *Nat Cell Biol* 12, 60-65; sup pp 61-69.

Murrell, M.P., Gardel, M.L., 2012. F-actin buckling coordinates contractility and severing in a biomimetic actomyosin cortex. *Proc Natl Acad Sci U S A* 109, 20820-20825.

Oda, H., Tsukita, S., 2001. Real-time imaging of cell-cell adherens junctions reveals that *Drosophila* mesoderm invagination begins with two phases of apical constriction of cells. *J Cell Sci* 114, 493-501.

Perez-Mockus, G., Mazouni, K., Roca, V., Corradi, G., Conte, V., Schweisguth, F., 2017. Spatial regulation of contractility by Neuralized and Bearded during furrow invagination in *Drosophila*. *Nat Commun* 8, 1594.

Pfister, K., Shook, D.R., Chang, C., Keller, R., Skoglund, P., 2016. Molecular model for force production and transmission during vertebrate gastrulation. *Development* 143, 715-727.

Pollard, T.D., 2007. Regulation of actin filament assembly by Arp2/3 complex and formins. *Annu Rev Biophys Biomol Struct* 36, 451-477.

Qin, X., Park, B.O., Liu, J., Chen, B., Choesmel-Cadamuro, V., Belguise, K., Heo, W.D., Wang, X., 2017. Cell-matrix adhesion and cell-cell adhesion differentially control basal myosin oscillation and *Drosophila* egg chamber elongation. *Nat Commun* 8, 14708.

Quintin, S., Gally, C., Labouesse, M., 2008. Epithelial morphogenesis in embryos: asymmetries, motors and brakes. *Trends Genet* 24, 221-230.

Ramamurthy, B., Yengo, C.M., Straight, A.F., Mitchison, T.J., Sweeney, H.L., 2004. Kinetic mechanism of blebbistatin inhibition of nonmuscle myosin IIb. *Biochemistry* 43, 14832-14839.

Rauzi, M., Lenne, P.F., Lecuit, T., 2010. Planar polarized actomyosin contractile flows control epithelial junction remodelling. *Nature* 468, 1110-1114.

Rauzi, M., Verant, P., Lecuit, T., Lenne, P.F., 2008. Nature and anisotropy of cortical forces orienting *Drosophila* tissue morphogenesis. *Nat Cell Biol* 10, 1401-1410.

Ray, R.P., Matamoro-Vidal, A., Ribeiro, P.S., Tapon, N., Houle, D., Salazar-Ciudad, I., Thompson, B.J., 2015. Patterned Anchorage to the Apical Extracellular Matrix Defines Tissue Shape in the Developing Appendages of *Drosophila*. *Dev Cell* 34, 310-322.

Reeves, G.T., Stathopoulos, A., 2009. Graded dorsal and differential gene regulation in the *Drosophila* embryo. *Cold Spring Harb Perspect Biol* 1, a000836.

Rembold, M., Ciglar, L., Yanez-Cuna, J.O., Zinzen, R.P., Girardot, C., Jain, A., Welte, M.A., Stark, A., Leptin, M., Furlong, E.E., 2014. A conserved role for Snail as a potentiator of active transcription. *Genes Dev* 28, 167-181.

Reymann, A.C., Boujemaa-Paterski, R., Martiel, J.L., Guerin, C., Cao, W., Chin, H.F., De La Cruz, E.M., Thery, M., Blanchoin, L., 2012. Actin network architecture can determine myosin motor activity. *Science* 336, 1310-1314.

Roh-Johnson, M., Shemer, G., Higgins, C.D., McClellan, J.H., Werts, A.D., Tulu, U.S., Gao, L., Betzig, E., Kiehart, D.P., Goldstein, B., 2012. Triggering a cell shape change by exploiting preexisting actomyosin contractions. *Science* 335, 1232-1235.

Rosenblatt, J., Raff, M.C., Cramer, L.P., 2001. An epithelial cell destined for apoptosis signals its neighbors to extrude it by an actin- and myosin-dependent mechanism. *Curr Biol* 11, 1847-1857.

Samarage, C.R., White, M.D., Alvarez, Y.D., Fierro-Gonzalez, J.C., Henon, Y., Jesudason, E.C., Bissiere, S., Fouras, A., Plachta, N., 2015. Cortical Tension Allocates the First Inner Cells of the Mammalian Embryo. *Dev Cell* 34, 435-447.

Schroeder, T.E., 1972. The contractile ring. II. Determining its brief existence, volumetric changes, and vital role in cleaving Arbacia eggs. *J Cell Biol* 53, 419-434.

Shindo, A., Wallingford, J.B., 2014. PCP and septins compartmentalize cortical actomyosin to direct collective cell movement. *Science* 343, 649-652.

Simoes, S., Oh, Y., Wang, M.F.Z., Fernandez-Gonzalez, R., Tepass, U., 2017. Myosin II promotes the anisotropic loss of the apical domain during *Drosophila* neuroblast ingression. *J Cell Biol* 216, 1387-1404.

Slattum, G., McGee, K.M., Rosenblatt, J., 2009. P115 RhoGEF and microtubules decide the direction apoptotic cells extrude from an epithelium. *J Cell Biol* 186, 693-702.

Soares e Silva, M., Depken, M., Stuhrmann, B., Korsten, M., MacKintosh, F.C., Koenderink, G.H., 2011. Active multistage coarsening of actin networks driven by myosin motors. *Proc Natl Acad Sci U S A* 108, 9408-9413.

Stachowiak, M.R., Laplante, C., Chin, H.F., Guirao, B., Karatekin, E., Pollard, T.D., O'Shaughnessy, B., 2014. Mechanism of cytokinetic contractile ring constriction in fission yeast. *Dev Cell* 29, 547-561.

Steen, P.W., Tian, S., Tully, S.E., Cravatt, B.F., LeMosy, E.K., 2010. Activation of Snake in a serine protease cascade that defines the dorsoventral axis is atypical and pipe-independent in *Drosophila* embryos. *FEBS Lett* 584, 3557-3560.

Steinberg, M.S., 1963. Reconstruction of tissues by dissociated cells. Some morphogenetic tissue movements and the sorting out of embryonic cells may have a common explanation. *Science* 141, 401-408.

Steward, R., Zusman, S.B., Huang, L.H., Schedl, P., 1988. The dorsal protein is distributed in a gradient in early *Drosophila* embryos. *Cell* 55, 487-495.

Sun, S.X., Walcott, S., Wolgemuth, C.W., 2010. Cytoskeletal cross-linking and bundling in motor-independent contraction. *Curr Biol* 20, R649-654.

Sun, Z., Amourda, C., Shagirov, M., Hara, Y., Saunders, T.E., Toyama, Y., 2017. Basolateral protrusion and apical contraction cooperatively drive *Drosophila* germ-band extension. *Nat Cell Biol* 19, 375-383.

Sweeton, D., Parks, S., Costa, M., Wieschaus, E., 1991. Gastrulation in *Drosophila*: the formation of the ventral furrow and posterior midgut invaginations. *Development* 112, 775-789.

Thisse, B., el Messal, M., Perrin-Schmitt, F., 1987. The twist gene: isolation of a *Drosophila* zygotic gene necessary for the establishment of dorsoventral pattern. *Nucleic Acids Res* 15, 3439-3453.

Thompson, D.A.W., 1917. *On growth and form.* University press, Cambridge Eng.

Toyama, Y., Peralta, X.G., Wells, A.R., Kiehart, D.P., Edwards, G.S., 2008. Apoptotic force and tissue dynamics during *Drosophila* embryogenesis. *Science* 321, 1683-1686.

Umetsu, D., Aigouy, B., Aliee, M., Sui, L., Eaton, S., Julicher, F., Dahmann, C., 2014. Local increases in mechanical tension shape compartment boundaries by biasing cell intercalations. *Curr Biol* 24, 1798-1805.

Vale, R.D., Milligan, R.A., 2000. The way things move: looking under the hood of molecular motor proteins. *Science* 288, 88-95.

Vasquez, C.G., Heissler, S.M., Billington, N., Sellers, J.R., Martin, A.C., 2016. *Drosophila* non-muscle myosin II motor activity determines the rate of tissue folding. *Elife* 5.

Vavylonis, D., Wu, J.Q., Hao, S., O'Shaughnessy, B., Pollard, T.D., 2008. Assembly mechanism of the contractile ring for cytokinesis by fission yeast. *Science* 319, 97-100.

Vicente-Manzanares, M., Zareno, J., Whitmore, L., Choi, C.K., Horwitz, A.F., 2007. Regulation of protrusion, adhesion dynamics, and polarity by myosins IIA and IIB in migrating cells. *J Cell Biol* 176, 573-580.

Vuong-Brender, T.T., Ben Amar, M., Pontabry, J., Labouesse, M., 2017. The interplay of stiffness and force anisotropies drives embryo elongation. *Elife* 6.

Wallingford, J.B., Niswander, L.A., Shaw, G.M., Finnell, R.H., 2013. The continuing challenge of understanding, preventing, and treating neural tube defects. *Science* 339, 1222002.

West, J.J., Zulueta-Coarasa, T., Maier, J.A., Lee, D.M., Bruce, A.E.E., Fernandez-Gonzalez, R., Harris, T.J.C., 2017. An Actomyosin-Arf-GEF Negative Feedback Loop for Tissue Elongation under Stress. *Curr Biol* 27, 2260-2270 e2265.

Wu, J.Q., Pollard, T.D., 2005. Counting cytokinesis proteins globally and locally in fission yeast. *Science* 310, 310-314.

Wu, S.K., Gomez, G.A., Michael, M., Verma, S., Cox, H.L., Lefevre, J.G., Parton, R.G., Hamilton, N.A., Neufeld, Z., Yap, A.S., 2014. Cortical F-actin stabilization generates apical-lateral patterns of junctional contractility that integrate cells into epithelia. *Nat Cell Biol* 16, 167-178.

Xu, J., Tseng, Y., Wirtz, D., 2000. Strain hardening of actin filament networks. Regulation by the dynamic cross-linking protein alpha-actinin. *J Biol Chem* 275, 35886-35892.

Xue, Z., Sokac, A.M., 2016. Back-to-back mechanisms drive actomyosin ring closure during *Drosophila* embryo cleavage. *J Cell Biol* 215, 335-344.

Yamashiro, S., Totsukawa, G., Yamakita, Y., Sasaki, Y., Madaule, P., Ishizaki, T., Narumiya, S., Matsumura, F., 2003. Citron kinase, a Rho-dependent kinase, induces di-phosphorylation of regulatory light chain of myosin II. *Mol Biol Cell* 14, 1745-1756.

Yang, J., Mani, S.A., Donaher, J.L., Ramaswamy, S., Itzykson, R.A., Come, C., Savagner, P., Gitelman, I., Richardson, A., Weinberg, R.A., 2004. Twist, a master regulator of morphogenesis, plays an essential role in tumor metastasis. *Cell* 117, 927-939.

Yengo, C.M., Takagi, Y., Sellers, J.R., 2012. Temperature dependent measurements reveal similarities between muscle and non-muscle myosin motility. *J Muscle Res Cell Motil* 33, 385-394.

Yu, J.C., Fernandez-Gonzalez, R., 2016. Local mechanical forces promote polarized junctional assembly and axis elongation in *Drosophila*. *Elife* 5.

Zallen, J.A., Wieschaus, E., 2004. Patterned gene expression directs bipolar planar polarity in *Drosophila*. *Dev Cell* 6, 343-355.

Zhou, J., Kim, H.Y., Davidson, L.A., 2009. Actomyosin stiffens the vertebrate embryo during crucial stages of elongation and neural tube closure. *Development* 136, 677-688.

Zhou, J., Pal, S., Maiti, S., Davidson, L.A., 2015. Force production and mechanical accommodation during convergent extension. *Development* 142, 692-701.

Zhu, H., Enaw, J.O., Ma, C., Shaw, G.M., Lammer, E.J., Finnell, R.H., 2007. Association between CFL1 gene polymorphisms and spina bifida risk in a California population. *BMC Med Genet* 8, 12.

Chapter 2. Actomyosin-based tissue folding requires a multicellular myosin gradient

Natalie C. Heer[1], Pearson W. Miller[2,3], Soline Chanet[1], Norbert Stoop[3], Jörn Dunkel[3], Adam C. Martin[1‡]

This chapter was previously published as Heer, N. C. et al. Actomyosin-based tissue folding requires a multicellular myosin gradient. *Development* 144, 1876–1886 (2017). Author contributions: NCH developed the project. NCH and ACM wrote the manuscript. Simulations were performed and Figures 2.7 and 2.8 were created by PWM with advice from JD and NS. SC acquired the Spn 27A and control images. PWM also wrote section 2.3.7 with advice from JD and NS. NCH performed the rest of the experiments, all of the image analysis and made the rest of the figures.

Actomyosin-associated folding of epithelial sheets is a common mode of morphogenesis during the development of complex organs and organisms. Defects in these folding events can lead to congenital birth defects, including spina bifida, which can be caused by failure of the neural plate to fold and fuse (Copp and Greene, 2010; Wallingford et al., 2013). Actomyosin-based epithelial folding is often associated with apical constriction, a process in which apical actomyosin contractility causes columnar epithelial cells to adopt a wedge shape by reducing their apical cell surface area (Martin and Goldstein, 2014). One unanswered question is how apical contractility must be spatially patterned in a tissue to generate three-dimensional (3D) form.

Drosophila gastrulation is a classic example of tissue folding in response to apical constriction. Cells on the ventral side of the embryo fold into the embryo as one of the first tissue rearrangements during development. The domain of invaginating cells is specified by two embryonic transcription factors, *twist* and *snail* (Leptin and Grunewald, 1990; Thisse et al.,

1987). At the time of gastrulation, *snail* expression extends 9 cells from the ventral midline (VM) (to form an 18 cell wide domain) (Ip et al., 1992). *twist* expression extends a few cells further than *snail* (Leptin, 1991). Both genes are initially expressed in a narrower domain of cells that expands over time (Leptin, 1991). Expression of both twist and snail requires the maternal transcription factor dorsal. *twist* is necessary for persistent apical constriction and non-muscle myosin 2 (myosin) accumulation (Mason et al., 2016; Xie and Martin, 2015). Two transcriptional targets of Twist appear to act in parallel to regulate actomyosin contractility in the ventral furrow: *folded gastrulation* (*fog*) and *T48*. Fog is a secreted protein that activates a maternally provided Gα12/13, concertina, through a GPCR pathway (Costa et al., 1994; Kerridge et al., 2016; Manning et al., 2013; Parks and Wieschaus, 1991; Xie et al., 2016). T48 is a transmembrane protein that contains a PDZ-binding consensus motif (Kolsch et al., 2007). T48 and Gα12/13 activation at the apical surface appear to recruit and activate RhoGEF2, a Rho Guanine nucleotide exchange factor with a PDZ domain and a regulator of G protein signaling (RGS) domain (Barrett et al., 1997; Hacker and Perrimon, 1998). There, active RhoGEF2 can activate RhoA (Rho1 in flies), which, in turn, promotes apical actomyosin contractility (Kolsch et al., 2007; Mason et al., 2016). RhoA's effector, ROCK, is required for apical myosin accumulation in the ventral furrow (Dawes-Hoang et al., 2005).

As the tissue folds, there is significant variation in the extent and timing of apical constriction along the ventral-lateral axis of the furrow (Leptin and Grunewald, 1990; Oda et al., 1998; Sweeton et al., 1991) (Fig. 1A). Specifically, cells closer to the VM constrict earlier and to a greater extent than cells farther from the VM, despite the fact that all cells express *twist* prior to constriction (Leptin, 1991). The *twist* target *fog* is transcribed in a subset of ventral cells that extends 6 cells from the VM (Costa et al., 1994); this region corresponds to the region of earliest

constriction (Sweeton et al., 1991). Recently, it was shown that expression of *twist* transcriptional targets, *fog* and *T48* occurs in a graded manner along the ventral-lateral axis (Lim et al., 2017). The intensity profile of myosin during gastrulation has been illustrated at the tissue level, with highest myosin concentrations at the VM (Lim et al., 2017; Spahn and Reuter, 2013). However, whether there are cell-to-cell differences in transcription and active myosin levels and how patterns of transcription and contractility relate to each other is unknown. Most importantly, it is not known whether the variation in apical constriction/contractility is relevant to tissue folding.

Here, we demonstrate that there is a gradient in myosin contractility across the ventral furrow. This gradient starts 2 - 3 cells from the VM and extends to ~ 6 cells from the VM. In this region, 2 - 6 cells from the VM, each subsequent cell has lower levels of active myosin. This contractility gradient originates from the dorsal morphogen gradient, and perturbation of the dorsal morphogen gradient changes the spatial patterning of contractility. Our 3D model of the gastrulating embryo predicts the importance of contractility gradients in generating a tissue fold. Our experimental data validated a prediction of the model: tissue bending was associated with contractile gradients, but not absolute contractility.

2.1. Results

2.1.1. Ventral furrow formation is associated with a multicellular contractility gradient, originating 2-3 cells from the VM.

To determine how tissue-scale contractility is organized in the ventral furrow, we imaged embryos with labeled myosin (sqh::GFP) and membrane (gap43::mCherry) (Martin et al., 2010; Royou et al., 2002). We segmented all images from time-lapse movies of the folding process and partitioned cells into bins based on the initial distance of the cell centroid from the VM

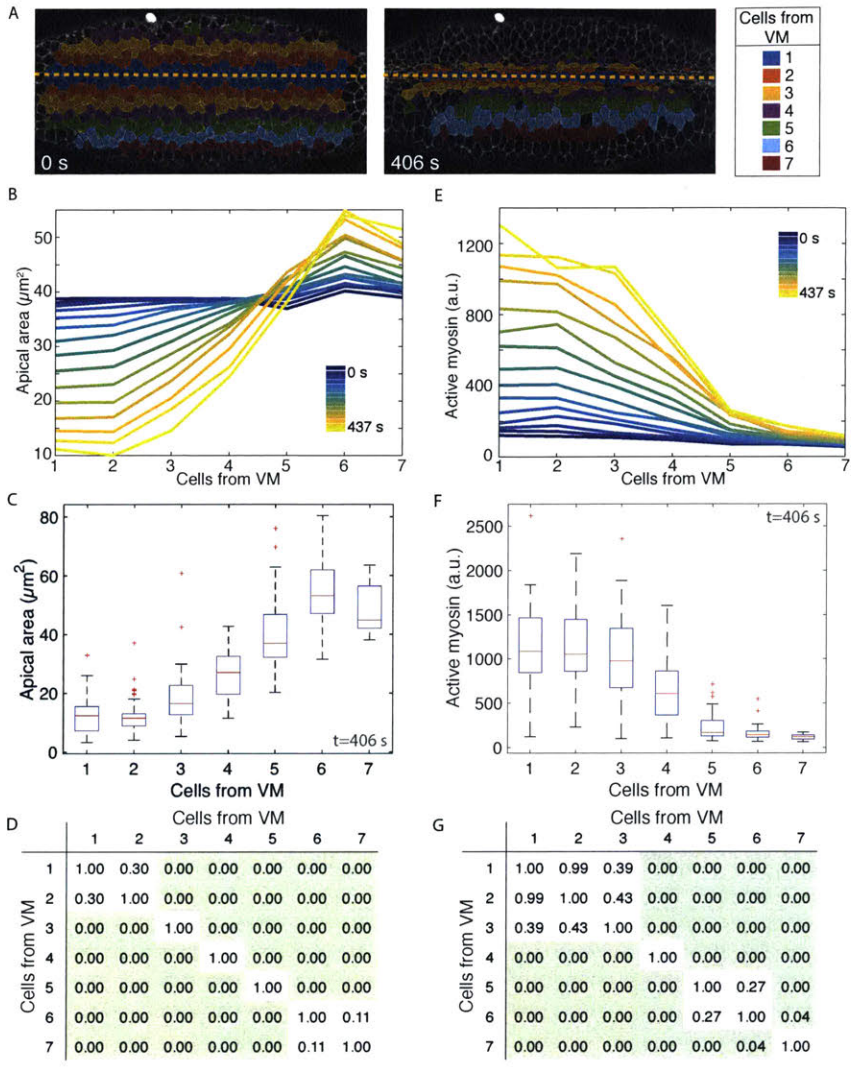

Figure 2.1: Apical area and active myosin intensity are present in a ventral-lateral gradient. (A) Cell position bins relative to the ventral midline (VM, yellow dashed line). (B,E) Apical area (B, y-axis) or total active myosin intensity (E, y-axis) plotted for each ventral-lateral cell position bin (x-axis) for each time frame (color bar) as the embryo furrows. (C,F) Distribution of cell areas (C) or total active myosin intensity (F) for cells in different position bins at time point t=406 s. Red lines indicate median values, box indicates inner quartiles, dashed lines indicate outer quartiles. (D,G) Pairwise statistical comparisons between different cell bins. Tables show P-values from a two-sample Kolmogorov–Smirnov (K–S) test comparing the distribution of apical area (D) and active myosin (G) in each cell bin with every other cell bin. Green shading indicates statistical significance (P<0.05). All data in A-G are from a single embryo. (B,E) n varies for each cell bin and time point. n=17 cells/bin (minimum) and 47 cells/bin (average). (C,D,F,G) n values are 58, 48, 50, 40, 32, 30 and 17 cells (for bins 1-7, respectively).

(example, Fig. 2.1A). As previously observed (Jodoin and Martin, 2016), cells do not intercalate during furrow formation, and cell positions for bins at later time points show the same relative positions as at the initial reference time point (Fig. 2.1A). Thus, we were able to measure cell apical cross-sectional area over time as a function of relative position from the VM.

In agreement with a past live imaging study, which quantified groups of cells (Oda et al., 1998), we found that apical area reduction was not uniform along the ventral-lateral axis. Prior to the onset of constriction, all cells along the ventral-lateral axis had an apical area of

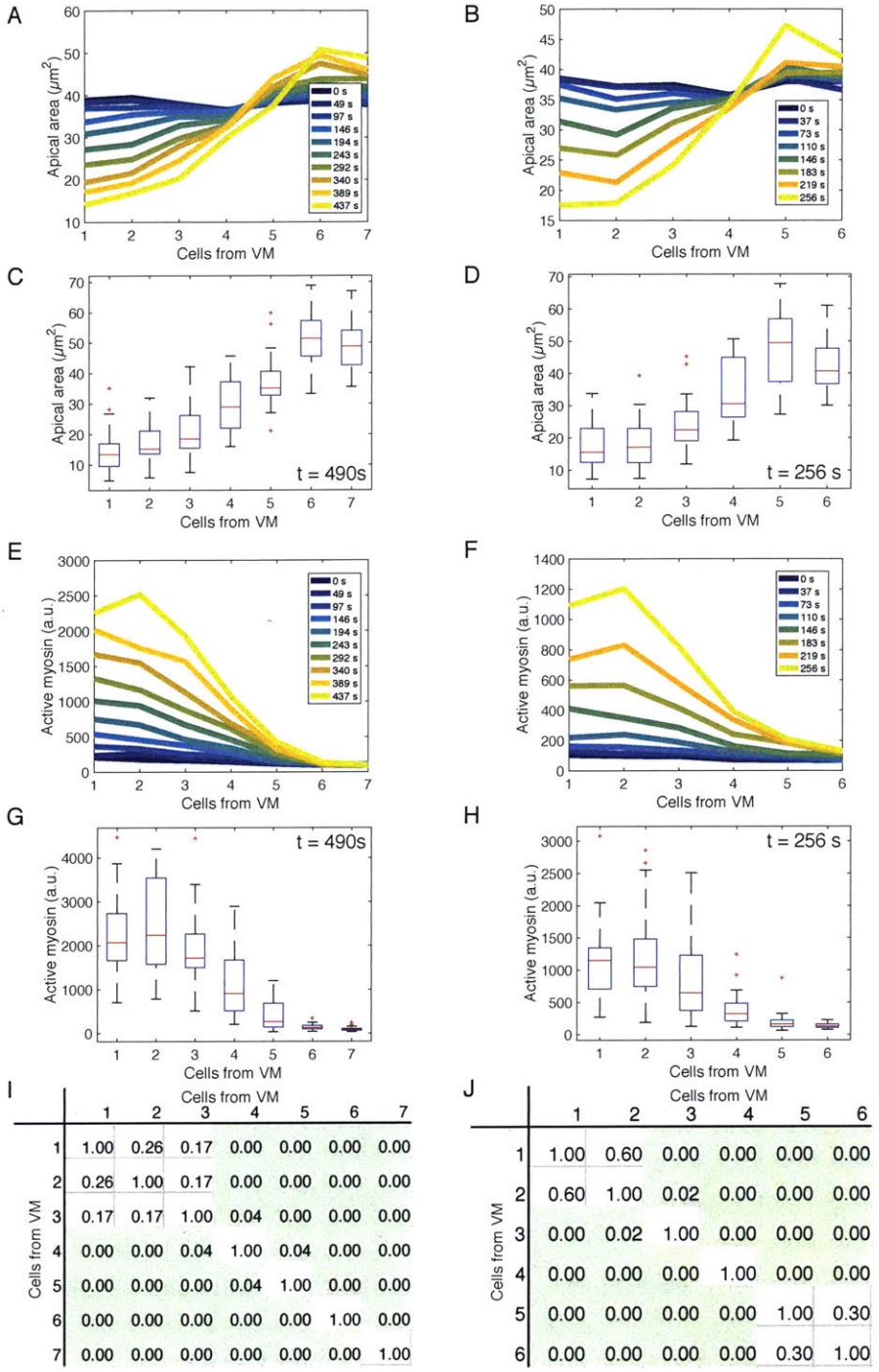

Cells from VM	1	2	3	4	5	6	7
1	1.00	0.26	0.17	0.00	0.00	0.00	0.00
2	0.26	1.00	0.17	0.00	0.00	0.00	0.00
3	0.17	0.17	1.00	0.04	0.00	0.00	0.00
4	0.00	0.00	0.04	1.00	0.04	0.00	0.00
5	0.00	0.00	0.00	0.04	1.00	0.00	0.00
6	0.00	0.00	0.00	0.00	0.00	1.00	0.00
7	0.00	0.00	0.00	0.00	0.00	0.00	1.00

Cells from VM	1	2	3	4	5	6
1	1.00	0.60	0.00	0.00	0.00	0.00
2	0.60	1.00	0.02	0.00	0.00	0.00
3	0.00	0.02	1.00	0.00	0.00	0.00
4	0.00	0.00	0.00	1.00	0.00	0.00
5	0.00	0.00	0.00	0.00	1.00	0.30
6	0.00	0.00	0.00	0.00	0.30	1.00

Figure 2.2: Apical area and active myosin intensity are present in a ventral-lateral gradient in two *wild type* embryos. **(A–B)** Increase in total active myosin intensity per cell is graded along the ventral-lateral axis in *wild type* embryos. Average total apical myosin intensity per cell (y-axis) is plotted for each cell position bin (x-axis) for each time frame (colorbar). **(C–D)** Distribution of levels of active myosin per cell for each cell bin show a gradient in the average cell behavior at t = 490 s (C) and t = 256 s (D). **(E–F)** Statistical significance of pairwise comparisons between distributions of active myosin levels in cell bins at different positions from the VM from (C) and (D) respectively. Tables show p-values (K-S test). Green indicates $p<0.05$. **(G–H)** Apical constriction is graded along the ventral-lateral axis in WT embryos. Apical area (y-axis) is plotted for each cell position bin (x-axis) for each time frame (colorbar) as each embryo furrows. **(I–J)** Distribution of cell areas for cell bin at a late time point highlights the gradient at t = 430 s (I) and t = 438 s (J). (A, C, E, G, and I) are measurements from one *Rh3-RNAi* embryo. n varies for each cell bin and time point. n = 26 cells/bin (minimum) and 49 cells/bin (average). (B, D, F, H, and J) are measurements from a second WT embryo. n varies for each cell bin and time point. n = 10 cells/bin (minimum) and 53 cells/bin (average).

approximately 40 μm² (Fig. 2.1B and 2.2A,B, blue curves). Over time, cells within 4 cells of the

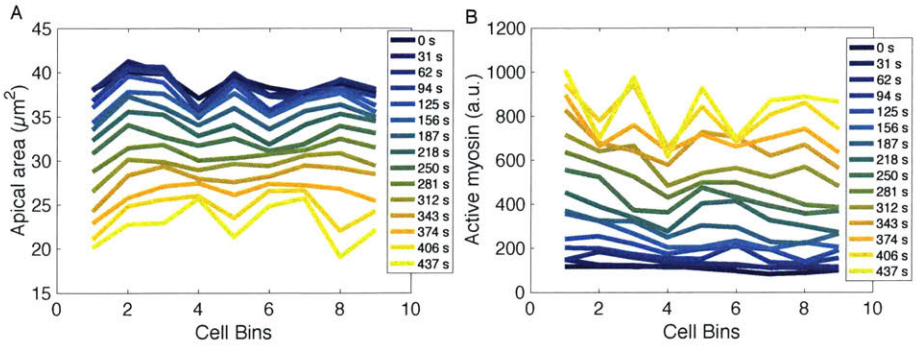

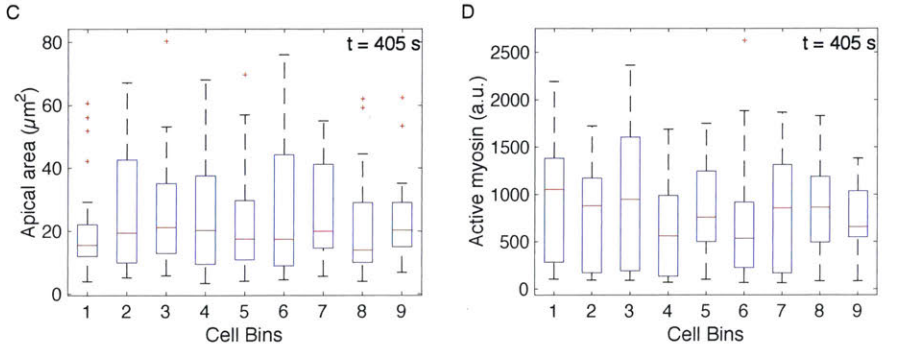

E

Cell Bins	1	2	3	4	5	6	7	8	9
1	1.00	0.64	0.77	0.20	0.83	0.02	0.52	0.59	0.14
2	0.64	1.00	0.80	0.92	0.79	0.17	0.99	0.77	0.86
3	0.77	0.80	1.00	0.32	0.42	0.08	0.67	0.75	0.32
4	0.20	0.92	0.32	1.00	0.20	0.89	0.78	0.20	0.27
5	0.83	0.79	0.42	0.20	1.00	0.26	0.32	0.93	0.58
6	0.02	0.17	0.08	0.89	0.26	1.00	0.50	0.26	0.21
7	0.52	0.99	0.67	0.78	0.32	0.50	1.00	0.49	0.60
8	0.59	0.77	0.75	0.20	0.93	0.26	0.49	1.00	0.59
9	0.14	0.86	0.32	0.27	0.58	0.21	0.60	0.59	1.00

F

Cell Bins	1	2	3	4	5	6	7	8	9
1	1.00	0.49	0.32	0.84	0.49	0.76	0.28	0.59	0.16
2	0.49	1.00	0.33	0.94	0.70	0.98	0.13	0.96	0.04
3	0.32	0.33	1.00	0.94	0.84	0.40	0.64	0.34	0.79
4	0.84	0.94	0.94	1.00	0.87	0.94	0.70	0.59	0.41
5	0.49	0.70	0.84	0.87	1.00	0.57	0.59	0.72	0.40
6	0.76	0.98	0.40	0.94	0.57	1.00	0.13	0.77	0.04
7	0.28	0.13	0.64	0.70	0.59	0.13	1.00	0.22	0.39
8	0.59	0.96	0.34	0.59	0.72	0.77	0.22	1.00	0.06
9	0.16	0.04	0.79	0.41	0.40	0.04	0.39	0.06	1.00

Figure 2.3: Apical area and apical myosin do not exhibit a gradient along the anterior-posterior axis. (A) Apical area in a wild-type embryo (same as in Fig. 1). Apical area (y-axis) is plotted for each anterior-posterior (AP) cell bin (x-axis) for each time frame (colorbar) as the embryo furrows. (B) Apical myosin in the same embryo as (A). Average total apical myosin intensity per cell (y-axis) is plotted for each cell position bin (x-axis) for each time frame (colorbar). (C) and (D) the distribution of apical cells area (C) and active myosin (D) at t = 405 s. Red lines indicate median values, box indicates inner quartiles, while dotted lines indicate outer quartiles. (E) Apical area distributions at t = 405 s are not statistically different from each other. (F) Active myosin distributions at t = 405 s are for the most part not significantly different from each other. (E) and (F) Tables show p-values (K–S test) comparing the distribution of apical area (E) and active myosin (F) between each pair of cell bins. Green shading indicates statistical significance with $p<0.05$. Bins in (A) and (B) are the same. n varies for each cell bin and time point. n = 3 cells/bin (minimum) and 13 cells/bin (average)

VM reduced their apical area and cells farther than 5 cells from the VM expanded their apical area (Fig. 2.1B and 2.2A,B, blue to yellow curves). At late time points, the apical area distributions for the 2 cells adjacent to the VM were not statistically different, but each subsequent cell from the VM had significantly larger apical area until 6 cells from the VM (Fig. 2.1C,D and 2.2C,D). We refer to this pattern in the resulting apical area as a gradient in apical constriction. Differences in cell area were not seen when cells were binned based on their

position along the orthogonal anterior-posterior axis of the embryo, demonstrating that the apical constriction gradient occurs mainly along the ventral-lateral axis (Fig. 2.3).

To measure the levels of 'active' myosin in the cell apex, we have used an image processing method to capture activated, cortical myosin molecules and exclude cytoplasmic, 'inactive' myosin (see Methods). Several arguments support the fact that we have measured active myosin: 1) *Drosophila* myosin 2 can exist either as a single molecule in an inactive, folded conformation or as an active bipolar filament consisting of 12 molecules, depending on phosphorylation of its regulatory light chain (Vasquez et al., 2016), 2) Inhibition of ROCK, a kinase that phosphorylates and activates myosin filament formation and motor activity, results in the immediate dissolution (in 10 – 15 seconds) of the intense cortical myosin structures that we measure (Coravos and Martin, 2016), and 3) The amount of myosin that we measured using this method is well-correlated with apical constriction in single cells (Martin et al., 2009; Xie and Martin, 2015). For all of these reasons, we conclude that the intensity of the cortical myosin structures measured in this study represent active myosin.

We found that there was a cellular gradient in active myosin that accompanied ventral furrow formation. Specifically, active myosin intensity distributions were highest on average in the two cells adjacent to the VM (Fig. 2.1E-G and 2.2E-H). The average amount of active myosin in the third cell from the VM was often lower, but this was not always statistically significant (Fig. 2.1E-G and 2.2G-J). Beginning three cells from the VM every subsequent cell position consistently exhibited a significantly lower active myosin distribution than the one before (Fig. 2.1F,G, and 2.2G-J). Thus, there is a multicellular gradient in myosin activity that starts 2 - 3 cells from the VM and extends to 6 cells from the VM. We refer to this as a ventral-lateral contractility gradient.

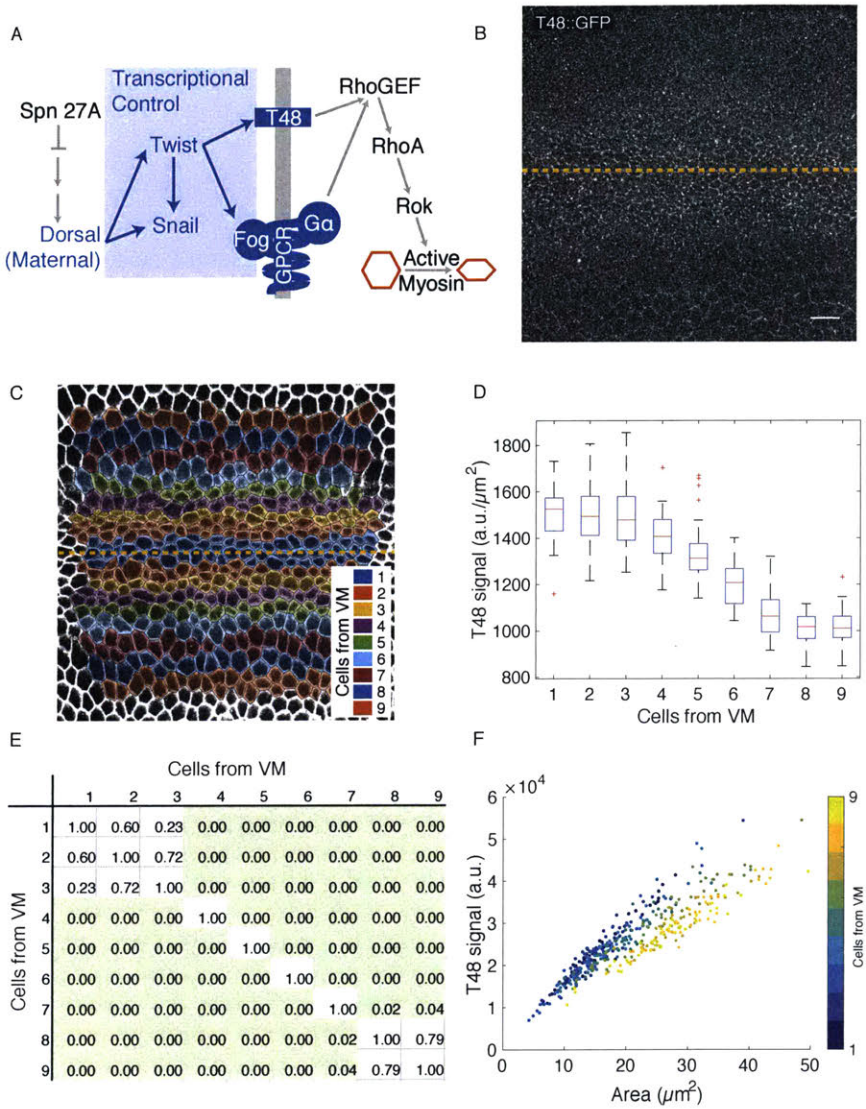

Figure 2.4: T48::GFP signal density is graded three to eight cells from the VM. **(A)** Schematic of the signaling pathway that promotes apical constriction. Gray line represents apical membrane. GPCR, G protein-coupled receptor. **(B)** Image of GFP::T48 (anti-GFP) embryo with VM centered (dashed yellow line). **(C)** Cell bins (colored) manually determined in a fixed embryo. Image is of a phalloidin-stained embryo. **(D)** GFP::T48 density (fluorescence intensity μm^{-2}) (y-axis) as a function of position from the VM (x-axis, see C). **(E)** Pairwise statistical comparisons between different cell bins. Table shows p-values (K–S test) from (D). Green indicates $p<0.05$. **(F)** Total GFP::T48 signal per cell (y-axis) as a function of apical cell area (x-axis). Cell bin is denoted (color bar). (B-F) n is one embryo and 45, 43, 44, 44, 44, 47, 50, 51 and 50 cells (for bins 1–9, respectively). Scale bar: 10 μm.

2.1.2. An upstream regulator of contractility, T48, exists in a gradient

To determine the source of the active myosin gradient, we examined an upstream component of the signaling pathway that regulates ventral furrow formation, the integral membrane protein T48 (Fig. 2.4A). We engineered a T48 allele with an internal GFP tag. The GFP::T48 fusion allele was expressed from the endogenous T48 promoter using bacterial artificial chromosome-mediated recombineering (Venken et al., 2006). GFP::T48 was visualized in fixed embryos stained with a GFP antibody (Fig. 2.4B). We segmented the image based on

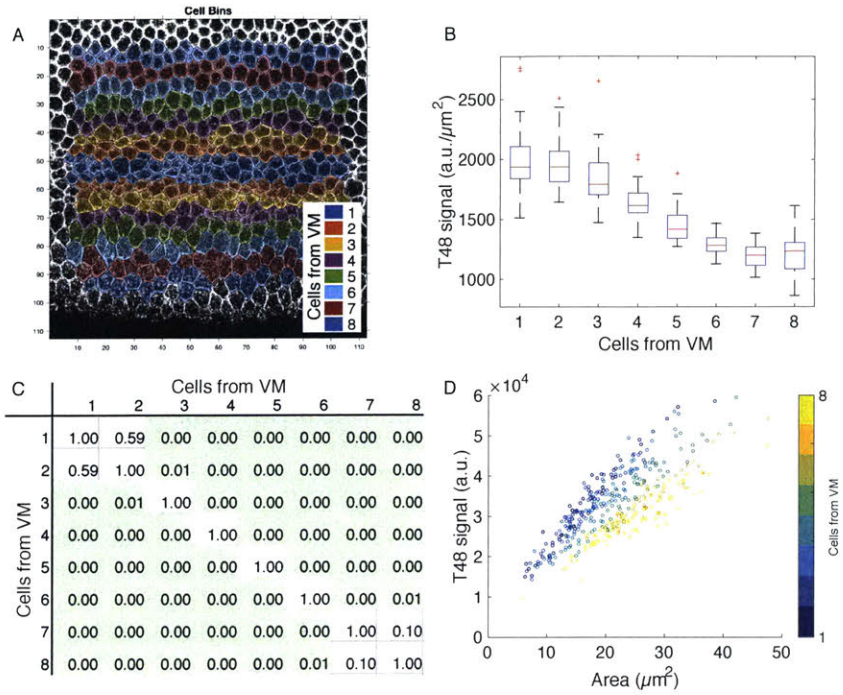

Figure 2.5: T48::GFP signal density exhibits graded levels 3–7 cells from VM in a second T48::GFP expressing embryo. (A) Cell bins as manually determined in fixed embryo. Images show cell outlines (phalloidin stain). Colors indicate cell bin. Colors repeat after 7 bins. (B) Average T48 signal density is graded along the ventral-lateral axis with highest levels at the VM. GFP::T48 density (fluorescence intensity μm^{-2}) (y-axis) as a function of cells from the VM (x-axis) (See (A) for illustration of cell bins. (C) A statistically significant gradient in T48 levels is observed from 2–7 cells from the VM. p-values (K–S test) generated from cell bins in (B). Green indicates $p<0.05$ (D) Total GFP::T48 signal per cell is higher in cells closer to the VM for a given cell area. Total GFP::T48 signal per cell (y-axis) as a function of apical cell area (x-axis). Cell bin is denoted (colorbar). (B-D) show measurements from a single embryo. n= 42 (minimum) n=53 (maximum).

phalloidin staining and binned cells with respect to their position from the VM (Fig. 2.4C and 2.5A). We found that average signal density of GFP::T48 is highest in cells closest to the VM (Fig. 2.4D and 2.5B). Similar to the distribution of active myosin, a difference in T48 levels first appears between cells 3 and 4 from the VM. The gradient in T48 seems to extend slightly further than the gradient in myosin (encompassing 7 - 8 cells on either side of the midline) (Fig. 2.4D,E and 2.5B,C). The fact that there is a T48 gradient is consistent with the myosin gradient resulting from upstream signals.

The measured gradient in T48::GFP signal density (a.u. per μm^2) could reflect the gradient in apical constriction, and not a gradient in T48 gene expression. As cells apically constrict, T48::GFP on apical membranes could be concentrated. To test this we measured the total amount of T48 at the apical surface of a cell. We found that total signal is strongly

correlated with cell area possibly due to a low signal to noise ratio (Fig. 2F). However, for cells of a given area, cells closest to the VM have a higher level of total T48::GFP signal, suggesting that differential expression of T48 accounts for at least some of the difference in signal density (Fig. 2F blue vs yellow points). This is supported by recent work measuring T48 expression in the ventral domain that found that T48 and fog, another twist target, are expressed earlier in cells closest to the VM (Lim et al., 2017). Our data demonstrates that between 3 - 7 cells from the VM there are differences in both T48 density and overall levels, in a pattern that mirrors active myosin.

2.1.3. twist mRNA is present in a gradient at the onset of cycle 14

It has been previously shown that Dorsal, the maternal morphogen that is required for *twist* transcription, is active in a gradient along the ventral-lateral axis with highest nuclear levels in the most ventral cells (Fig. 2.4A) (Kanodia et al., 2009; Reeves et al., 2012). *twist* expression levels have previously been described as being uniform across the central region of the ventral furrow with a gradient of *twist* at the edge of the furrow, where cells stretch (Leptin, 1991). We measured *twist* mRNA levels at the beginning of nuclear cycle 14, about an hour before gastrulation, using quantitative fluorescence in situ hybridization (FISH). We found that *twist* mRNA was detected as small puncta in the cytoplasm of ventral cells (Fig. 2.6A). We measured *twist* mRNA levels by quantifying the mean intensity of the *twist* FISH signal in the cytoplasm adjacent to each nucleus (McHale et al., 2011). At early nuclear cycle 14, twist is expressed in a gradient around the VM. The gradient begins 2-3 cells from the VM and extends to about 12 cells from the VM (Fig. 2.6B,C). Early differences in *twist* levels are consistent with, and could explain, the later differences in transcription and downstream signaling measured in this paper

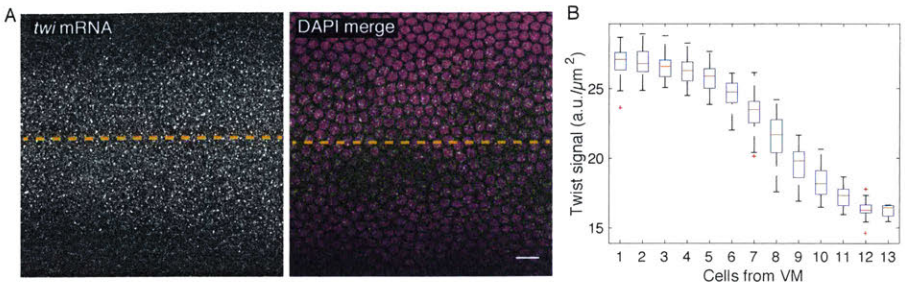

C

Cells from VM	1	2	3	4	5	6	7	8	9	10	11	12	13
1	1.00	0.30	0.01	0.00	0.00	0.00	0.00	0.00	0.00	0.00	0.00	0.00	0.00
2	0.30	1.00	0.05	0.07	0.00	0.00	0.00	0.00	0.00	0.00	0.00	0.00	0.00
3	0.01	0.05	1.00	0.60	0.00	0.00	0.00	0.00	0.00	0.00	0.00	0.00	0.00
4	0.00	0.07	0.60	1.00	0.06	0.00	0.00	0.00	0.00	0.00	0.00	0.00	0.00
5	0.00	0.00	0.00	0.06	1.00	0.00	0.00	0.00	0.00	0.00	0.00	0.00	0.00
6	0.00	0.00	0.00	0.00	0.00	1.00	0.00	0.00	0.00	0.00	0.00	0.00	0.00
7	0.00	0.00	0.00	0.00	0.00	0.00	1.00	0.00	0.00	0.00	0.00	0.00	0.00
8	0.00	0.00	0.00	0.00	0.00	0.00	0.00	1.00	0.00	0.00	0.00	0.00	0.00
9	0.00	0.00	0.00	0.00	0.00	0.00	0.00	0.00	1.00	0.00	0.00	0.00	0.00
10	0.00	0.00	0.00	0.00	0.00	0.00	0.00	0.00	0.00	1.00	0.00	0.00	0.00
11	0.00	0.00	0.00	0.00	0.00	0.00	0.00	0.00	0.00	0.00	1.00	0.00	0.01
12	0.00	0.00	0.00	0.00	0.00	0.00	0.00	0.00	0.00	0.00	0.00	1.00	0.95
13	0.00	0.00	0.00	0.00	0.00	0.00	0.00	0.00	0.00	0.00	0.01	0.95	1.00

Figure 2.6: *twist* mRNA expression is graded 3-12 cells from VM at early nuclear cycle 14. (A) Images show *twist* mRNA (left) or *twist* mRNA and DAPI (green and magenta, respectively) in single z-slices, *en face*, just apical to cortical nuclei. Dashed line indicates VM. (B) Cytoplasmic *twist* signal (y-axis, fluorescence intensity/μm2) plotted as a function of position from the VM (x-axis, determined by average cell diameter). (C) Pairwise statistical comparisons between cell bins in (B). p-values recorded (K–S test). Green indicates $p<0.05$. n is one embryo with 45, 43, 44, 44, 44, 47, 50, 51, 50, 50, 56, 30 and 5 cells (for bins 1-13, respectively). Scale bar: 10 μm.

and previously (Costa et al., 1994). Time delays due to transcription of target genes and the translation of Twist and target genes could explain the delay between the measurement of *twist* mRNA and the downstream gradients. Thus, there is an early, transient gradient in *twist* mRNA levels that could explain the subsequent gradient in apical T48 levels, myosin activity, and contractility.

2.1.4. Mechanical model demonstrates that contractile gradients promote curvature

To understand the mechanisms underlying furrow formation by contractility gradients, we studied a 3D continuum model of the *Drosophila* embryo during gastrulation. At this developmental stage, the embryo consists of a thin, single-layer epithelial sheet of approximately ellipsoid shape. Its mechanics can be described mathematically by an elastic shell (Koiter shell model, (Ciarlet, 2000)), represented by its middle surface (Fig. 2.7A and 2.7B, dotted line); for further explanation see Materials and Methods. Passive mechanical stresses appear whenever the

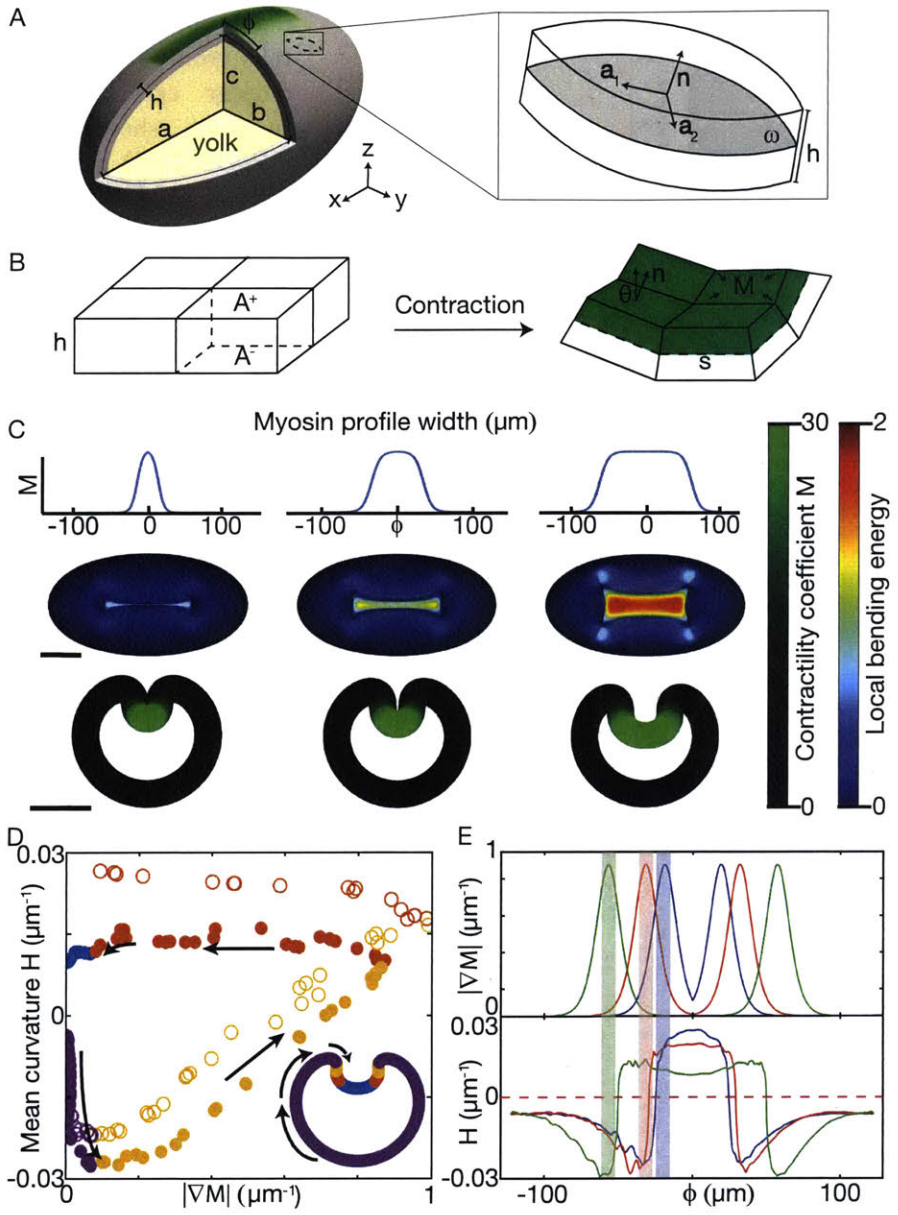

Figure 2.7: Continuum mechanical model associates curvature with contractility gradients. **(A)** Ellipsoid model schematic with surface tangents (a_1 and a_2) and normal (n). w is distance from VM. **(B)** Schematic showing how contractility (M) on surface A^+ changes the preferred curvature. **(C)** Profiles of M (top) used for simulation, with w = 19 μm (left), w = 31 μm (middle) and w = 56 μm (right), and the resulting shape (bottom). In each case, steepness parameter k=0.19 μm^{-1} and M_0=30. Bending energy (color bar) is a proxy for the difference between local preferred and actual curvature (Materials and Methods). Scale bars: 100 μm. **(D)** Mean curvature of the middle plane as a function of the gradient in contractility (M) for small w (open circles) and large w (closed circles). Although the VM has the highest concentration of myosin, there is no contractility gradient and no further increase in curvature (blue). **(E)** Myosin gradient (top) aligned with maximum curvature (bottom) as a function of w. The location of peak contractility M is highlighted with shaded bars. Blue line corresponds to leftmost simulation in C, red to the middle simulation and green to the rightmost.

middle-surface geometry deviates from its original shape by local stretching or bending deformations. Active stresses from apical constriction were incorporated into this model by modifying the local preferred curvature of the middle surface (mimicking constriction at the apical surface); these cause active bending moments that drive furrow formation (Fig. 2.7B).

This is analogous to the bending of bimetallic strips, which assume a curved state when one of the two adjacent layers expands less strongly than the other in the presence of a thermal stimulus (Timoshenko, 1925). Similarly, apical contraction is expected to create a preferred tissue curvature. To relate the local myosin activity to active stress generation, we analyzed how apical constriction affects preferred curvature in a vertex-based cell model (Fig. 2.7B). This allowed us to relate active stresses to a dimensionless parameter $\boldsymbol{M}$. $\boldsymbol{M}$ measures the relative strength of active and passive stresses and fully determines the induced shape deformation. The parameter $\boldsymbol{M}$ can thus be understood as a dimensionless contractility coefficient that is proportional to the local myosin activity. This theoretical framework allowed us to efficiently study spatial patterns of contractility and compare the predicted 3D shell shapes against our experimental data for wild-type and mutant embryos.

Guided by our myosin activity measurements in wild-type embryos, we approximated the contractility profile as $M(\varphi) = M_0(1 + e^{-kw}) / (1 + e^{k(|\varphi|-w)})$. Here, φ is the distance from the VM, M_0 denotes the maximum value of M (assumed at $\varphi = 0$), k is a steepness coefficient characterizing the profile decay, and w is the width of the profile (Fig. 2.7C). We adjusted k, M_0, and w to fit the distribution of myosin and apical constriction that we observed in wild-type embryos.

To test whether the gradient in contractility was important for folding, we compared furrow formation in the model for increasing values of w (Fig. 2.7C). For low values of w, we observed furrows that were morphologically similar to those of wild-type embryos (Fig. 2.7C, left and middle). Increasing w increased the width of the region of contractility and resulted in a region around $\varphi = 0$ where the contractility profile is flat (Fig. 2.7C, right). Simulated

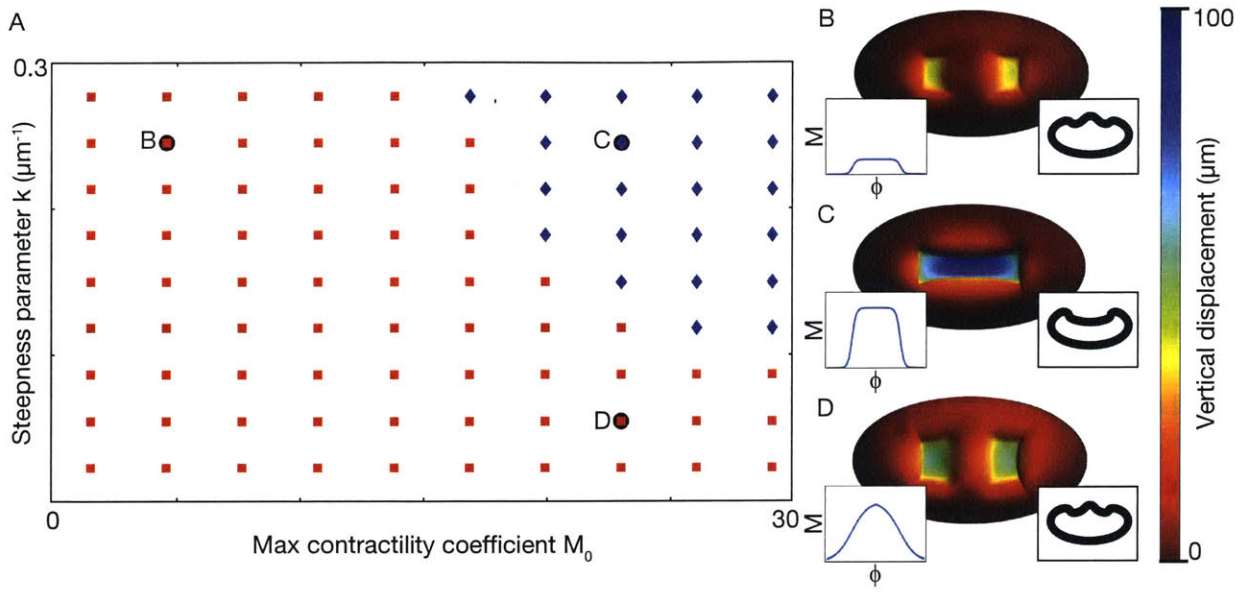

Figure 2.8: Parameter scan shows folding requires increased contractility and a contractility gradient. (A) Phase diagram showing parameters for which a furrow forms (blue) and for which a furrow fails to form (red). Letters indicate parameters that correspond to the examples in B-D. (B) Low contractility parameter, M_0=6, does not furrow. (C) High contractility and presence of gradient (M_0=24 and k=0.256 μm^{-1}, respectively) results in furrow. (D) Low steepness parameter, k=0.064 μm^{-1}, does not furrow. Insets indicate M as a function of w and cross-section views along the long axis of the ellipsoid. In each case, width w=43 μm.

equilibrium shapes showed that, as the distance between regions of graded contractility increased, the furrow width also increased, leaving a relatively flat surface in the region of uniform contractility (Fig. 2.7C). Importantly, changes in shell curvature were associated with the position of the gradient in M (Fig. 2.7D). This was the case regardless of the width of the myosin profile. Changes in shell curvature always occurred near the boundary where there was a gradient in M. In contrast, where there was an extended region of uniform M, curvature was low (Fig. 2.7D,E).

We next explored how our model responded to changes in M_0 and k; i.e., the level of contractility and steepness of the contractility gradient, respectively. We found that with low contractility M_0, but normal steepness k, our model does not form a furrow (Fig. 2.8A,B). Additionally, in our model, having high contractility M_0, but a low steepness k for the gradient,

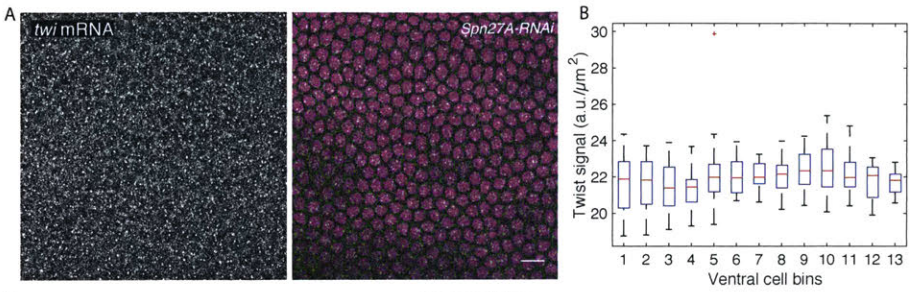

C

Ventral cell bins	1	2	3	4	5	6	7	8	9	10	11	12	13
1	1.00	0.95	0.82	0.04	0.07	0.08	0.13	0.35	0.26	0.28	0.28	0.55	0.13
2	0.95	1.00	0.80	0.09	0.22	0.13	0.29	0.47	0.36	0.30	0.42	0.75	0.13
3	0.82	0.80	1.00	0.15	0.06	0.05	0.08	0.23	0.13	0.18	0.07	0.35	0.08
4	0.04	0.09	0.15	1.00	0.02	0.07	0.05	0.02	0.00	0.01	0.10	0.06	0.15
5	0.07	0.22	0.06	0.02	1.00	0.99	0.63	0.89	0.36	0.47	0.93	0.88	0.37
6	0.08	0.13	0.05	0.07	0.99	1.00	0.89	0.92	0.67	0.64	0.96	0.59	0.44
7	0.13	0.29	0.08	0.05	0.63	0.89	1.00	0.98	0.27	0.48	0.94	0.91	0.71
8	0.35	0.47	0.23	0.02	0.89	0.92	0.98	1.00	0.30	0.69	0.98	0.93	0.30
9	0.26	0.36	0.13	0.00	0.36	0.67	0.27	0.30	1.00	0.74	0.54	0.13	0.02
10	0.28	0.30	0.18	0.01	0.47	0.64	0.48	0.69	0.74	1.00	0.57	0.50	0.14
11	0.28	0.42	0.07	0.10	0.93	0.96	0.94	0.98	0.54	0.57	1.00	0.90	0.71
12	0.55	0.75	0.35	0.06	0.88	0.59	0.91	0.93	0.13	0.50	0.90	1.00	0.57
13	0.13	0.13	0.08	0.15	0.37	0.44	0.71	0.30	0.02	0.14	0.71	0.57	1.00

Figure 2.9: *twist* mRNA expression is uniform around the VM in a *Spn27A-RNAi* embryo. (A) *twist* mRNA at early nuclear cycle 14 in a *Spn27A-RNAi* embryo. Images are single z-slices, *en face*, at the level of the nuclei. Left image shows *twist* mRNA staining and right image is a merge of the *twist* mRNA in green and DAPI in magenta. (B) Cytoplasmic *twist* mRNA signal is uniform around the VM. Cytoplasmic *twist* mRNA signal (fluorescence intensity/μm^2) is plotted as a function of cells from the VM (x-axis) (determined by average cell diameter). (C) There is no statistically significant gradient in levels of *twist* mRNA. p-values (K–S test) comparing the distribution of *twist* (a.u. μm^{-2}) in each cell bin from (B). Green indicates $p<0.05$. Data from one embryo is presented. n of cells for each bin (1-13) is 23, 16, 19, 22, 21, 21, 21, 23, 20, 23, 19, 19, and 20 respectively. Scale bars = 10 μm.

also fails to form a furrow and instead results in an hour-glass-shaped flattened depression (Fig. 2.8A,D). Only when both M_0 and k are above a certain threshold will the model form a furrow. Thus, our model predicts that furrow formation in embryos will fail if either the total activity of active myosin or the steepness of the gradient is too small.

2.1.5. Experimental flattening of the active myosin gradient in vivo disrupts tissue curvature.

Our 3D model simulations predicted that tissue folding occurs where there is a gradient in contractility. To show that uniform levels of active myosin were insufficient to cause tissue bending, we attempted to flatten the active myosin gradient in vivo using a genetic perturbation. Spn27A is a negative regulator of ventral cell fate in the *Drosophila* embryo (Fig. 2.4A). Hypomorphic alleles of *Spn27A* and depletion of *Spn27A* using RNA interference (*RNAi*) have been shown to increase the width of the ventral domain (Jodoin et al., 2015; Ligoxygakis et al.,

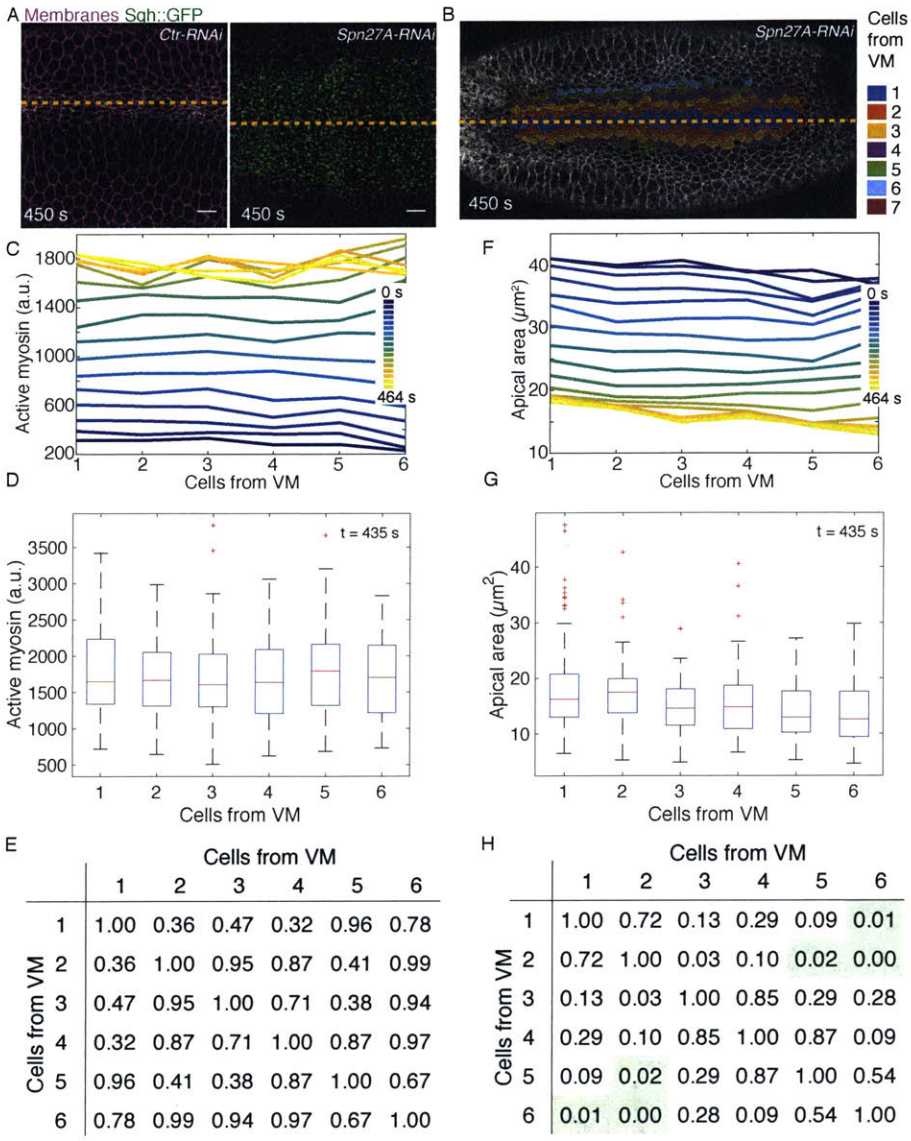

Figure 2.10: Active myosin gradient is dependent on dorsal patterning. **(A)** Apical surface projection (see Materials and Methods) showing myosin (Sqh::GFP) and membrane (Gap43::mCherry) in *Rh3*-RNAi (Ctr-RNAi) or *Spn27A*-RNAi embryos. **(B)** Cell outlines (Gap43::mCherry) and cell position bins, relative to VM (yellow line). **(C,F)** Plots of average active myosin intensity (C) or apical area (F) as a function of position from VM. Different color lines are different time points. **(D,G)** Distributions of active myosin (D) and apical area (G) for cell position bins at 435 s time point. Red lines indicate median value, boxes indicate inner quartiles, dashed lines indicate outer quartiles. **(E,H)** Tables of P-values generated from a two-sample K–S test comparing the distribution of active myosin (E) or apical area (H) in each cell bin with every other cell bin. Green indicates $p<0.05$. Data shown in A-H are from the same *Spn27A*-RNAi embryo. *Ctr*-RNAi image is from the embryo quantified in Fig. 2.11A,C,E,G,I. n=17 cells/bin (minimum) and 50 cells/bin (average). Scale bars: 10 μm.

2003). We hypothesized that increasing Dorsal activity could lead to an extended region of uniform Dorsal activity around the VM. We first tested the effect of *Spn27A* depletion on the upstream gradient in *twist* mRNA and found that, as expected, *twist* expression levels were uniform in an expanded region around the VM in *Spn27A-RNAi* embryos (Fig. 2.9). We next examined the effect of *Spn27A* depletion on the contractility gradient, and found that the region

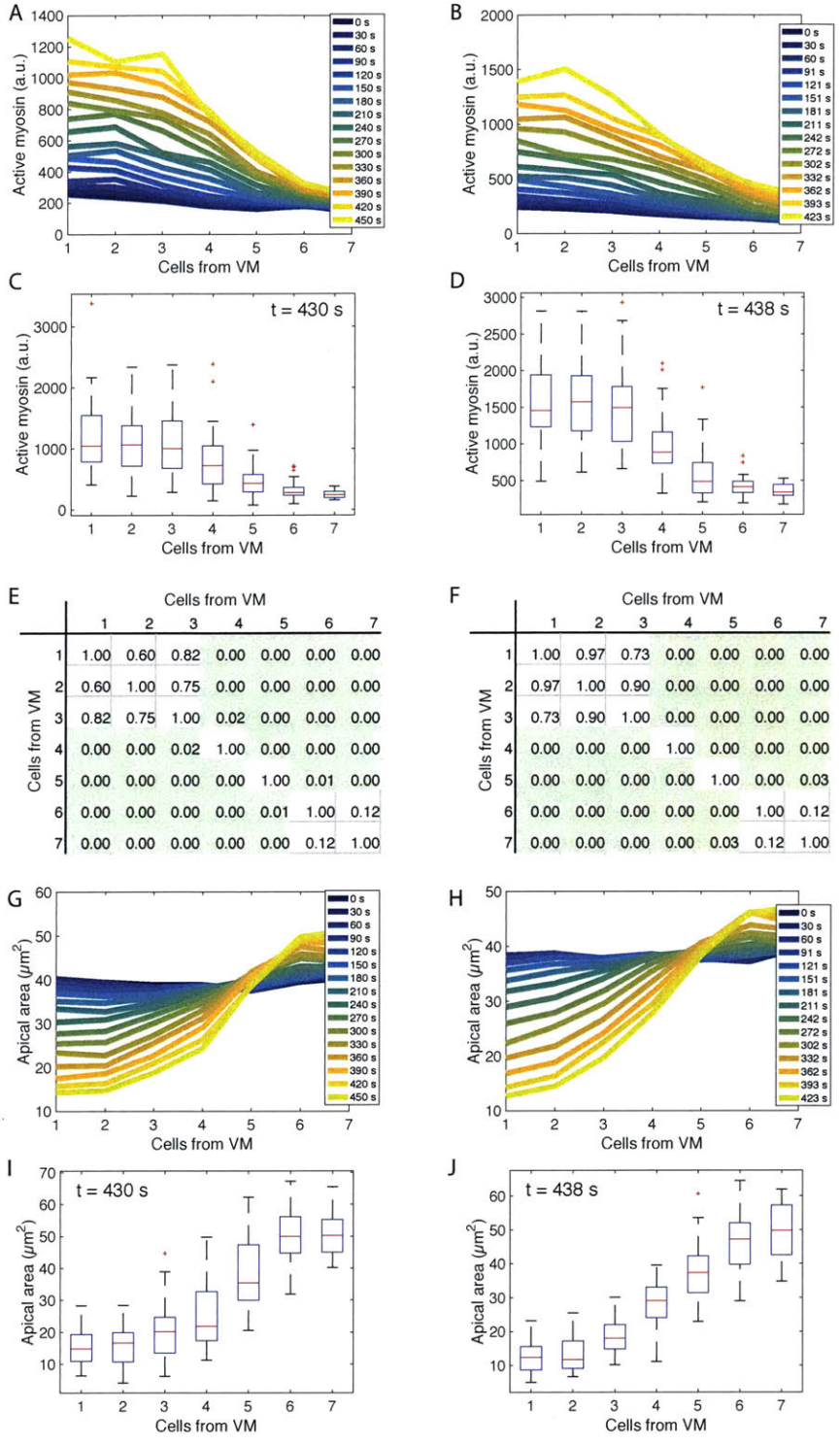

Cells from VM	1	2	3	4	5	6	7
1	1.00	0.60	0.82	0.00	0.00	0.00	0.00
2	0.60	1.00	0.75	0.00	0.00	0.00	0.00
3	0.82	0.75	1.00	0.02	0.00	0.00	0.00
4	0.00	0.00	0.02	1.00	0.00	0.00	0.00
5	0.00	0.00	0.00	0.00	1.00	0.01	0.00
6	0.00	0.00	0.00	0.00	0.01	1.00	0.12
7	0.00	0.00	0.00	0.00	0.00	0.12	1.00

Cells from VM	1	2	3	4	5	6	7
1	1.00	0.97	0.73	0.00	0.00	0.00	0.00
2	0.97	1.00	0.90	0.00	0.00	0.00	0.00
3	0.73	0.90	1.00	0.00	0.00	0.00	0.00
4	0.00	0.00	0.00	1.00	0.00	0.00	0.00
5	0.00	0.00	0.00	0.00	1.00	0.00	0.03
6	0.00	0.00	0.00	0.00	0.00	1.00	0.12
7	0.00	0.00	0.00	0.00	0.03	0.12	1.00

Figure 2.11: Apical area and active myosin intensity are present in a ventral-lateral gradient in two *Rh3-RNAi* embryos. (A–B) Increase in total active myosin intensity per cell is graded along the ventral-lateral axis in *Rh-3-RNAi* (control) embryos. Average total apical myosin intensity per cell (y-axis) is plotted for each cell position bin (x-axis) for each time frame (colorbar). **(C–D)** Distribution of levels of active myosin per cell for each cell bin show a gradient in the average cell behavior at t = 430 s (C) and t = 438 s (D). **(E–F)** Statistical significance of pairwise comparisons between distributions of active myosin levels in cell bins at different positions from the VM from (C) and (D) respectively. Tables show p-values (K-S test). Green indicates $p < 0.05$. **(G–H)** Apical constriction is graded along the ventral-lateral axis in WT embryos. Apical area (y-axis) is plotted for each cell position bin (x-axis) for each time frame (colorbar) as each embryo furrows. **(I–J)** Distribution of cell areas for cell bin at a late time point highlights the gradient at t = 430 s (I) and t = 438 s (J). (A, C, E, G, and I) are measurements from one *Rh3-RNAi* embryo. n varies for each cell bin and time point. n = 26 cells/bin (minimum) and 49 cells/bin (average). (B, D, F, H, and J) are measurements from a second WT embryo. n varies for each cell bin and time point. n = 10 cells/bin (minimum) and 53 cells/bin (average).

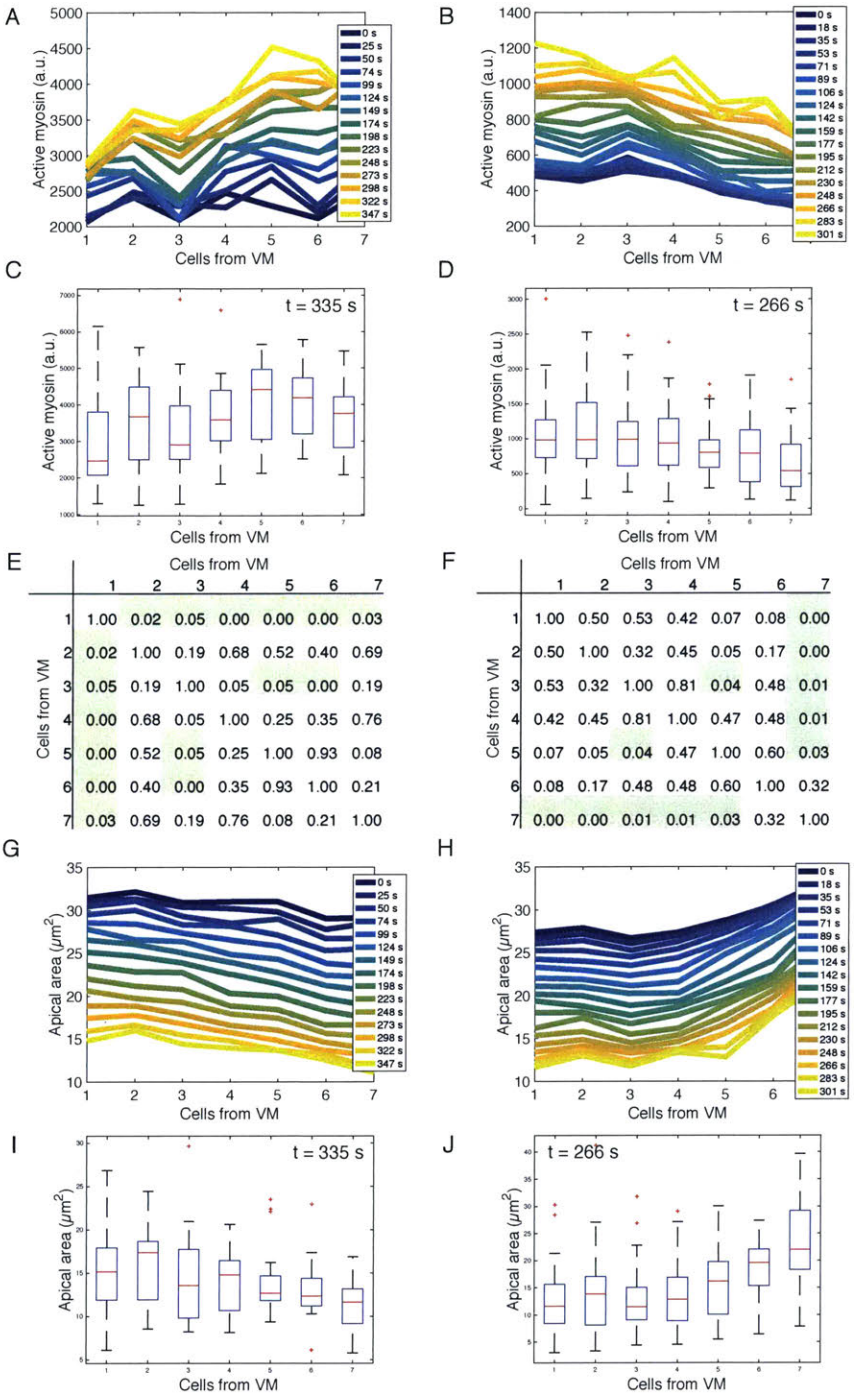

Figure 2.12: *Spn27A-RNAi* shows that the active myosin gradient is dependent on *dorsal* patterning in two additional *Spn27A--RNAi* embryos. (A–B) *Spn27A-RNAi* results in relatively uniform active myosin levels along ventral-lateral axis at all time points in two different embryos. Plot shows average active myosin intensity for each bin as a function of distance from VM. Different color lines are different time points. **(C–D)** The distribution of active myosin in two different embryos at t = 335 s and t = 266 s respectively. The distribution for each bin is depicted as a box and whisker plot. Red lines indicate median values, box indicates inner quartiles, while dotted lines indicate outer quartiles. **(E–F)** Active myosin neither embryo has a statistically significant gradient in average active myosin. Table of p-values from two-sample K-S test comparing cell bins for the data plotted in (C) and (D) respectively. Green indicates with $p < 0.05$. **(G–H)** *Spn27A-RNAi* results in uniform apical constriction along ventral-lateral axis in two separate embryos. Plot shows average apical area for each bin. Different color lines are different time points. (G) The distribution of apical area in two different embryos at t = 335 s and t = 266 s respectively. The distribution for each bin is depicted as a box and whisker plot. Red lines indicate median values, box indicates inner quartiles, while dotted lines indicate outer quartiles. (H). (A, C, E, G, and I) are measurements from a single embryo. Binning was performed the same for all measurements. n varies for each cell bin and time point. n = 12 cells/bin (minimum) and 22 cells/bin (average). (B, D, F, H, and J) are measurements from a single embryo. Binning was performed the same for all measurements. (n varies for each cell bin and time point. n = 21 cells/bin (minimum) and 62 cells/bin (average).

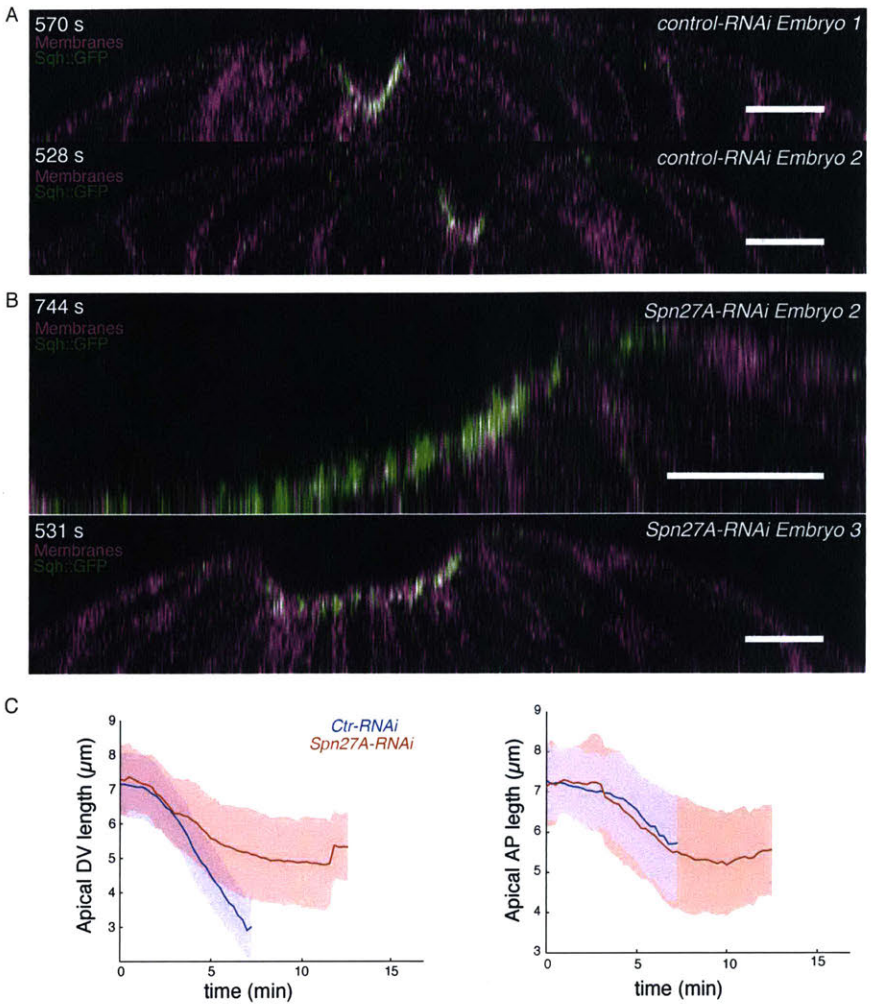

Figure 2.13: The shape of the furrow is flatter in *Spn27A-RNAi* embryos than in control embryos and the apical area decreases uniformly around the VM. (A) The cross-sectional shape of the furrow in control *Rh3-RNAi* is consistent with the WT furrow shape. Z-projection from an image stack from two control embryos. Embryo 1 is the same embryo as measured in Fig. 2.11 A, C, E, and G. Embryo 2 is the same embryo as measured in Fig. 2.11 B, D, F, and H. Timestamps are consistent. (B) The cross-section shape of the furrow in *Spn27A*-RNAi embryos is flatter and consistent with the model. Images are Z projections from an image stack from two *Spn27A*-RNAi embryos. Embryo 2 is the same embryo as measured in Fig. 2.12 A, C, E, and G. Embryo 3 is the same embryo as measured in Fig. 2.12 B, D, F, and H. (C) Quantification of apical cell length along each embryonic axis shows that control cells constrict more along the dorsal-lateral (DV) axis than *Spn27A-RNAi* embryos (left), but constrict a similar amount along the anterior-posterior (AP) axis (right). Cell length along each axis was determined by fitting an ellipsoid to shape of the cell and measuring the length along the AP and DV axes. *control-RNAi* (blue, n = 168 cells, 2 embryos), *Spn27A-RNAi* (red, n = 153 cells, 2 embryos), shaded areas indicate SD.

of uniform active myosin was broadened (Fig. 2.10A). Control knock-downs exhibited a gradient in active myosin similar to wild-type embryos (Fig. 2.11A-F). In contrast, *Spn27A* depleted embryos did not exhibit a normal gradient; instead they exhibited uniform active myosin within 6 cells of the VM (Fig. 2.11C-E and 2.12A-F). Furthermore, the uniform levels of active myosin were associated with uniform apical constriction compared to the normal apical area gradient seen in the control RNAi embryos (Fig. 2.10F-H and 2.12G-J compared with

2.11G-J). Because Spn27A attenuates Dorsal activity, our data suggests that the gradient in *twist*, active myosin, and apical constriction is the result of the gradient in Dorsal transcriptional activity.

In accordance with the prediction of our 3D continuum mechanical model, *Spn27A* depleted embryos exhibited reduced cross-sectional curvature in the region surrounding the VM, while the tissue does curve where there is a gradient of apical myosin activity at the edge of the broadened ventral domain (compare Fig. 2.7C to Fig. 2.14A and 2.13A to 2.13B). This failure to form a sharp furrow was associated with defective/reduced apical constriction, specifically along the ventral-lateral axis (Fig. 2.13C). This phenotype is consistent with the prediction of our model that increasing the width (w) of the region of contractility results in an expanded furrow, which is flattened at the VM where there is no myosin gradient.

2.2. Discussion

In many cases, epithelial folding is thought to result from myosin accumulating at the site of the fold (Lecuit et al., 2011; Leptin, 2005; Martin and Goldstein, 2014). Here, we show that active myosin accumulation fails to effectively change tissue curvature, except in regions where neighboring cells or tissue regions are accumulating different amounts of apical, active myosin. This conclusion is based on several pieces of evidence: 1) There is a gradient in mean levels of active myosin, which originates 2-3 cells from the VM and extends to 6 cells from the VM (Fig. 2.14B), 2) There are graded levels of both *twist* and its transcriptional target GFP::T48 that originate 3 cells from the VM and extend slightly farther than mean levels of active myosin (Fig. 2.14B), 3) mechanical modeling of a 3D elastic shell requires a contractility gradient to form a fold that resembles a ventral furrow, and 4) experimentally expanding and flattening the

myosin gradient in vivo results in an abnormal tissue shape that is predicted by the mechanical model. Thus, changes in tissue curvature and folding occur at sites of active myosin gradients. In the case of the *Drosophila* ventral furrow, the gradient in active myosin is the result of a gradient in the activity or levels of upstream transcription factors.

Gradients in the level of contractility, in our case apical contractile myosin, promote curvature by promoting a contractile force imbalance between neighboring regions of cells (Fig. 2.14C). In the case of the wild-type ventral furrow, this imbalance occurs along the ventral-lateral axis. Cells within 2-3 rows from the VM, accumulate similar levels of active myosin and constrict the same amount. Despite uniform active myosin in these central ~ 4 cells, it appears that these cells are able to pull the surrounding tissue and effectively constrict. Beyond 2-3 cells from the VM each cell exhibits progressively lower apical, active myosin, T48, and *twist* levels and constricts later and to a lesser extent (Fig. 2.14B,C).

Furrow formation requires asymmetric constriction (i.e., a wedge shape), such that cells' apical surface remains stretched along the anterior-posterior axis and constricted along the orthogonal (ventral-lateral) axis (Martin et al., 2010). When mechanically isolated, ventral furrow cells constrict symmetrically, suggesting that the elongated shape of the cell apical surface is the result of differences in forces generated by the surrounding tissue (Martin et al., 2010). We propose that the contractility gradient we measured in this paper allows cells to constrict more along the ventral-lateral axis because of less resistance from the surrounding tissue. This results in wedge-shaped cells and promotes curvature/folding specifically along the ventral-lateral axis (Fig. 2.14C).

In contrast to wild-type embryos, uniform contractility levels (i.e. in *Spn27A-RNAi*) increase the resistance to apical constriction from neighboring cells, thus, cells do not constrict

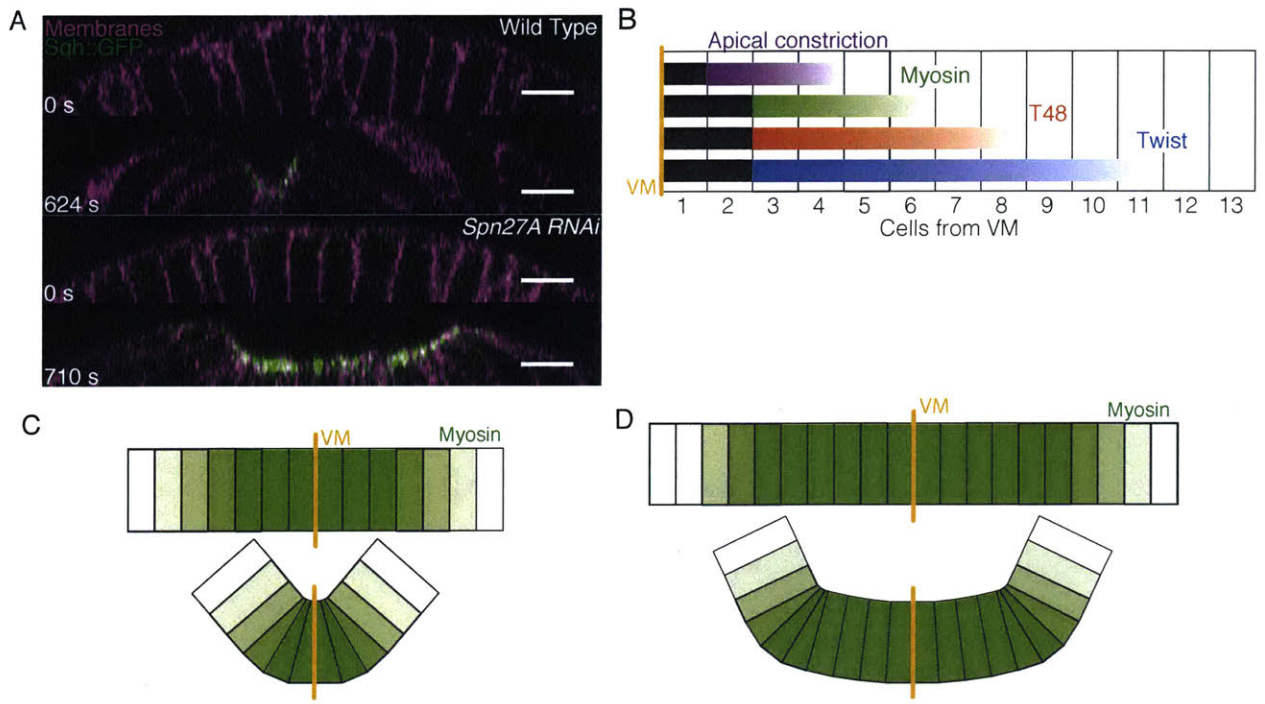

Figure 2.14: Model of ventral furrow formation. (A) Orthogonal projections in the z-plane of the ventral cross-section of wild-type (from Fig. 2.1) and *Spn27A*-RNAi (from Fig. 2.10) embryos. (B) Summary of gradients observed for twist mRNA (early nuclear cycle 14), T48::GFP, active myosin, and apical constriction in wild-type embryos. Uniform signal levels are in black, gradients are in color. (C) Gradient of myosin activation promotes cell wedging around the VM due to force imbalance, which folds the tissue. (D) Expansion of the ventral domain (i.e. *Spn27A*-RNAi) leads to an extended region of uniform myosin, in which forces are more balanced and bending is inhibited near the VM. Scale bars: 10 μm.

enough to generate high curvature (Fig. 2.14A,D). Consistent with this interpretation *Spn27A-RNAi* exhibited a defect in constriction along the ventral-lateral axis (Fig. 2.13C). *Spn27A-RNAi* embryos could occasionally fold and internalize the mesoderm, but these folds consistently exhibited a flattened depression and the invagination was often uneven and not temporally smooth.

2.2.1. A 3D elastic shell model supports importance of contractile gradients in tissue folding.

The in vivo experimental outcomes described above are consistent with our mechanical model. We found that having a contractile gradient around the circumference of an ellipsoid resulted in a sharp, narrow furrow. In contrast, increasing the width of the contractile zone

between opposing contractile gradients resulted in a flattening of the tissue at the VM, similar to in *Spn27A-RNAi*. In a systematic parameter scan of our model, the ventral furrow fails to develop if either contractility or the steepness of the gradient is too small. Thus, it is not simply absolute apical myosin activity that is required for shape, but active myosin differentials between neighboring regions or cells.

Our mechanical model differs from previous models of *Drosophila* gastrulation. It represents the first 3D continuum model of ventral furrow formation where apical constriction is the only active force input into the system (Conte et al., 2009; Conte et al., 2008; Odell et al., 1981; Polyakov et al., 2014; Spahn and Reuter, 2013). In particular, our theoretical analysis implies the role of active myosin gradients in tissue bending. Spahn and colleagues explored the role of a gradient in contractility on the pattern of cellular constriction, but their planar model did not reveal the importance of the gradient to folding (Spahn and Reuter, 2013). Conte and colleagues presented a 3D model of *Drosophila* gastrulation, but required introducing an ectodermal pushing to generate folding (Conte et al., 2008). Our results suggest that the embryo does not require ectodermal pushing if there is a contractility gradient.

We note that contractility conditions for successful furrow formation are intrinsic 3D effects not captured by 2D cross-section models. In particular, 2D models assume spatial invariance along the anterior-posterior axis and thus can be thought of as a model of furrow formation on an infinite cylinder. A cylinder has vanishing Gaussian curvature and axially invariant deformations introduce bending, but no stretching deformations. By contrast, furrow formation on an ellipsoid requires stretching of the membrane due to positive Gaussian curvature. The high energetic cost of stretching thus presents an effective energy barrier against such deformations, an important mechanical effect neglected in 2D. Therefore, 2D models may

significantly underestimate the conditions required for the furrow to form. The present 3D analysis underscores the mechanical importance of contractility gradients for the robust formation of the ventral furrow.

There are some limitations to our particular modeling approach. The most important is that the height of the elastic shell in our model is constant. This is not the case in vivo, where apical constriction initially results is cells lengthening along their apical-basal axis, followed by shortening along same axis (Sweeton et al., 1991). This final shortening step is associated with the generation of the highest curvature (Polyakov et al., 2014). Given that our model successfully predicts several experimental observations, thinking that a given magnitude of apical contractility generates a local preferred curvature of the surface of a shell provides a useful framework with which to understand tissue folding. The final tissue curvature will also be governed by the extent to which epithelial cells lengthen (which minimizes curvature) versus expanding their basal domain (which promotes curvature). A future experimental challenge will be to understand the cell biological and physical mechanisms that control epithelial cell height during this process. Regardless of specific mechanisms that control cell height the spatial pattern of contractility will play a central role in governing final tissue shape.

2.2.2. Evidence for the presence and function of a contractile gradient in the ventral furrow

Because of our ability to resolve cell shape and active myosin at cellular resolution, we have been able to show that there is a gradient in apical myosin that starts 3 cells from the VM and extends 6 cells distal to the VM. Thus, a 4-cell wide domain exhibits a contractility gradient, with differences in contractility existing between individual rows of cells with given ventral-lateral positions (Fig. 2.14B). The gradient we measured depends on a gradient in twist and

likely T48. It was the basis for our mechanical model of folding. Importantly, we show that flattening of this gradient leads to defects in tissue shape (i.e. reduced tissue curvature at the VM).

Other work also supports the importance of an active myosin gradient. Mutation of a possible attenuator of Fog signaling, *gprk2*, results in a broader activation of myosin (Fuse et al., 2013). Interestingly, the *gprk2* mutant phenotype delayed folding at the VM and instead only displayed changes in curvature at the edges of the myosin domain (Fuse et al., 2013). The *gprk2* mutant phenotype resembles that of *Spn27A-RNAi*. Thus, multiple mutant phenotypes are consistent with the requirement of an active myosin gradient to promote tissue curvature, which reinforces our conclusions.

2.2.3. Implications of the gradient model to neural tube closure

Our finding, that it is not myosin activity per se, but active myosin differentials that lead to folding, is likely relevant to neural tube closure in vertebrates. Interestingly, the neural tube folds mainly at 3 hinge points that are separate from one another in the neuroepithelium (Copp and Greene, 2010). The width of the domain of apically constricting cells in a hinge point in the mouse neuroepithelium has been shown to be about 3 or 4 cells (Smith et al., 1994). Because folding occurs in regions where there is differential myosin activity, hinge points might promote this differential and enable more efficient tissue folding, as opposed to activating myosin in the entire neuroepithelium.

2.3. Materials and Methods

2.3.1. Fly stocks and genetics

Fly lines and crosses are listed in Table 2.1. Embryos were collected from cages at 25° C except where noted.

Table 2.1

Stock	Genotype	Source/Reference	Figure (# of embryos)
1	SqhGFP Royou		
2	w; Gap43::mCherry(attp40); Sqh::GFP	Martin et al., 2010	
3	OreR	Bloomington *Drosophila* Stock Center	3 (1)
4	y[1] sc[*] v[1]; P{y[+t7.7] v[+t1.8]=TRiP.HMC03159} attP2 (Spn27A shRNA line)	TRiP center*	
5	y[1] sc[*] v[1]; P{y[+t7.7] v[+t1.8]=TRiP.GL01052}attP2 (Rh3 shRNA control line)	TRiP center*	
6	y,w; Sqh::GFP; mat15, Gap43::mCherry/(TM3, Sb[1])	Vasquez et al., 2014	
7	y,w;+; vk33{BAC GFP::T48}	Heer et al. 2017	2 (1); S3 (1)
F2 embryos imaged from these crosses, using above stock numbers/genotypes. Non-balancer females were used for cages.			
	Stock # 1 x 2 (Virgins x males)		1 B–H (1); S1(2); S2 (2)
	4 x 6 (23 and 18 °C)		6 B–F (1); S3(1); S6 (2)
	5 x 6 (23 C)		S5 (2)
	*Norbert Perrimon, Harvard Medical School and Howard Hughes Medical Institute, Boston, MA		

2.3.2. Cloning

GFP was inserted in the T48 coding sequence at amino acid residue 85, with a standard linker (amino acids GGSG) added before and after the GFP. The T48::GFP construct was inserted in the BAC (CH321-58L17,) using standard recombineering techniques (Venken et al., 2006; Warming et al., 2005). We injected the nanos-integrase; attp40; vk33 embryos with the purified BAC and selected for transgenic flies using white+ marker. Primers for T48 transgenic as follows:

5' upstream homology arm: 5'-ATGCGGTCGGTGGAAGTGGC-3'; 3' upstream homology arm: 5'-GCTCACGCCCGAGCCGCCCATGCCGGGCAGCACCAC-3'; 5' GFP with linker: 5'-GGCGGCTCGGGCGTGAGCAAGGGCGAGGAGCTGTTCACCGG-3'; 3' GFP with linker: 5'-GCCCGAGCCGCCCTTGTACAGCTCGTCCATGCCGAGAGTG-3'; 5' downstream homology arm: 5'-GTACAAGGGCGGCTCGGGCCTGCAAAATTCAGGTGGG-3'; 3' downstream homology arm: 5'-CACACGCTTTATTTGGGGCTC-3'.

2.3.3. Live and Fixed imaging

For live imaging, embryos were dechorionated with 50% bleach, rinsed with water and mounted with ventral side facing up on glass slides covered with embryo glue (Scotch tape glue in Heptane). A chamber was created using spacers made from 1.5 cover slips, and imaged through a No. 1 cover slip after being covered in Halocarbon oil 27. Images were acquired on a Zeiss 710 microscope with an Apochromat 40x/1.2 numerical aperture W Korr M27 objective. Pinhole size: 2.2 or 2.4 airy units. A 488/561 beam splitter was used. Channels were excited

(Argon 488 LASER, 2.6% or 4.5%, DPSS 561-10, 2% or 2.8%) and acquired (Detected range: 493-561 nm and 599-696 nm) concurrently.

For immunostaining, embryos were first dechorionated in 50% bleach and fixed in 8% PFA using standard protocols. The vitelline membranes of the embryos were mechanically removed using a syringe and the embryos were then stained using standard protocols with a GFP antibody(Rabbit, 1:500, ABCAM (ab290)) and AlexaFluor 647 phalloidin (Invitrogen). Embryos were mounted in Aqua Poly/Mount (Polyscience, Inc). All imaging was done on a Zeiss 710 confocal microscope with a Plan-Apochromat 63x/1.4 numerical aperture Oil DIC M27 objective. Pinhole size: 1 airy unit. Channel 1: DPSS 651-10 LASER (1%), detector range: 574-712 nm. Channel 2: Argon 488 LASER (2%) detector range: 493-574 nm.

For quantitative FISH, embryos were fixed (8% PFA, 45 mins) and stained as described in (Little et al., 2011). Probes complementary to the twist ORF were conjugated to AlexaFluor594 (Life Technologies). DAPI was used to detect nuclei. Embryos were mounted in Aqua Poly/Mount (Polyscience, Inc). All imaging was done on a Zeiss 710 confocal microscope with a Plan-Apochromat 63x/1.4 numerical aperture Oil DIC M27 objective. Channels were acquired on separate tracks. Pinhole size: 1 airy unit. Track1: Diode 405-30 (.5%) Detector range: 410-582 nm. Track 2 HeNe594 (15%) detector range 602-734 nm. Each line was scanned 4 times and the sum recorded.

2.3.4. Image processing

All image analysis was done in FIJI (http://fiji.sc) (Schindelin et al., 2012) and MATLAB (MathWorks). Custom software for image processing is available upon request to the corresponding author.

Analysis of active myosin: First cytoplasmic background signal (defined as the mean cytoplasmic signal plus 2.5 std.) was subtracted from the myosin channel (Martin et al., 2009; Vasquez et al., 2014). This subtraction removed the contribution of cytoplasmic myosin to the integrated signal and left only the concentrated apical signal that evidence suggests is active myosin. The max myosin signal intensity in z was used to generate a rough map of the embryo surface. A Fourier transform was used to generate a smooth continuous surface. Myosin signal was averaged over the 4 μm above the surface and membrane signal was the sum of the signal from 1-2μm below the surface. (Membrane signal was only used for segmentation, not quantification).

Immunostained images: T48 signal was quantified in a single apical slice from a 3D image. Fixed embryos are flattened during mounting, surface projections used in live embryos were not necessary. The T48 signal was not background subtracted.

All live and immunostained images were then segmented using an existing MATLAB package Embryo Development Geometry Explorer (EDGE) (Gelbart et al., 2012). Membrane signal (gap43mCherry) or cortical actin (phalloidin) were used to detect cell boundaries and track cells in time for live images. Errors in segmentation were corrected manually to ensure proper segmentation. Our segmentation algorithm was used to determine centroid position, cell diameter, cell area and total myosin or T48 signal intensity within a cell.

Quantification of the twist mRNA in OR and Spn27A-RNAi embryos: FISH signal was performed using a previously published software package, which partitions the cytoplasm into "cells" based on nuclear position and subtracts the nuclear volume from measurements of average cytoplasmic signal per "cell" (McHale et al., 2011). This package was used to determine cell centroid position for each cell, average cytoplasmic signal per pixel for each cell, and average cell

diameter for the image.

2.3.5. Image Analysis

In all image quantifications, data was aggregated into "cell bins". Cells were assigned to bins based on the position of the cell centroid along the ventral-lateral axis. We first identified the approximate position of the VM in all images. In live images, the VM was defined as the position at which the furrow closes over (Fig. 2.1, 2.10, 2.2, 2.11 and 2.12). In fixed images, the signal was first confirmed to be symmetric, and the position of the VM was determined by the symmetry of the signal (Fig. 2.4, 2.5, 2.6, and 2.9). We were unable to determine the precise VM position in Spn27A-RNAi embryos stained for in twist mRNA because the boundaries of the domain expressing twist mRNA extended beyond the field of view. In this case (Fig. 2.5) we did not assume symmetry of the signal, and simply determined the distribution twist mRNA in a ventral region. When assigning cells to bins based on centroid position, live images were binned based on initial position of the cell centroid before tissue contraction and folding and the boundaries of the bins were set by the average cell diameter along the ventral-lateral axis (Fig. 2.1, 2.2, 2.11, 2.10, and 2.12). For example, cell bin 1 includes all cells with a cell centroid that fell within 1 average cell diameter of the VM. For fixed images where cells had already begun to constrict, the width of each bin was set manually to approximate the width of cells at that ventral-lateral position (Fig. 2.4 and 2.5). For fixed images were cells had yet to constrict, the boundaries of each bin were determined by an average cell diameter estimate (Fig. 2.6 and 2.9).

For a representative time point from each image, box and whisker plots depicted the distribution of values in each cell bin were generated using MATLAB. Additionally, for all box and whisker plots, a two sample Kolmogorov–Smirnov test was used to test whether the

distribution of signal at each bin was significantly different from the distribution of signal at every other bin. For live images, we also determined the mean value of each bin for all time points.

In some time series, image acquisition began slightly after myosin accumulation in which case t =0 s, is the first acquired image in the time series. In other time series, the image acquisition began much before furrow formation in which case we truncated the time series so that the initial time point is ~1 min before cells begin to constrict.

Apical cell length measurement: Cell length along the ventral-lateral and anterior-posterior axes is an output of EDGE. Embryos were aligned in time base on the average onset of apical constriction. Measurements were made only for cells within ~2 cell diameters of the ventral midline.

2.3.6. Statistical analysis

Testing for statistical significance was done using the MATLAB statistical toolbox. We used the non-parametric two sample Kolmogorov-Smirnov to test for significance for all reported p-values.

2.3.7. Theoretical Model

At the gastrulation state, the epithelial sheet consists of ~6,000 cells and its shape closely resembles that of an ellipsoid with major axis $a \sim 250$ μm and minor axes $b = c \sim 125$ μm (Fig. 2.7A). As both the length and diameter of the embryo are much larger than the average cell diameter ~7– 8 μm and thickness $h \sim 35$ μm, the mechanics of the epithelial cell sheet can approximately be described by the Koiter shell model (Ciarlet, 2000). This continuum theory accounts for mechanical strain and stresses in terms of the deviation of the shell's middle-surface

ω from a reference shape $\bar{\omega}$. Explicitly, the elastic energy $\mathcal{E}$ of the shell is given by

$$\mathcal{E} = \frac{Yh}{8(1-\nu^2)} \int_{\bar{\omega}} S \Big\{ (1-\nu)\mathrm{Tr}[(\mathbf{a}-\bar{\mathbf{a}})^2] + \nu \mathrm{Tr}(\mathbf{a}-\bar{\mathbf{a}})^2 + \frac{h^2}{3}\left[(1-\nu)\,\mathrm{Tr}\left[(\mathbf{b}-\bar{\mathbf{b}})^2\right] + \nu \mathrm{Tr}(\mathbf{b}-\bar{\mathbf{b}})^2\right] \Big\} d\bar{\omega}$$

Here, Y is the Young's modulus, ν the Poisson Ratio (we set $\nu = \frac{1}{2}$ corresponding to an incompressible material), and the integral extends over the surface $\bar{\omega}$. The parameter S accounts for the spatially dependent stiffness variations and is typically set to $S = 1$ for passive equilibrium materials. However, when including apical constriction stresses, S becomes myosin dependent, as outlined below. The first term in the integral corresponds to a stretching energy, while the second term captures the energetic cost of bending the surface. Tr denotes a generalized trace, similar to the usual matrix trace (see SM for details). $\mathbf{a}$ and $\bar{\mathbf{a}}$ are the 2 x 2 metric tensors of the deformed surface ω and reference surface $\bar{\omega}$. They describe the local geometry of the surface by measuring the lengths of and angles between tangent vectors $\mathbf{a}_i$ at any point of the surface (Fig. 2.7A). Specifically, the components of $\mathbf{a}$ are given by $a_{ij} = \mathbf{a}_i \cdot \mathbf{a}_j$ with $\cdot$ the usual (vector) dot product. The first term in Eq. (1) thus measures the deviations of lengths and angles between the reference and deformed configurations, thereby capturing the energetic cost of stretching and shearing the surface. Similarly, the curvature tensors $\mathbf{b}$ and $\bar{\mathbf{b}}$ measure the local curvature of the deformed and the reference surface (denoted), respectively; see SM for their precise definitions. Thus, the integrand in the second line assigns an energetic cost whenever there is a mismatch between the local and preferred curvatures $\mathbf{b}$ and $\bar{\mathbf{b}}$, respectively.

The Koiter shell energy in Eq. (1) describes the mechanics of a passive shell. To include the internal stresses due to active myosin, we consider a patch of neighboring rectangular 'model'

cells (Fig. 1B). The inner and outer faces represent the apical and basal surfaces of the epithelial cells, respectively. We assume that the most relevant forces are due to compression/stretching of the upper and lower cell faces. If the cell patch is initially in a stress-free flat state, active myosin stresses are introduced by adding an additional surface tension term to the apical face of the cells. The energy E of each cell then reads

$$E(A^+, A^-) = C_M \rho_M A^{+2} + K(A^+ - A^0)^2 + K(A^- - A^0)^2$$

where A^+ and A^- denote the areas of the outer (contracting) and inner cell faces, A^0 is the stress-free reference area of each face, and K their stiffness in the absence of myosin. ρ_M is the myosin concentration and C_M a proportionality constant. We note that the dimensionless ratio $M = \frac{C_M \rho_M}{K}$ alone determines the myosin-induced shape deformation. M can thus be understood as a dimensionless contractility coefficient that is proportional to the local myosin concentration. Assuming a constant cell volume and constant thickness h, we can determine the equilibrium shape of the patch for given value of M in terms of the equilibrium areas $\bar{A}^+$ and $\bar{A}^-$ that minimize Eq. (2). Reducing the geometry to its middle surface, we find that the initially flat patch effectively obtains a new, myosin-induced target curvature κ given by

$$\kappa \approx \frac{\theta}{s}$$

with $\theta = \pi - 2 \arctan\left[\frac{2\epsilon}{\sqrt{\bar{A}^-} - \sqrt{\bar{A}^+}}\right]$ the angle between the middle-surface normal of neighboring cells and $s = \frac{(\sqrt{\bar{A}^-} + \sqrt{\bar{A}^+})}{2}$ the distance between cell centers on the middle-surface (Fig. 1B). The exact dependence of κ on M is given in the SM. Taking the continuum limit (SM), we obtain the myosin-induced target curvature tensor $\bar{\mathbf{b}} = \kappa\, \bar{\boldsymbol{a}}$

and the material stiffening parameter $S = 1 + M$. The mismatch of local shell curvature

$\mathbf{b}$ and myosin-induced spontaneous curvature $\bar{\mathbf{b}}$ drives furrow formation in our model. In our simulations, we add to Eq. (1) two additional energy terms representing the incompressibility of the embryo yolk and the stiffness of the vitelline membrane. The resulting continuum model was simulated using the algorithm previously described (Vetter et al., 2013).

2.3.8. Acknowledgements

We would like to thank N. Perrimon, L. Perkins, and the Transgenic RNAi Project at Harvard Medical School (National Institutes of Health/National Institutes of General Medical Sciences R01-GM084947) for providing transgenic RNAi stocks used in this study. We would also like to thank A. McHale for the software package used to analyze of FISH images. We would like to thank S. Little for his protocol to stain embryos with smFISH probes and C. Engbert for help implementing the protocol. The authors thank R. Horvitz, R. Gupta, and current and former members of the Martin Lab for helpful discussion and feedback on the project.

2.4. References

Barrett, K., Leptin, M., Settleman, J., 1997. The Rho GTPase and a putative RhoGEF mediate a signaling pathway for the cell shape changes in *Drosophila* gastrulation. Cell 91, 905-915.

Ciarlet, P.G., 2000. Mathematical Elasticity. North Holland.

Conte, V., Munoz, J.J., Baum, B., Miodownik, M., 2009. Robust mechanisms of ventral furrow invagination require the combination of cellular shape changes. Phys Biol 6, 016010.

Conte, V., Munoz, J.J., Miodownik, M., 2008. A 3D finite element model of ventral furrow invagination in the *Drosophila* melanogaster embryo. J Mech Behav Biomed Mater 1, 188-198.

Copp, A.J., Greene, N.D., 2010. Genetics and development of neural tube defects. J Pathol 220, 217-230.

Coravos, J.S., Martin, A.C., 2016. Apical Sarcomere-like Actomyosin Contracts Nonmuscle *Drosophila* Epithelial Cells. Dev Cell 39, 346-358.

Costa, M., Wilson, E.T., Wieschaus, E., 1994. A putative cell signal encoded by the folded gastrulation gene coordinates cell shape changes during *Drosophila* gastrulation. Cell 76, 1075-1089.

Dawes-Hoang, R.E., Parmar, K.M., Christiansen, A.E., Phelps, C.B., Brand, A.H., Wieschaus, E.F., 2005. folded gastrulation, cell shape change and the control of myosin localization. Development 132, 4165-4178.

Fuse, N., Yu, F., Hirose, S., 2013. Gprk2 adjusts Fog signaling to organize cell movements in *Drosophila* gastrulation. Development 140, 4246-4255.

Gelbart, M.A., He, B., Martin, A.C., Thiberge, S.Y., Wieschaus, E.F., Kaschube, M., 2012. Volume conservation principle involved in cell lengthening and nucleus movement during tissue morphogenesis. Proc Natl Acad Sci U S A 109, 19298-19303.

Hacker, U., Perrimon, N., 1998. DRhoGEF2 encodes a member of the Dbl family of oncogenes and controls cell shape changes during gastrulation in *Drosophila*. Genes Dev 12, 274-284.

Ip, Y.T., Park, R.E., Kosman, D., Yazdanbakhsh, K., Levine, M., 1992. dorsal-twist interactions establish snail expression in the presumptive mesoderm of the *Drosophila* embryo. Genes Dev 6, 1518-1530.

Jodoin, J.N., Coravos, J.S., Chanet, S., Vasquez, C.G., Tworoger, M., Kingston, E.R., Perkins, L.A., Perrimon, N., Martin, A.C., 2015. Stable Force Balance between Epithelial Cells Arises from F-Actin Turnover. Dev Cell 35, 685-697.

Jodoin, J.N., Martin, A.C., 2016. Abl suppresses cell extrusion and intercalation during epithelium folding. Mol Biol Cell 27, 2822-2832.

Kanodia, J.S., Rikhy, R., Kim, Y., Lund, V.K., DeLotto, R., Lippincott-Schwartz, J., Shvartsman, S.Y., 2009. Dynamics of the Dorsal morphogen gradient. Proc Natl Acad Sci U S A 106, 21707-21712.

Kerridge, S., Munjal, A., Philippe, J.M., Jha, A., de las Bayonas, A.G., Saurin, A.J., Lecuit, T., 2016. Modular activation of Rho1 by GPCR signaling imparts polarized myosin II activation during morphogenesis. Nat Cell Biol 18, 261-270.

Kolsch, V., Seher, T., Fernandez-Ballester, G.J., Serrano, L., Leptin, M., 2007. Control of *Drosophila* gastrulation by apical localization of adherens junctions and RhoGEF2. Science 315, 384-386.

Lecuit, T., Lenne, P.F., Munro, E., 2011. Force generation, transmission, and integration during cell and

tissue morphogenesis. Annu Rev Cell Dev Biol 27, 157-184.

Leptin, M., 1991. twist and snail as positive and negative regulators during *Drosophila* mesoderm development. Genes Dev 5, 1568-1576.

Leptin, M., 2005. Gastrulation movements: the logic and the nuts and bolts. Dev Cell 8, 305-320.

Leptin, M., Grunewald, B., 1990. Cell shape changes during gastrulation in *Drosophila*. Development 110, 73-84.

Ligoxygakis, P., Roth, S., Reichhart, J.M., 2003. A serpin regulates dorsal-ventral axis formation in the *Drosophila* embryo. Curr Biol 13, 2097-2102.

Lim, B., Levine, M., Yamakazi, Y., 2017. Transcriptional Pre-patterning of *Drosophila* Gastrulation. Curr Biol 27, 286-290.

Little, S.C., Tkacik, G., Kneeland, T.B., Wieschaus, E.F., Gregor, T., 2011. The formation of the Bicoid morphogen gradient requires protein movement from anteriorly localized mRNA. PLoS Biol 9, e1000596.

Manning, A.J., Peters, K.A., Peifer, M., Rogers, S.L., 2013. Regulation of epithelial morphogenesis by the G protein-coupled receptor mist and its ligand fog. Sci Signal 6, ra98.

Martin, A.C., Gelbart, M., Fernandez-Gonzalez, R., Kaschube, M., Wieschaus, E.F., 2010. Integration of contractile forces during tissue invagination. J Cell Biol 188, 735-749.

Martin, A.C., Goldstein, B., 2014. Apical constriction: themes and variations on a cellular mechanism driving morphogenesis. Development 141, 1987-1998.

Martin, A.C., Kaschube, M., Wieschaus, E.F., 2009. Pulsed contractions of an actin-myosin network drive apical constriction. Nature 457, 495-499.

Mason, F.M., Xie, S., Vasquez, C.G., Tworoger, M., Martin, A.C., 2016. RhoA GTPase inhibition organizes contraction during epithelial morphogenesis. J Cell Biol 214, 603-617.

McHale, P., Mizutani, C.M., Kosman, D., MacKay, D.L., Belu, M., Hermann, A., McGinnis, W., Bier, E., Hwa, T., 2011. Gene length may contribute to graded transcriptional responses in the *Drosophila* embryo. Dev Biol 360, 230-240.

Oda, H., Tsukita, S., Takeichi, M., 1998. Dynamic behavior of the cadherin-based cell-cell adhesion system during *Drosophila* gastrulation. Dev Biol 203, 435-450.

Odell, G.M., Oster, G., Alberch, P., Burnside, B., 1981. The mechanical basis of morphogenesis. I. Epithelial folding and invagination. Dev Biol 85, 446-462.

Parks, S., Wieschaus, E., 1991. The *Drosophila* gastrulation gene concertina encodes a G alpha-like protein. Cell 64, 447-458.

Polyakov, O., He, B., Swan, M., Shaevitz, J.W., Kaschube, M., Wieschaus, E., 2014. Passive mechanical forces control cell-shape change during *Drosophila* ventral furrow formation. Biophys J 107, 998-1010.

Reeves, G.T., Trisnadi, N., Truong, T.V., Nahmad, M., Katz, S., Stathopoulos, A., 2012. Dorsal-ventral gene expression in the *Drosophila* embryo reflects the dynamics and precision of the dorsal nuclear gradient. Dev Cell 22, 544-557.

Royou, A., Sullivan, W., Karess, R., 2002. Cortical recruitment of nonmuscle myosin II in early syncytial *Drosophila* embryos: its role in nuclear axial expansion and its regulation by Cdc2 activity. J Cell Biol 158, 127-137.

Schindelin, J., Arganda-Carreras, I., Frise, E., Kaynig, V., Longair, M., Pietzsch, T., Preibisch, S., Rueden, C., Saalfeld, S., Schmid, B., Tinevez, J.Y., White, D.J., Hartenstein, V., Eliceiri, K., Tomancak, P., Cardona, A., 2012. Fiji: an open-source platform for biological-image analysis. Nat Methods 9, 676-682.

Smith, J.L., Schoenwolf, G.C., Quan, J., 1994. Quantitative analyses of neuroepithelial cell shapes during bending of the mouse neural plate. J Comp Neurol 342, 144-151.

Spahn, P., Reuter, R., 2013. A vertex model of *Drosophila* ventral furrow formation. PLoS One 8, e75051.

Sweeton, D., Parks, S., Costa, M., Wieschaus, E., 1991. Gastrulation in *Drosophila*: the formation of the ventral furrow and posterior midgut invaginations. Development 112, 775-789.

Thisse, B., Stoetzel, C., El Messal, M., Perrin-Schmitt, F., 1987. Genes of the *Drosophila* maternal dorsal group control the specific expression of the zygotic gene twist in presumptive mesodermal cells. Genes & Development 1, 709-715.

Timoshenko, S., 1925. Analysis of bi-metal thermostats. J Opt Soc Am Rev Sci 11, 233-255.

Vasquez, C.G., Heissler, S.M., Billington, N., Sellers, J.R., Martin, A.C., 2016. *Drosophila* non-muscle myosin II motor activity determines the rate of tissue folding. Elife 5.

Vasquez, C.G., Tworoger, M., Martin, A.C., 2014. Dynamic myosin phosphorylation regulates contractile pulses and tissue integrity during epithelial morphogenesis. J Cell Biol 206, 435-450.

Venken, K.J., He, Y., Hoskins, R.A., Bellen, H.J., 2006. P[acman]: a BAC transgenic platform for targeted insertion of large DNA fragments in D. melanogaster. Science 314, 1747-1751.

Vetter, R., Stoop, N., Jenni, T., Wittel, F.K., Herrmann, H.J., 2013. Subdivision shell elements with anisotropic growth. Int J Numer Meth Eng 95, 791-810.

Wallingford, J.B., Niswander, L.A., Shaw, G.M., Finnell, R.H., 2013. The continuing challenge of understanding, preventing, and treating neural tube defects. Science 339, 1222002.

Warming, S., Costantino, N., Court, D.L., Jenkins, N.A., Copeland, N.G., 2005. Simple and highly efficient BAC recombineering using galK selection. Nucleic Acids Res 33, e36.

Xie, S., Martin, A.C., 2015. Intracellular signaling and intercellular coupling coordinate heterogeneous contractile events to facilitate tissue folding. Nat Commun 6, 7161.

Xie, S., Mason, F.M., Martin, A.C., 2016. Loss of Galpha12/13 exacerbates apical area-dependence of actomyosin contractility. Mol Biol Cell.

Chapter 3. Inhibitors downstream of Twist restrict the multicellular gradient of myosin activation

Natalie C. Heer

Classically, morphogen gradients function to convey tissue-scale positional information to individual cells within that tissue. In the case of the *Drosophila* ventral furrow, the morphogen gradient that determines cell position along the dorsal-ventral axis also patterns the activation of actomyosin contractility in the embryo. There are many signaling steps between the gradient in the morphogen Dorsal and the gradient in actomyosin contractility, some of which are still unknown. The signal activators measured in the previous chapter were all activated or present in a gradient similar to the Dorsal gradient, but more upstream components consistently had broader gradients than more downstream components. In the previous chapter, we found that the downstream gradients depended on the upstream gradients, but it is still unclear what determines the shape and extent of the myosin gradient given the distribution of Twist. (Fig. 3.1).

Generally speaking, cell fate outputs are determined by the concentration of morphogen inputs. Recent work, however, has suggested that it is not simply the concentration at any given time that determines cell fates, but instead may be a result of more complicated processes, such as temporal integration of the signal or a cell-level calculation of the spatial and temporal

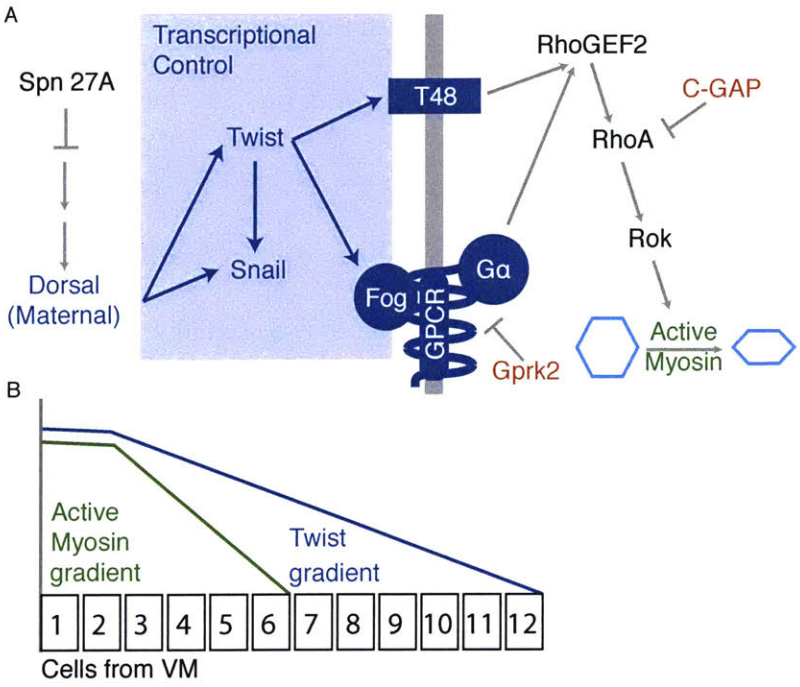

Figure 3.1: (A) Schematic of the signaling pathway leading to myosin activation from the ventral-lateral patterning genes. Transcription factors are lettered in blue, and the interactions at the apical surface of cells expressing *fog* and *T48* are diagramed along the gray line, which represents the apical membrane. Inhibitors of the signaling pathway explored in this chapter are colored in red. (B) Diagram comparing the distribution of active myosin around the ventral midline with the distribution of *twist* mRNA around the ventral midline. Cells and relative levels of active myosin and *twist* mRNA are depicted.

derivatives of the signal (Richards and Saunders, 2015). To begin to understand the relationship between morphogen input and constriction output in the ventral domain, I will test whether signaling inhibitors play a role in restricting the morphogen and Twist gradient to the gradient in apical constriction. The two signaling pathway inhibitors that I test in this chapter are C-GAP, an inhibitor of RhoA, and Gprk2, an inhibitor of GPCR signaling that functions upstream of RhoA (Fuse et al., 2013; Mason et al., 2016).

In the *Drosophila* embryo, the Dorsal morphogen has classically been thought to determine domains, including the ventral domain, through concentration thresholding; that is all cells with a Dorsal concentration above a certain threshold would be in the ventral domain. Recent work, however, has suggested a more complicated relationship. The Dorsal gradient increases in amplitude and sharpness with time (Reeves et al., 2012). The width of the domains of expression of *snail*, *t48*, and *fog* genes downstream of Dorsal activity also expand over time

(Lim et al., 2017; Reeves et al., 2012). For *t48* and *fog*, the increasing width of the expression domain causes the transcripts to accumulate in a gradient (Lim et al., 2017). The mechanism is a possible source for the signaling gradients measured in Chapter 2. An important aspect of the gradients that I measured is that the more upstream components have broader distributions, raising the question of what causes the narrowing of the gradient across the signaling pathway.

Twist, the most upstream component measured in Chapter 2, is one of two key embryonic transcription factors downstream of Dorsal in the ventral domain (Leptin and Grunewald, 1990). Twist is required to spatially pattern the ventral furrow and to activate apical constriction in the furrow domain (Heer et al., 2017; Leptin and Grunewald, 1990). Twist activates the transcription of two target genes, *fog* and *T48*. RhoGEF2 is activated in parallel by T48 and a GPCR/G protein pathway activated by Fog (Costa et al., 1994; Hacker and Perrimon, 1998; Kanesaki et al., 2013; Kolsch et al., 2007; Rogers et al., 2004). RhoGEF2, in turn, activates RhoA, a small GTPase that is a key component of the signaling pathway. RhoA promotes and organizes myosin activity and actin polarity within individual cells, leading to apical constriction (Coravos and Martin, 2016; Mason et al., 2013).

The inhibitor of RhoA, C-GAP, plays a crucial role in regulating the dynamics of actomyosin contractility in the ventral furrow. Embryos depleted of C-GAP, or genetic mutants for the C-GAP gene, display a range of phenotypes, including disruption of embryo development prior to ventral furrow formation, inhibition of furrow formation, and delay of furrow formation (Mason et al., 2016). C-GAP levels, along with RhoGEF2 levels, set the rate of myosin oscillations (pulsing) in the embryo. During furrow formation, apical myosin levels both oscillate and increase with time on the cell level. Overexpression of C-GAP causes the myosin dynamics to be more oscillatory, whereas depleting C-GAP eliminates oscillations and

causes the linear increase of activate myosin to dominate. Both extremes can prevent successful apical constriction. C-GAP is maternally loaded and uniformly expressed in the embryo, though it is not yet known how C-GAP is regulated (Mason et al., 2016).

GPCR kinases phosphorylate ligand-bound GPCRs and attenuate their signaling (Moore, 2007). Gprk2, the *Drosophila* GPCR kinase, is required for proper cell dynamics in the ventral furrow (Fuse et al., 2013). Prior to this work, the impact of Gprk2 inhibition of the dynamics of myosin accumulation had not been studied, but Gprk2 mutant embryos display different dynamics, in which more lateral cells in the ventral domain move toward the ventral furrow. In wild type embryos, these more lateral cells experience an acceleration in their movement towards the ventral midline (VM), which is inhibited in Gprk2 mutant embryos (Fuse et al., 2013). This effect depends on Fog activity, suggesting that Gprk2 operates downstream of Twist and Fog (Fuse et al., 2013).

Recent work has demonstrated the importance of negative regulators in promoting dynamic constriction and maintaining tissue integrity in the ventral furrow (Jodoin et al., 2015; Mason et al., 2016). Here, I directly test whether these inhibitors also shape the spatial distribution of apical myosin across the tissue. My hypothesis, based on the previous chapter, is that the negative regulators might play a role in narrowing the broader gradient seen in more upstream signaling components. This is the first step in generating a model of how a gradient in Twist is translated into a gradient in active myosin.

3.1. Results

3.1.1. The inhibitor of RhoA activity, C-GAP restricts the width of the gradient in active myosin in the ventral furrow.

To test whether C-GAP restricts the gradient of the more upstream components, I

measured the distribution of active myosin[2] in embryos depleted of C-GAP using a GFP-tagged version of the myosin regulatory light chain (sqh::GFP). To disrupt C-GAP, shRNA targeting the C-GAP transcript was loaded into the embryo using the UAS-GAL4 system. Embryos were collected under conditions designed to generate a mild phenotype because severe phenotypes disrupt the process of cellularization and thus the integrity of the epithelium (see Methods for description) (Mason et al., 2016). I analyzed the shape of the myosin gradient in two embryos moderately depleted of C-GAP RNA. Cells were binned by their position relative to the VM, with cells on both sides of the VM combined into the same bins (Fig. 3.2A,B).

First, I analyzed the averaged active myosin levels for each cell bin over time (Fig. 3.2C,D and 3.S1A,B). As the C-GAP-depleted embryo furrows, active myosin levels increase at the midline and in cell bins 1–7, in contrast with the control embryo, in which active myosin levels increase in cell bins 1–5 (Fig. 3.2C,D and 3.3A,B). Next, I analyzed the distribution of active myosin values per cell in each cell bin at a specific time point between 350s and 450s after the onset of apical constriction (Fig. 3.2E,F and 3.3C,D). From these graphs, it is clear that there is greater variation in active myosin cells in cell bins with higher levels of active myosin. This is consistent with previous analyses of active myosin distributions in Chapter 2. Consistent with our measurements of average cell bin values over time, the gradient in active myosin is broader in C-GAP-depleted embryos than in the control embryo (Fig. 3.2E,F and 3.3C,D). The domains of uniform active myosin around the VM, defined by the cell bins, do not exhibit a statistical difference in the distribution of total active myosin levels per cell (K-S test, $p < 0.05$; see Methods for details). Cells within 4-5 cells of the VM have uniform myosin levels in the C-

[2] Active myosin, as it is used here, is defined in Section 2.2.1.

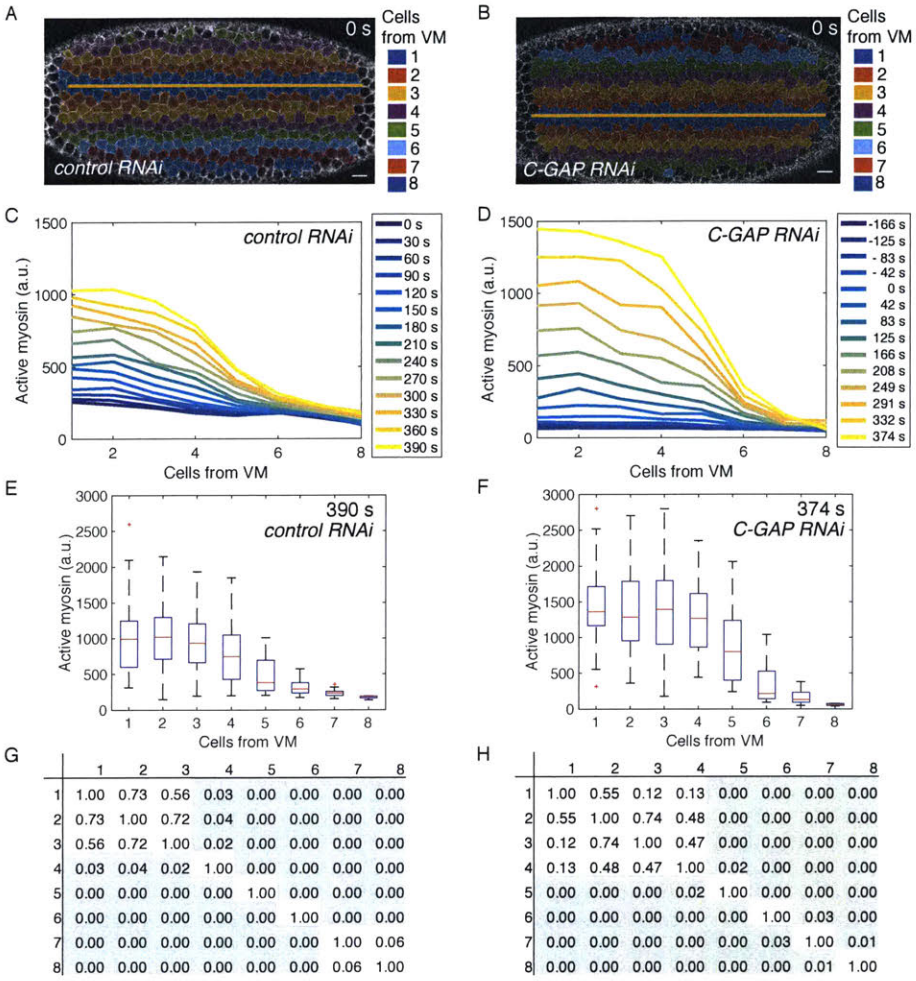

	1	2	3	4	5	6	7	8
1	1.00	0.73	0.56	0.03	0.00	0.00	0.00	0.00
2	0.73	1.00	0.72	0.04	0.00	0.00	0.00	0.00
3	0.56	0.72	1.00	0.02	0.00	0.00	0.00	0.00
4	0.03	0.04	0.02	1.00	0.00	0.00	0.00	0.00
5	0.00	0.00	0.00	0.00	1.00	0.00	0.00	0.00
6	0.00	0.00	0.00	0.00	0.00	1.00	0.00	0.00
7	0.00	0.00	0.00	0.00	0.00	0.00	1.00	0.06
8	0.00	0.00	0.00	0.00	0.00	0.00	0.06	1.00

	1	2	3	4	5	6	7	8
1	1.00	0.55	0.12	0.13	0.00	0.00	0.00	0.00
2	0.55	1.00	0.74	0.48	0.00	0.00	0.00	0.00
3	0.12	0.74	1.00	0.47	0.00	0.00	0.00	0.00
4	0.13	0.48	0.47	1.00	0.02	0.00	0.00	0.00
5	0.00	0.00	0.00	0.02	1.00	0.00	0.00	0.00
6	0.00	0.00	0.00	0.00	0.00	1.00	0.03	0.00
7	0.00	0.00	0.00	0.00	0.00	0.03	1.00	0.01
8	0.00	0.00	0.00	0.00	0.00	0.00	0.01	1.00

Figure 3.2: *C-GAP*-RNAi increases the width of the gradient of active myosin and the region of uniform active myosin around the VM. (A–B) Diagram of the cell bins of a control (*Rh3-RNAi*) (A) and *C-GAP*-RNAi (B) embryos. Cell membranes (gap43::mCh) are shown in grayscale. Cells, as identified by EDGE, are colored by the bin to which they are assigned. Yellow line denotes VM. **(C–D)** *C-GAP*-RNAi embryos increase myosin in cell bin 6, unlike in the control embryo. Plot shows distribution of average active myosin per cell bin as a function of distance from the VM at various times for the control-RNAi (C) and *C-GAP*-RNAi (D) embryos. **(E–F)** The distribution of active myosin at t = 390 s in the control embryo (E) and t = 374 s in a *C-GAP*-RNAi embryo (F). The distribution for each bin is depicted as a box plot. Red lines indicate median values, the box indicates inner quartiles, and dashed lines indicate outer quartiles. **(G–H)** *C-GAP*-RNAi increases the domain of cells with active myosin distributions that are not statistically different from each other. Table is of the p-values for each pair-wise statistical test (K–S test) each of the cell bins plotted in E and F, respectively. Green indicates $p < 0.05$. n varies for each cell bin and time point. **Note:** A, C, E, and G are all the same embryo and the same as in Fig. 2.4A, C, E, and G, with n = 44.5 cells/bin (mean) and 5 cells/bin (min). B, D, F, and H are all the same embryo and the same as Fig. 2.4B, D, F, and H, with n = 45.5 cells/bin (mean) and 3 cells/bin (min). Scale bars: 10 μm.

GAP-depleted embryos, whereas control embryos only have uniform levels of myosin activation within 2-3 cells of the VM (Fig. 3.2G,H, 3.3E,F).

3.1.2. Modulation of RhoA activity by C-GAP is required to create the normal tissue folding shape.

Next, I analyzed the effect of C-GAP depletion and the resulting change in the active

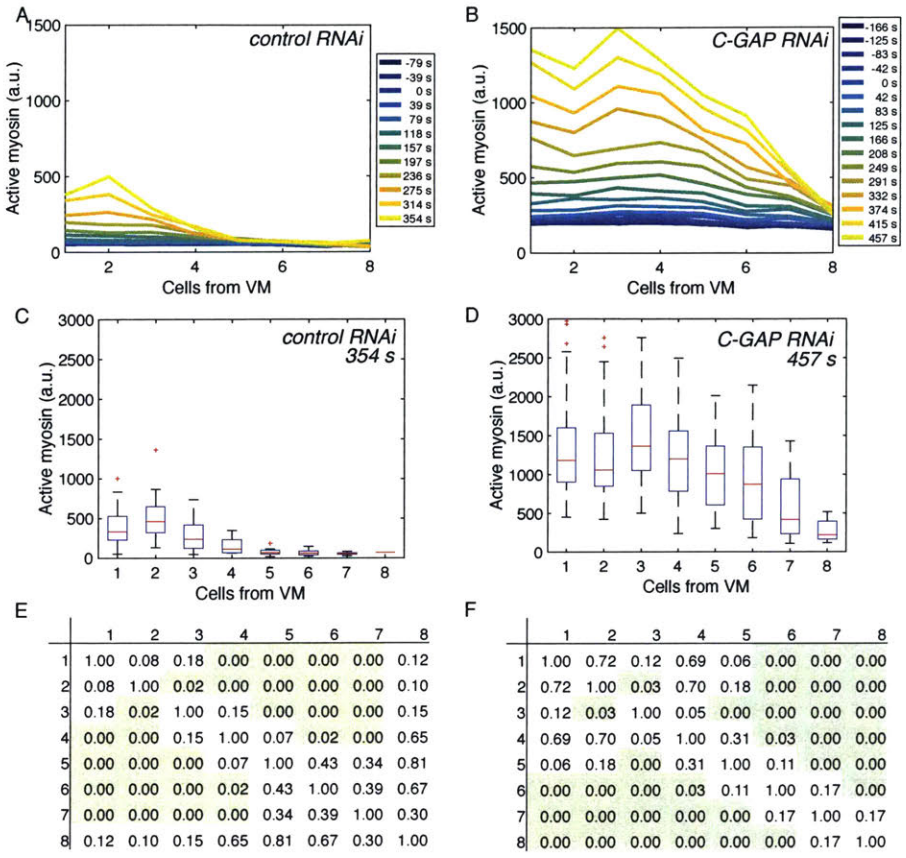

E

	1	2	3	4	5	6	7	8
1	1.00	0.08	0.18	0.00	0.00	0.00	0.00	0.12
2	0.08	1.00	0.02	0.00	0.00	0.00	0.00	0.10
3	0.18	0.02	1.00	0.15	0.00	0.00	0.00	0.15
4	0.00	0.00	0.15	1.00	0.07	0.02	0.00	0.65
5	0.00	0.00	0.00	0.07	1.00	0.43	0.34	0.81
6	0.00	0.00	0.00	0.02	0.43	1.00	0.39	0.67
7	0.00	0.00	0.00	0.00	0.34	0.39	1.00	0.30
8	0.12	0.10	0.15	0.65	0.81	0.67	0.30	1.00

F

	1	2	3	4	5	6	7	8
1	1.00	0.72	0.12	0.69	0.06	0.00	0.00	0.00
2	0.72	1.00	0.03	0.70	0.18	0.00	0.00	0.00
3	0.12	0.03	1.00	0.05	0.00	0.00	0.00	0.00
4	0.69	0.70	0.05	1.00	0.31	0.03	0.00	0.00
5	0.06	0.18	0.00	0.31	1.00	0.11	0.00	0.00
6	0.00	0.00	0.00	0.03	0.11	1.00	0.17	0.00
7	0.00	0.00	0.00	0.00	0.00	0.17	1.00	0.17
8	0.00	0.00	0.00	0.00	0.00	0.00	0.17	1.00

Figure 3.3: *C-GAP*-RNAi increases the width of the gradient of active myosin and the region of uniform active myosin around the VM. (A-B) Plot shows distribution of average active myosin per cell bin as a function of distance from the VM at various times for the control (*white*-RNAi) (A) and *C-GAP*-RNAi (B) embryo. (C-D) The distribution of active myosin at t = 354 s in the control embryo (C) and t = 457s in a *C-GAP*-RNAi embryo (D). The distribution for each bin is depicted as a box plot. Red lines indicate median values, the box indicates inner quartiles, and dashed lines indicate outer quartiles. (E-F) *C-GAP*-RNAi increases the domain of cells with active myosin distributions that are not statistically different from each other. Table is of the p-values for each pair-wise statistical test (K–S test) between the distribution of fluorescence intensity for each of the cell bins plotted in E and F, respectively. Green shading indicates statistical significance with $p < 0.05$. n varies for each cell bin and time point. **Note:** A, C, and E are all the same *white*-RNAi control embryo and the same as Fig. 2.5A, C, E, and G, with n = 36.6 cells/bin (mean) and 2 cells/bin (min). B, D, and F are all the same *C-GAP*-RNAi embryo and the same as Fig. 2.5B, D, F, and H, with n = 51.5 cells/bin (mean) and 3 cells/bin (min). Scale bars: 10 μm.

myosin gradient on the apical area in the same embryos. I calculated the average apical area for each time point over all cell bins. Consistent with our findings in Spn27A-depleted embryos, the broadening of the myosin gradient corresponds to a broadening of the gradient in apical constriction at all time points (Fig. 3.4A,B and 3.5A,B). There is a clear inflection point in the analysis of apical area with respect to cell distance from the VM over time (Fig. 3.4A,B, 3.5A,B). This point differentiates between cells that tend to constrict over time and cells that generally expand over time. This inflection point can be used define the width of the domain of apical

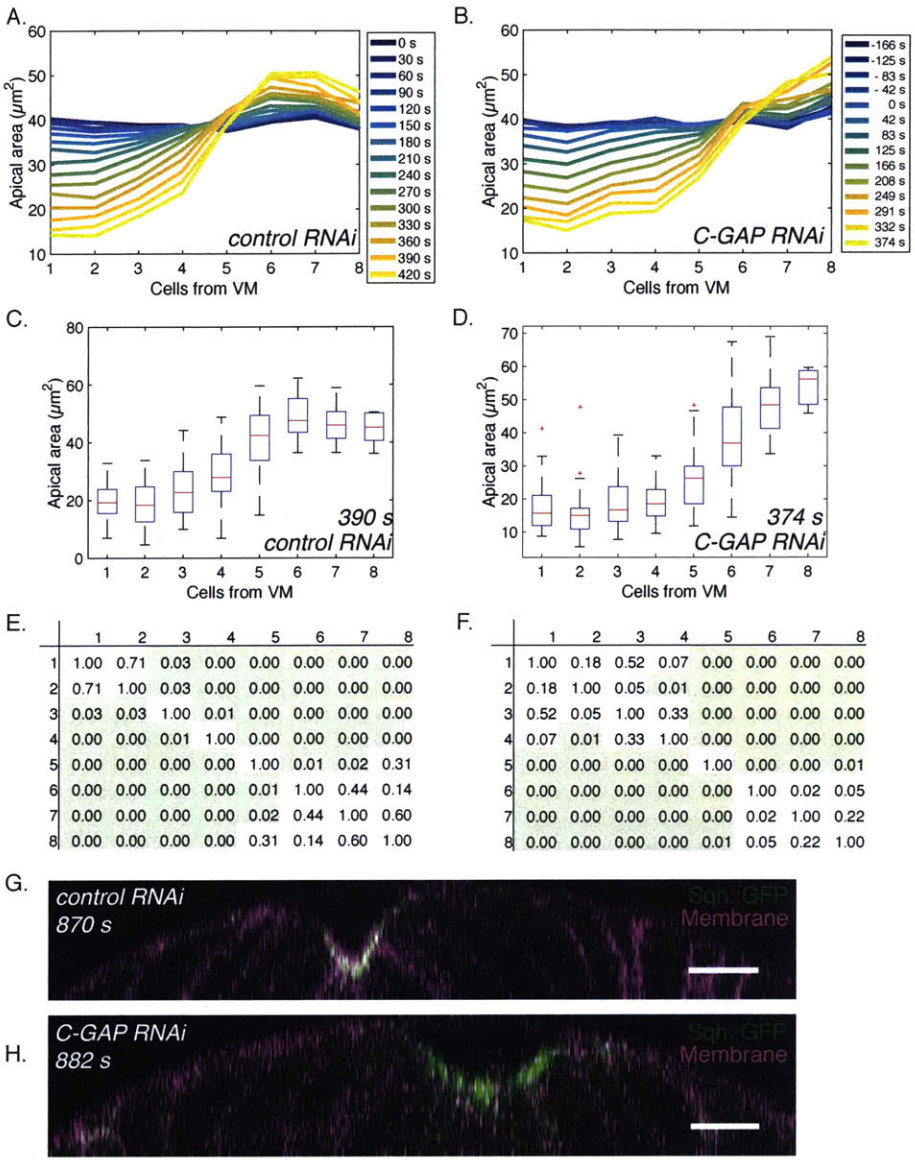

E.

	1	2	3	4	5	6	7	8
1	1.00	0.71	0.03	0.00	0.00	0.00	0.00	0.00
2	0.71	1.00	0.03	0.00	0.00	0.00	0.00	0.00
3	0.03	0.03	1.00	0.01	0.00	0.00	0.00	0.00
4	0.00	0.00	0.01	1.00	0.00	0.00	0.00	0.00
5	0.00	0.00	0.00	0.00	1.00	0.01	0.02	0.31
6	0.00	0.00	0.00	0.00	0.01	1.00	0.44	0.14
7	0.00	0.00	0.00	0.00	0.02	0.44	1.00	0.60
8	0.00	0.00	0.00	0.00	0.31	0.14	0.60	1.00

F.

	1	2	3	4	5	6	7	8
1	1.00	0.18	0.52	0.07	0.00	0.00	0.00	0.00
2	0.18	1.00	0.05	0.01	0.00	0.00	0.00	0.00
3	0.52	0.05	1.00	0.33	0.00	0.00	0.00	0.00
4	0.07	0.01	0.33	1.00	0.00	0.00	0.00	0.00
5	0.00	0.00	0.00	0.00	1.00	0.00	0.00	0.01
6	0.00	0.00	0.00	0.00	0.00	1.00	0.02	0.05
7	0.00	0.00	0.00	0.00	0.00	0.02	1.00	0.22
8	0.00	0.00	0.00	0.00	0.01	0.05	0.22	1.00

Figure 3.4: *C-GAP*-RNAi increases the width of the gradient of apical constriction and the region of uniform apical area around the VM. (A–B) Plot shows distribution of average apical area per cell bin as a function of distance from the VM at various times for the control (*Rh3*-RNAi) (A) and *C-GAP*-RNAi (B) embryo. (C–D) The distribution of apical areas for all cell bins at t = 390 s in the control embryo (C) and t = 374 s in a *C-GAP*-RNAi embryo (D). The distribution for each bin is depicted as a box plot. Red lines indicate median values, the box indicates inner quartiles, and dashed lines indicate outer quartiles. (E–F) *C-GAP*-RNAi increases the domain of cells with apical area distributions that are not statistically different from each other around the VM. Table is of the p-values for each pair-wise statistical test (K–S test) between the distribution of fluorescence intensity for each of the cell bins plotted in E and F respectively. Green shading indicates statistical significance with $p < 0.05$. n varies for each cell bin and time point. (G–H) Cross-sections of the embryo show that the *C-GAP*-RNAi embryo has a wildtype v-shaped furrow. Cross-sections are of control embryo at t = 870 s (G) and *C-GAP*-RNAi embryo at t = 882 s. Cross-sections are reconstructed from a z-stack. Myosin (sqh::GFP) is shown in green and membranes (gap43::mCH) in magenta. **Note:** A, C, and E are all the same *Rh3*-RNAi control embryo and the same as in Fig. 2.2A, C, E, G, with n = 44.5 cells/bin (mean) and 5 cells/bin (min). B, D, and F are all the same *C-GAP*-RNAi embryo and the same as in Fig. 2.2B, D, F, and H, with n = 45.5 cells/bin (mean) and 3 cells/bin (min). Scale bars: 10 μm.

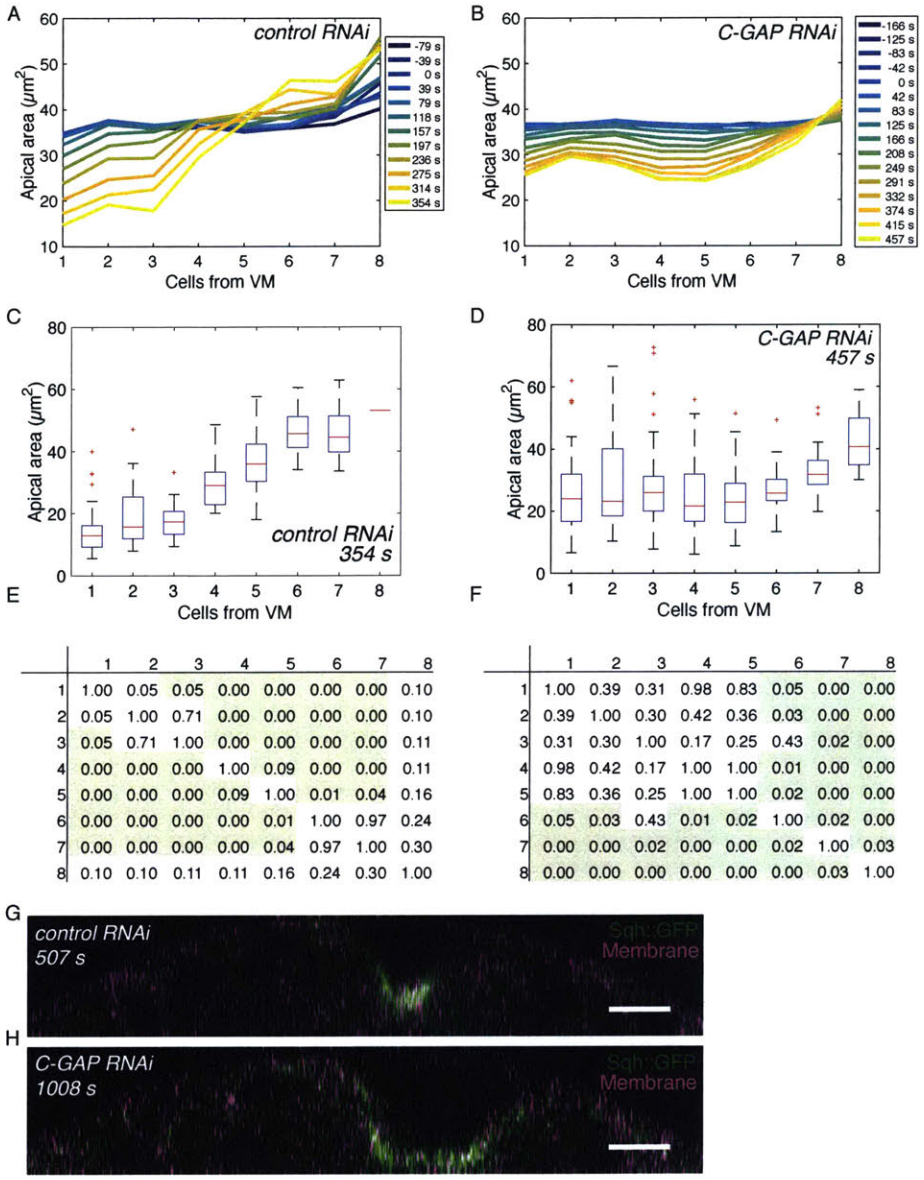

	1	2	3	4	5	6	7	8
1	1.00	0.05	0.05	0.00	0.00	0.00	0.00	0.10
2	0.05	1.00	0.71	0.00	0.00	0.00	0.00	0.10
3	0.05	0.71	1.00	0.00	0.00	0.00	0.00	0.11
4	0.00	0.00	0.00	1.00	0.09	0.00	0.00	0.11
5	0.00	0.00	0.00	0.09	1.00	0.01	0.04	0.16
6	0.00	0.00	0.00	0.00	0.01	1.00	0.97	0.24
7	0.00	0.00	0.00	0.00	0.04	0.97	1.00	0.30
8	0.10	0.10	0.11	0.11	0.16	0.24	0.30	1.00

	1	2	3	4	5	6	7	8
1	1.00	0.39	0.31	0.98	0.83	0.05	0.00	0.00
2	0.39	1.00	0.30	0.42	0.36	0.03	0.00	0.00
3	0.31	0.30	1.00	0.17	0.25	0.43	0.02	0.00
4	0.98	0.42	0.17	1.00	1.00	0.01	0.00	0.00
5	0.83	0.36	0.25	1.00	1.00	0.02	0.00	0.00
6	0.05	0.03	0.43	0.01	0.02	1.00	0.02	0.00
7	0.00	0.00	0.02	0.00	0.00	0.02	1.00	0.03
8	0.00	0.00	0.00	0.00	0.00	0.00	0.03	1.00

Figure 3.5: *C-GAP*-RNAi increases the width of the gradient of apical constriction and the region of uniform apical area around the VM. (A–B) Plot shows distribution of average apical area per cell bin as a function of distance from the VM for time points listed in the legend the control (*white*-RNAi) (A) and *C-GAP*-RNAi (B) embryo. **(C–D)** The distribution of apical areas for all cell bins at t = 390 s in the control embryo (C) and t = 374 s in a *C-GAP*-RNAi embryo (D). The distribution for each bin is depicted as a box plot. Red lines indicate median values, the box indicates inner quartiles, and dashed lines indicate outer quartiles. **(E–F)** *C-GAP*-RNAi increases the domain of cells with apical area distributions that are not statistically different from each other around the VM. Table is of the p-values for each pair-wise statistical test (K–S test) between the distribution of fluorescence intensity for each of the cell bins plotted in E and F respectively. Green indicates $p < 0.05$. n varies for each cell bin and time point. **(G–H)** Cross-sections of the embryo show that the *C-GAP*-RNAi embryo has a flattened domain around the VM. Cross-sections are of control embryo at t = 507 s (G) and *C-GAP*-RNAi embryo at t = 1008 s. Cross-sections are reconstructed from a z-stack. Myosin (sqh::GFP) is shown in green and membranes (gap43::mCH) in magenta. **Note:** A, C, E, and G are all the same *white*-RNAi control embryo and the same as in Fig. 2.3 A, C, and E, with n = 36.6 cells/bin (mean) and 3 cells/bin (min). B, D, F, and H are all the same *C-GAP*-RNAi embryo and the same as Fig. 2.3B, D, and F, with n = 51.5 cells/bin (mean) and 10 cells/bin (min). Scale bars: 10 μm.

constriction. In the control embryo, as in other wild-type embryos, the fourth row of cells is at the inflection point (Fig. 3.4A and 3.5A). In contrast, in the embryo depleted of C-GAP, the

sixth (Fig. 3.4B) or seventh (Fig. 3.5B) cell rows are the inflection point, indicating a broadening of the domain. Next, I analyzed the distribution of apical area in each cell bin at the same time points for which I analyzed the distribution of active myosin (3.4C,D and 3.5C,D). There is also an increase in the domain of statistically-significant uniform cell constriction, from two cells from the VM in the control embryos (Fig. 3.4E and Fig. 3.5E) to four and six cells from the VM for each of the C-GAP depleted embryos, respectively (Fig. 3.4F and 3.5F). The embryo with a greater expansion of the uniform myosin domain also exhibited a greater expansion of the uniform area domain.

Finally, I observed the shape of the fold by generating a cross-sectional view from the image stack for all embryos (Fig. 3.4G and 3.5G). In the C-GAP-depleted embryo with the narrower gradient in active myosin, I observed no difference in curvature from the control (Fig. 3.4G). In the embryo with the widest gradient of active myosin, there is clearly a distortion of the furrow shape at later time points (Fig. 3.5G). The furrow is flat around the VM and the tissue bends further from the VM. This distortion does resolve itself, and the embryo is able to fold. This is consistent with the very broad gradient in embryos depleted of Spn27A causing a flattening of the tissue around the VM as in Chapter 2. We cannot rule out the possibility that the furrow is misshapen due to a defect in apical constriction, as we know happens in C-GAP-depleted embryos. In this embryo, I also observed a region of uniform contractility that is wider than the region of uniform active myosin level (Fig. 3.3F vs. 3.5F). This is the only embryo in which this is observed, a result that may also be caused by an inhibition of apical constriction due to the role of C-GAP in dynamically inhibiting RhoA.

3.1.3. Gprk2 increases the width of the myosin and area gradient.

Next, I examined the effect of Gprk2, an inhibitor upstream of RhoA activation, on the shape of the myosin and area gradients. Previous analyses found that the lateral mesodermal cells behave more similarly to the ventral mesodermal cells in Gprk2 mutant embryos. My hypothesis was that this change in behavior is due to an expansion of the myosin gradient.

To assess the role of GPCR downregulation in the ventral domain, I quantified the distribution of active myosin in embryos that were depleted of Gprk2 by RNAi. Gprk2-depleted embryos were generated by crossing a UAS-driven shRNA targeting Grpk2 with a GAL4 maternal driver (See Methods for fly genetics). Cells in the embryo were binned based on their initial position from the VM, as for C-GAP (Fig. 3.6A,B). Average active myosin levels for each cell bin increase over time as the embryo folds in both control and Gprk2 RNAi embryos (Fig. 3.6C,D and 3.7A,B). There was variation in the phenotypes that I quantified in the Gprk2 RNAi embryos (Fig. 3.6D and 3.7A vs Fig. 3.7B). Of the three embryos that I quantified, two showed active myosin levels increasing in all cells in which it could be measured (Fig. 3.6D and 3.7A). I analyzed the distribution of myosin at specific time points; due to experimental limitations, some embryos were analyzed at earlier time points (as specified in Fig. 3.6E,F and 3.7C,D). The distribution of myosin in these cell bins is consistent with the averages reported for all time points. Statistical analysis shows that one embryo had an expanded domain of uniform active myosin of four cells from VM, as opposed to the three cells seen in the wild type (Fig. 3.6G,H). The other two embryos did not show an expansion of the domain of uniform myosin. This is possibly due to the fact that they were analyzed at earlier time points (Fig. 3.7E,F).

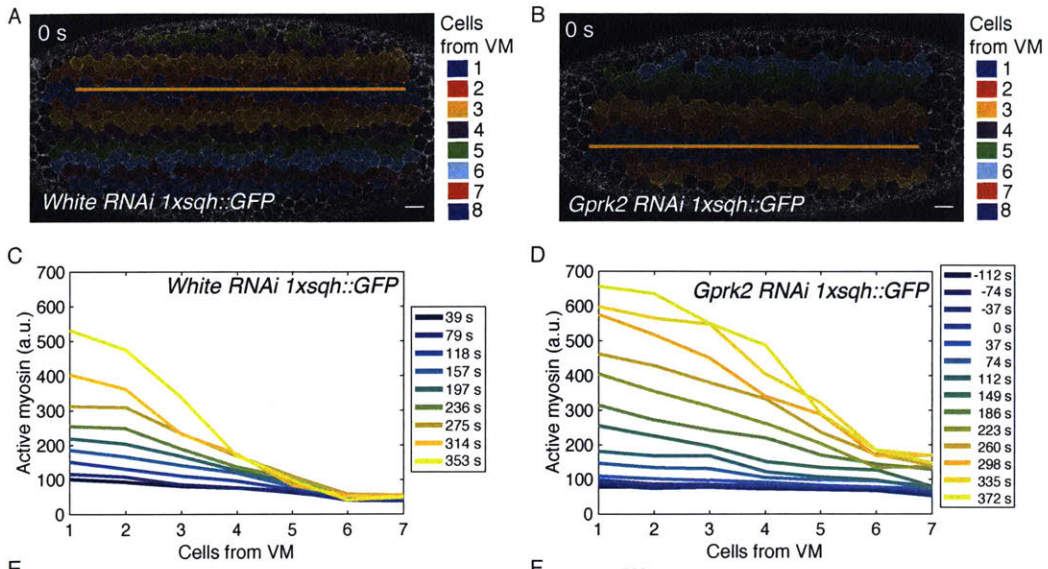

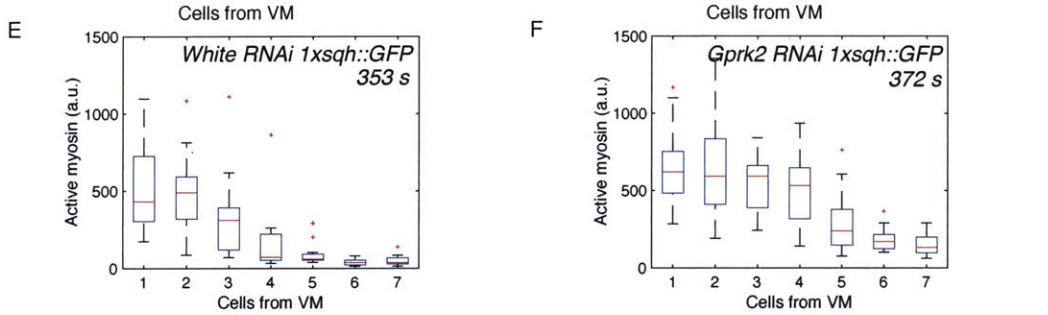

G

	1	2	3	4	5	6	7
1	1.00	0.78	0.11	0.00	0.00	0.00	0.00
2	0.78	1.00	0.02	0.00	0.00	0.00	0.00
3	0.11	0.02	1.00	0.02	0.00	0.00	0.00
4	0.00	0.00	0.02	1.00	0.79	0.01	0.04
5	0.00	0.00	0.00	0.79	1.00	0.00	0.00
6	0.00	0.00	0.00	0.01	0.00	1.00	0.73
7	0.00	0.00	0.00	0.04	0.00	0.73	1.00

H

	1	2	3	4	5	6	7
1	1.00	0.74	0.31	0.07	0.00	0.00	0.00
2	0.74	1.00	0.22	0.15	0.00	0.00	0.00
3	0.31	0.22	1.00	0.63	0.00	0.00	0.00
4	0.07	0.15	0.63	1.00	0.01	0.00	0.00
5	0.00	0.00	0.00	0.01	1.00	0.06	0.10
6	0.00	0.00	0.00	0.00	0.06	1.00	0.21
7	0.00	0.00	0.00	0.00	0.10	0.21	1.00

Figure 3.6: *Gprk2*-RNAi increases the width of the gradient of active myosin and the region of uniform active myosin around the VM. (A–B) Diagram of the cell bins of a control (*white*-RNAi) (A) and *Gprk2* -RNAi (B) embryo. Cell membranes (gap43::mCh) are shown in grayscale. Cells, as identified by EDGE, are colored by the bin to which they are assigned. Yellow line denotes VM. **(C–D)** *C-GAP*-RNAi embryos increase myosin in cell bins 6 and 7, unlike in the control embryo. Plot shows distribution of average active myosin per cell bin as a function of distance from the VM at various times for the control-RNAi (C) and *Gprk2*-RNAi (D) embryo. **(E–F)** The distribution of active myosin at t = 353 s in the control embryo (E) and t = 372 s in a *Gprk2*-RNAi embryo (F). The distribution for each bin is depicted as a box and whisker plot. Red lines indicate median values, box indicates inner quartiles, while dotted lines indicate outer quartiles. **(G–H)** *Gprk2*-RNAi increases the domain of cells with active myosin distributions that are not statistically different from each other from 3 to 4 cells. Table is of the p-values for each pair-wise statistical test (K-S test) for each of the cell bins plotted in E and F respectively. Green indicates $p < 0.05$. n varies for each cell bin and time point. **Note:** A, C, E, and G are all the same embryo and the same as in Fig. 2.8A, C, E, G, with n = 44. cells/bin (mean) and 13 cells/bin (min). B, D, F, and H are all the same embryo and the same as in Fig. 2.8B, D, F and H, with n = 29.7 cells/bin (mean) and 7 cells/bin (min). Scale bars: 10 μm

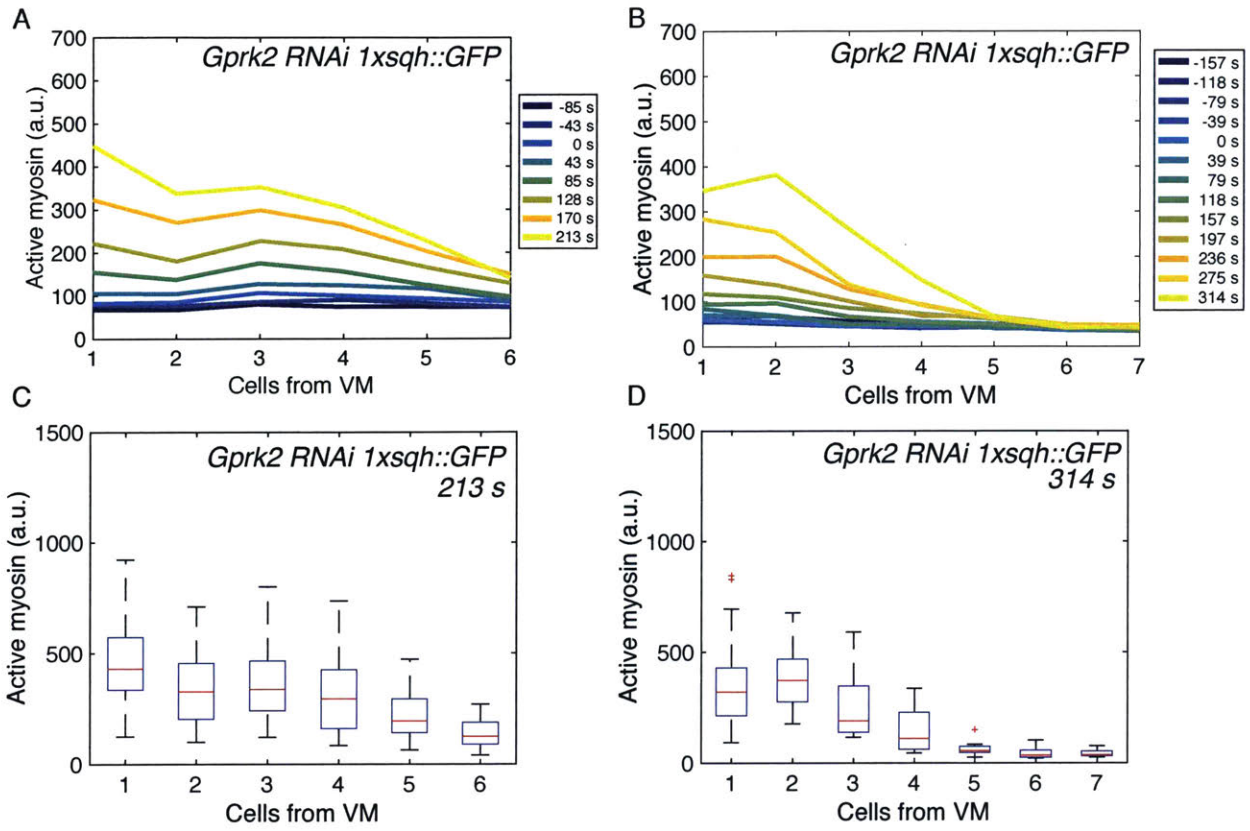

E

	1	2	3	4	5	6
1	1.00	0.06	0.06	0.01	0.00	0.00
2	0.06	1.00	0.96	0.69	0.00	0.00
3	0.06	0.96	1.00	0.37	0.01	0.00
4	0.01	0.69	0.37	1.00	0.09	0.00
5	0.00	0.00	0.01	0.09	1.00	0.00
6	0.00	0.00	0.00	0.00	0.00	1.00

F

	1	2	3	4	5	6	7
1	1.00	0.27	0.28	0.01	0.00	0.00	0.00
2	0.27	1.00	0.06	0.00	0.00	0.00	0.00
3	0.28	0.06	1.00	0.14	0.00	0.00	0.00
4	0.01	0.00	0.14	1.00	0.11	0.01	0.00
5	0.00	0.00	0.00	0.11	1.00	0.14	0.04
6	0.00	0.00	0.00	0.01	0.14	1.00	0.70
7	0.00	0.00	0.00	0.00	0.04	0.70	1.00

Figure 3.7: *Gprk2*-RNAi increases the width of the gradient of active myosin and the region of uniform active myosin around the VM in some but not all *Grpk2*-RNAi embryos. (A–B) Some *C-GAP*-RNAi embryos increase myosin in cell bins 6 (A) but not others (B). Plot shows distribution of average active myosin per cell bin as a function of distance from the VM at various time points for both *Gprk2*-RNAi embryos. **(C–D)** The distribution of active myosin at t = 213 s in one *Gprk2*-RNAi embryo (E) and t = 314 s the other *Gprk2*-RNAi embryo (F). The distribution for each bin is depicted as a box and whisker plot. Red lines indicate median values, box indicates inner quartiles, while dotted lines indicate outer quartiles. **(E–F)** *Gprk2*-RNAi does not increase the domain of cells with active myosin distributions that are not statistically different from each other from 3 to 4 cells in these two embryos. Table is of the p-values for each pair-wise statistical test (K–S test) between the distribution of fluorescence intensity for each of the cell bins plotted in E and F respectively. Green shading indicates statistical significance with $p<0.05$. n varies for each cell bin and time point. **Note:** A, C, and E are all the same embryo *Gprk2*-RNAi embryo and the same as Fig. 2.9A, C, E, G, with n = 52 cells/bin (mean) and 25 cells/bin (min). B, D, and F are all the same embryo and the same as Fig. 2.9B, D, F, and H, with n = 39 cells/bin (mean) and 8 cells/bin (min). Scale bars: 10 μm

3.1.4. Effect of Gprk2 depletion on the distribution of apical constriction.

Area is more easily comparable between embryos than active myosin levels, and in all of my previous analysis, expansion of the region of active myosin proportionally expands the region of constricting cells. Therefore, I examined the distribution of apical area in the same embryos to further examine whether there were differences in the patterning of the active myosin gradient. Measuring apical area over time, we see that the control embryo and two of the Gprk2-depleted embryos reduce their apical area in cell bins 1–4 over time (Fig. 3.8A and 3.9A,B). In the other Gprk2 embryo, cell bin five also reduces in area over time (Fig. 3.8B). There was a slight expansion of the region of uniform apical area to 3 cells, from the wildtype 2 cells, but this could also be due to the early time point of some of the measurements (Fig. 3.8E,F and 9E,F).

Finally, I did not observe a difference in the shape of the furrow between Gprk2-depleted and control embryos (Fig. 3.8G,H and Fig. 3.9G,H). There was no flattening of the furrow around the VM, which is consistent with the lack of increase in the uniform region of myosin activation around the VM.

These results indicate that Gprk2 depletion can expand both the region of myosin activation and apical area constriction, but less robustly than depletion of C-GAP. Because of the difference between my observations and the observations of the mutant phenotype, it may be the case that the depletion of Gprk2 was incomplete in the embryos I analyzed (Fuse et al., 2013). Additionally, I found that expansion of the region of uniform myosin around the ventral midline does not have an effect until it is at least two cells wider than in control embryos.

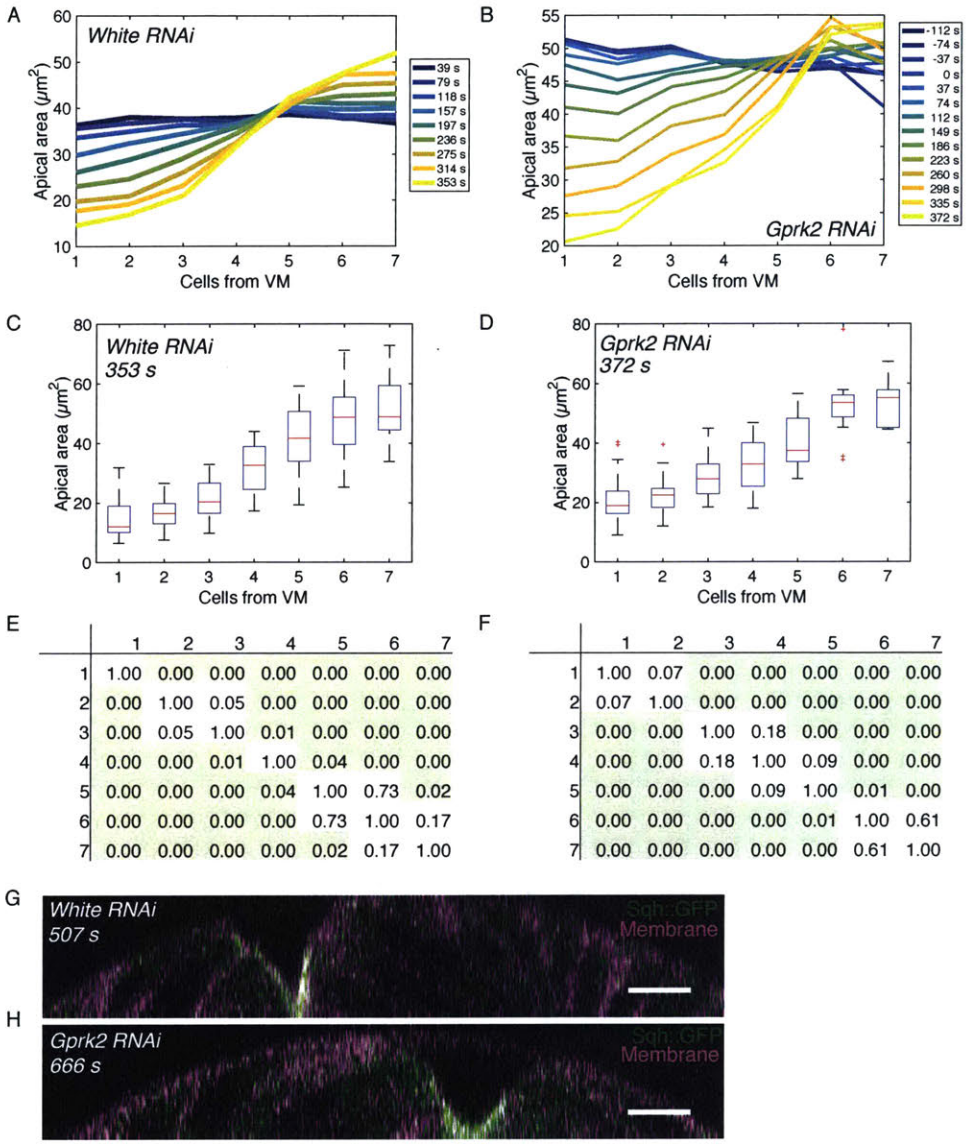

Figure 3.8: ***Gprk2* -RNAi increases the width of the gradient of apical constriction and the region of uniform apical area around the VM. (A–B)** Plot shows distribution of average apical area per cell bin as a function of distance from the VM for time points listed in the legend the control (*white*-RNAi) (A) and *Gprk2*-RNAi (B) embryo. **(C–D)** The distribution of apical areas for all cell bins at t=353 s in the control embryo (C) and t = 372 s in a *Gprk2*-RNAi embryo (D). The distribution for each bin is depicted as a box plot. Red lines indicate median values, the box indicates inner quartiles, and dashed lines indicate outer quartiles. **(E–F)** *Gprk2*-RNAi increases the domain of cells with apical area distributions that are not statistically different from each other around the VM. Table is of the p-values for each pair-wise statistical test (K–S test) between each of the cell bins plotted in C and D respectively. Green indicates statistical significance with $p<0.05$. n varies for each cell bin and time point. **(G–H)** Cross-sections of the embryo show that the *Gprk2*-RNAi embryo has a wildtype v-shaped furrow. Cross-sections are of control embryo at t = 507 s (G) and *Gprk2*-RNAi embryo at t = 666 s. Cross-sections are reconstructed from a z-stack. Myosin (sqh::GFP) is shown in green and membranes (gap43::mCH) in magenta. **Note:** A, C, E, and G are all the same *white*-RNAi control embryo and the same as in Fig. 2.6A, C, E, G, with n = 44 cells/bin (mean) and 13 cells/bin (min). B, D, F, and H are all the same *Gprk2*-RNAi embryo and the same as in Fig. 2.6B, D, F, and H, with n = 29.7 cells/bin (mean) and 7 cells/bin (min). Scale bars: 10 μm.

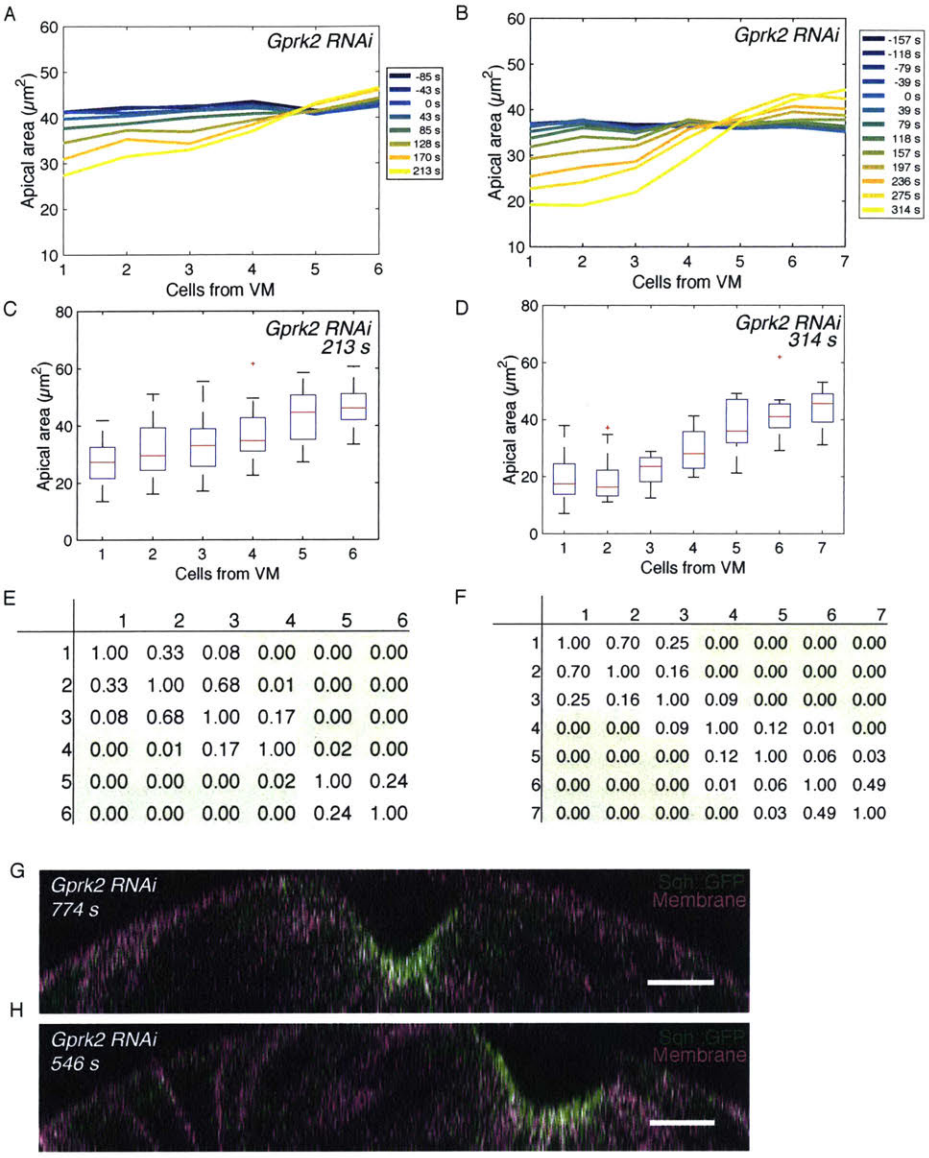

E

	1	2	3	4	5	6
1	1.00	0.33	0.08	0.00	0.00	0.00
2	0.33	1.00	0.68	0.01	0.00	0.00
3	0.08	0.68	1.00	0.17	0.00	0.00
4	0.00	0.01	0.17	1.00	0.02	0.00
5	0.00	0.00	0.00	0.02	1.00	0.24
6	0.00	0.00	0.00	0.00	0.24	1.00

F

	1	2	3	4	5	6	7
1	1.00	0.70	0.25	0.00	0.00	0.00	0.00
2	0.70	1.00	0.16	0.00	0.00	0.00	0.00
3	0.25	0.16	1.00	0.09	0.00	0.00	0.00
4	0.00	0.00	0.09	1.00	0.12	0.01	0.00
5	0.00	0.00	0.00	0.12	1.00	0.06	0.03
6	0.00	0.00	0.00	0.01	0.06	1.00	0.49
7	0.00	0.00	0.00	0.00	0.03	0.49	1.00

Figure 3.9: *Gprk2* -RNAi increases the width of the gradient of apical constriction and the region of uniform apical area around the VM. (A–B) Plot shows distribution of average apical area per cell bin as a function of distance from the VM at various time in two *Gprk2*-RNAi embryos. **(C–D)** The distribution of apical areas for all cell bins at t = 213 s in (C) and t = 314 s in (D). The distribution for each bin is depicted as a box plot. Red lines indicate median values, the box indicates inner quartiles, and dashed lines indicate outer quartiles. **(E–F)** *Gprk2*-RNAi increases the domain of cells with apical area distributions that are not statistically different from each other around the VM. Table is of the p-values for each pair-wise statistical test (K–S test) between each of the cell bins plotted in C and D respectively. Green indicates statistical significance with $p < 0.05$. n varies for each cell bin and time point. **(G–H)** Cross-sections of the embryo show that the *Gprk2*-RNAi embryo has a wildtype v-shaped furrow. Cross-sections of embryos at t = 774 s (G) and t = 546 s (H). Cross-sections are reconstructed from a z-stack. Myosin (sqh::GFP) is shown in green and membranes (gap43::mCH) in magenta. **Note:** A, C, E, and G are all the same embryo *Gprk2*-RNAi embryo and the same as Fig. 2.7A, C, E, with n = 52 cells/bin (mean) and 25 cells/bin (min). B, D, F, and H are all the same embryo and the same as Fig. 2.7B, D, F, with n = 39 cells/bin (mean) and 8 cells/bin (min). Scale bars: 10 μm

3.2. Discussion

Above, I found that depletion of known negative regulators of ventral furrow formation expands the gradient of active myosin. In the previous chapter, we noted that the gradients in upstream signaling components were generally broader than that of the more downstream components. Specifically, the distribution of active myosin in the C-GAP-RNAi embryos is similar in width to the distribution of T48 signal measured in the previous chapter. My findings in this chapter are consistent with C-GAP and Gprk2 both serving to narrow the gradient. When compared to the effect of depleting Spn27A, I found that the domain of active myosin was less expanded when depleting Gprk2 and C-GAP. This is consistent with our current understanding that both Gprk2 and C-GAP act downstream of the Twist signal, and thus myosin activity is still limited by the width of the Twist domain. I found that Gprk2 depletion less consistently expands the domain of active myosin and apical constriction. To differentiate between the phenotypic effect of Gprk2 depletion and C-GAP depletion, I would need to increase the number of embryos analyzed, particularly at later time points. It would be additionally useful to measure average levels of Gprk2 mRNA in the knock-down compared with control knock-down embryos to determine how much of the lack of phenotype is due to incomplete knock-down.

In addition to a widening of the gradient of active myosin in C-GAP-depleted embryos, I also observed a 1–2 cell increase in the region of uniform active myosin around the VM. This is consistent with a model in which inhibition of RhoA by C-GAP prevents RhoA from reaching saturation levels outside of the normal 2–3 cell domain of uniform myosin. To validate such a model, one would need to quantify the distribution of active RhoA, the distribution of the RhoA

input, RhoGEF2, and the distribution of C-GAP. Our current understanding of the distribution of active RhoA is based on the distribution of its downstream effector ROCK (Mason et al., 2013). The distribution of ROCK, the RhoA-dependent kinase that activates myosin in our system, has been measured on the per-cell level and localizes strongly with myosin in cells near the VM; this suggesting that it would closely track the gradient in active myosin. C-GAP is known to be maternally deposited, and our current hypothesis is that it acts uniformly across the ventral domain.

Finally, I suggest developing a method for quantifying tissue curvature in the furrow. This would allow a more careful analysis of the effect of changing the distribution of active myosin on tissue shape. This could be done be developing an image analysis program that could extract the shape from the cross-sectional view of the embryo. One would also need to develop a way of either averaging the shape over the length of the embryo, or creating an analysis that specifically associated curvature at a given anterior-posterior position to a specific level of active myosin at that position.

There is more work to be done to understand how the broader upstream signals are modulated over the course of the signaling pathway. I found that there was a subtle shift in the gradient of active myosin and apical constriction when C-GAP and Gprk2 are depleted. Detecting this subtle shift is dependent on the cell-level quantification techniques that I developed (Heer et al., 2017), and there are many more components of the pathway that can be measured using this technique. The *Drosophila* ventral furrow is one of the best-described systems of morphogenesis, allowing thorough characterization of all aspect of the system. Multiple discoveries from this system have been found to apply in other systems and contexts, and it is possible this discovery, that gradients in contractility are important for tissue folding,

might hold true in other systems as well.

3.3. Materials and Methods

Table 3.1

Stock	Genotype	Source/Reference
1	y[1] v[1]; P{TRiP.HMS00017}attP2; sqh::GFP (*white, Control shRNA*)	Perkins et al., 2015
2	y[1] sc[*] v[1]; P{TRiP.HMS00412}attP2 (*RhoGAP71E, C-GAP shRNA*)	Perkins et al., 2015
3	y[1] v[1]; P{TRiP.HMS00017}attP2 (*white, Control shRNA*)	Adapted from 2 by Frank Mason
4	y[1] sc[*] v[1]; P{TRiP.HMS00412}attP2; sqh::GFP (*RhoGAP71E, C-GAP shRNA*)	Adapted from 1 by Frank Mason
5	y[1] sc[*] v[1]; P{y[+t7.7] v[+t1.8]=TRiP.GL01052}attP2 (*Rh3* shRNA control line)	TRiP center*
7	w; mat67, Sqh::GFP; mat15, Gap43::mCherry/(TM3, Sb[1])	Vasquez et al., 2014
8	y[1] sc[*] v[1];P{TRiP.GL00233}attP2 (Gprk2 *shRNA*)	
F2 embryos imaged from these crosses, using above stock numbers/genotypes. Non-balancer females were used for cages.		**Figure**
	Stock # 4 x 7 (Virgins x males)	3.2, 3.3, 3.4, 3.5
	5 x 7	3.2, 3.4
	1 x 7	3.3, 3.5
	3 x 7	3.6, 3.8
	8 x 7	3.6, 3.7, 3.8, 3.9
	*Norbert Perrimon, Harvard Medical School and Howard Hughes Medical Institute, Boston, MA	

3.3.1. Fly stocks and genetics

Fly lines and crosses used in this chapter are listed in Table 3.1. Embryos were collected at 25 °C. Embryos from cross 1 and control cross 2 were collected from cages that had been aged more than 5 days to generate a consistent and mild phenotype. Modulation of RNAi levels are further described in (Jodoin et al., 2015).

3.3.2. Live imaging

C-Gap RNAi and control embryos were collected from cages that had been aged more than 5 days to standardize the phenotype. All embryos were dechlorinated in 50% bleach for 2 minutes, rinsed and mounted on slides coated with embryo glue (made by dissolving the adhesive from Scotch Tape in heptane). Embryos were visualized through a No. 1 coverslip, while immersed in Halocarbon 27 oil. Images were acquired with an Apochromatic 40x/1.2 numeric aperture W Korr M27 objective on a Zeiss 710 microscope, with pinhole size 1 AU. A 488/561 beam splitter was used to acquire (Detector range: 493.0–560.8 nm and 599.0–696.0 nm) and excite (Argon 488 LASER, 15.0% and DPSS 561-10, 2.0% and 5.0%) channels concurrently.

3.3.3. Image processing

Images were analyzed using Fiji (http://fiji.sc) (Schindelin et al., 2012) and MATLAB (MathWorks). Custom image processing software is available upon request. The myosin signal was processed as described in Chapter 2. The myosin signal (sqh::GFP) was thresholded at 2.5 standard deviations above the mean of the cytoplasmic background signal. Myosin signal was averaged over the 4 μm above the embryo surface. Images were segmented using the custom Embryo Development Geometry Explorer (EDGE) MATLAB package (Gelbart et al., 2012). Membrane signal (gap43::mCherry) was used to identify cell boundaries and track cells in time. Errors in the segmentation software were manually corrected. EDGE was used to measure cell centroid position, cell vertex position, cell diameter, cell area, and total myosin signal within a cell.

3.3.4. Image Analysis

To measure the tissue-level distribution of myosin relative to the VM independently of the displacement of cells with time, cells were binned based on their position relative to the VM.

Cells were assigned to bins based on the position of the cell centroid in the initial image. For most embryos, the boundaries of each bin were set by the average cell diameter. For embryos that began apical constriction prior to the time point of the image, the boundaries of each bin were empirically determined as some fraction of the average cell diameter as described in Section 2.4.5 (Fig. 3.6A,C,E and 3.7A,C,E).

3.3.5. Temporal alignment

Time 0 for each embryo was set as the time point immediately preceding the onset of average area reduction for the area of cell bin 1. For one control embryo that had begun apical area reduction prior to the first image acquired, I gave the first image a time of 39s, which was the length of the time steps between images (Fig. 3.6A,C,E and 3.7A,C,E). This was an approximation based on the apical area in cell bin 1 compared to the average area in the other cell bins.

3.3.6. Statistical analysis

Statistical analysis done using the MATLAB Statistics and Machine Learning Toolbox. The significance was determined using a Kolmogorov-Smirnov test with $\alpha = 0.05$.

3.4. References

Coravos, J.S., Martin, A.C., 2016. Apical Sarcomere-like Actomyosin Contracts Nonmuscle *Drosophila* Epithelial Cells. *Dev Cell* 39, 346-358.

Costa, M., Wilson, E.T., Wieschaus, E., 1994. A putative cell signal encoded by the folded gastrulation gene coordinates cell shape changes during *Drosophila* gastrulation. *Cell* 76, 1075-1089.

Fuse, N., Yu, F., Hirose, S., 2013. Gprk2 adjusts Fog signaling to organize cell movements in *Drosophila* gastrulation. *Development* 140, 4246-4255.

Gelbart, M.A., He, B., Martin, A.C., Thiberge, S.Y., Wieschaus, E.F., Kaschube, M., 2012. Volume conservation principle involved in cell lengthening and nucleus movement during tissue morphogenesis. *Proc Natl Acad Sci U S A* 109, 19298-19303.

Hacker, U., Perrimon, N., 1998. DRhoGEF2 encodes a member of the Dbl family of oncogenes and controls cell shape changes during gastrulation in *Drosophila*. *Genes Dev* 12, 274-284.

Heer, N.C., Miller, P.W., Chanet, S., Stoop, N., Dunkel, J., Martin, A.C., 2017. Actomyosin-based tissue folding requires a multicellular myosin gradient. *Development* 144, 1876-1886.

Jodoin, J.N., Coravos, J.S., Chanet, S., Vasquez, C.G., Tworoger, M., Kingston, E.R., Perkins, L.A., Perrimon, N., Martin, A.C., 2015. Stable Force Balance between Epithelial Cells Arises from F-Actin Turnover. *Dev Cell* 35, 685-697.

Kanesaki, T., Hirose, S., Grosshans, J., Fuse, N., 2013. Heterotrimeric G protein signaling governs the cortical stability during apical constriction in *Drosophila* gastrulation. *Mech Dev* 130, 132-142.

Kolsch, V., Seher, T., Fernandez-Ballester, G.J., Serrano, L., Leptin, M., 2007. Control of *Drosophila* gastrulation by apical localization of adherens junctions and RhoGEF2. *Science* 315, 384-386.

Leptin, M., Grunewald, B., 1990. Cell shape changes during gastrulation in *Drosophila*. *Development* 110, 73-84.

Lim, B., Levine, M., Yamakazi, Y., 2017. Transcriptional Pre-patterning of *Drosophila* Gastrulation. *Curr Biol* 27, 286-290.

Mason, F.M., Tworoger, M., Martin, A.C., 2013. Apical domain polarization localizes actin-myosin activity to drive ratchet-like apical constriction. *Nat Cell Biol* 15, 926-936.

Mason, F.M., Xie, S., Vasquez, C.G., Tworoger, M., Martin, A.C., 2016. RhoA GTPase inhibition organizes contraction during epithelial morphogenesis. *J Cell Biol* 214, 603-617.

Reeves, G.T., Trisnadi, N., Truong, T.V., Nahmad, M., Katz, S., Stathopoulos, A., 2012. Dorsal-ventral gene expression in the *Drosophila* embryo reflects the dynamics and precision of the dorsal nuclear gradient. *Dev Cell* 22, 544-557.

Richards, D.M., Saunders, T.E., 2015. Spatiotemporal analysis of different mechanisms for interpreting morphogen gradients. *Biophys J* 108, 2061-2073.

Rogers, S.L., Wiedemann, U., Hacker, U., Turck, C., Vale, R.D., 2004. *Drosophila* RhoGEF2 associates with microtubule plus ends in an EB1-dependent manner. *Curr Biol* 14, 1827-1833.

Schindelin, J., Arganda-Carreras, I., Frise, E., Kaynig, V., Longair, M., Pietzsch, T., Preibisch, S., Rueden, C., Saalfeld, S., Schmid, B., Tinevez, J.Y., White, D.J., Hartenstein, V., Eliceiri, K., Tomancak, P., Cardona, A., 2012. Fiji: an open-source platform for biological-image analysis. *Nat Methods* 9, 676-682.

Chapter 4. Concluding thoughts

Natalie C. Heer

Section 4.1 is adapted from: Heer, N. C. & Martin, A. C. Tension, contraction, and tissue morphogenesis. *Development* **144**, 4249–4260 (2017).

Broadly speaking, this dissertation serves to link the fields of tissue mechanics and developmental patterning. This link is possible because of the elegance of the *Drosophila* embryo as a model system and because of the extensive work that has preceded me in the field. First, I summarize my work in the context of tissue morphogenesis and relate it to the field of tissue mechanics. Looking towards the future, I next describe below some possible approaches to continue the work described in this dissertation.

4.1. Resistance: the interplay of tension and stiffness

From the work in this dissertation we can start to outline a paradigm by which the tissue-level organization of actomyosin contractility affects the individual cell shape changes and ultimately tissue shape. We can think of the tissue level organization of myosin activation as creating tension fields in which individual cells constrict in a manner that depends on their intrinsic contractility and the contractility of their neighbors. Specifically, in the context of a tissue, isotropic cell contractility can result in anisotropic forces and tissue movements, depending on how contractility is organized at the tissue level.

In the formation of the *Drosophila* ventral furrow, the ellipsoid shape of the embryo and the different distribution of myosin activation along the anterior-posterior vs. ventral-dorsal axes establishes an inherent asymmetry that orients tissue curvature along the ventral-dorsal axis,

forming a long, narrow furrow (Fig. 4.1A). In this system, cells initially have a radial organization to the cytoskeleton and in the absence of surrounding forces, contract isotropically (Fig. 4.1B) (Chanet et al., 2017; Coravos and Martin, 2016; Martin et al., 2010). However, the domain of cells expressing the transcription factors that promote contractility is rectangular (~ 70 cells long and 18 cells wide), and there is a ventral-dorsal gradient in the transcription of genes that promote contractility (Fig. 4.1B) (Heer et al., 2017; Lim et al., 2017). A consequence of this gradient being along the dorsal-ventral axis is that there is more-or-less uniform contractility and force balance along the anterior-posterior axis (Fig. 4.1C). The balanced contractile forces between neighboring cells prevents robust apical constriction along the anterior-posterior axis and leads to tension along that axis (Martin et al., 2010; Sweeton et al., 1991). In contrast, the gradient and resulting imbalance in contractility along the ventral-dorsal axis provides less resistance to cell constriction. This allows cells to mostly constrict along the ventral-dorsal axis and prevents the buildup of cortical tension along this axis (Chanet et al., 2017; Heer et al., 2017). The result is the formation of the wedge-shaped cells that fold the tissue along the ventral-dorsal axis (Fig. 4.1B vs 4.1C). The formation of wedge-shaped cells in the *Drosophila* ventral furrow is also regulated by basolateral cortical tension that initially resists tissue deformation. Basal expansion of the ventral cells is associated with a decrease in basal myosin levels and vertex modeling predicts that this is important for the formation of wedge-shaped cells (Polyakov et al., 2014). Thus, the organization of the region of active contractility and actomyosin-based resistance from neighboring contractile cells, in combination with resistance within the cell, affects both the individual cell shape changes as well as the overall tissue architecture.

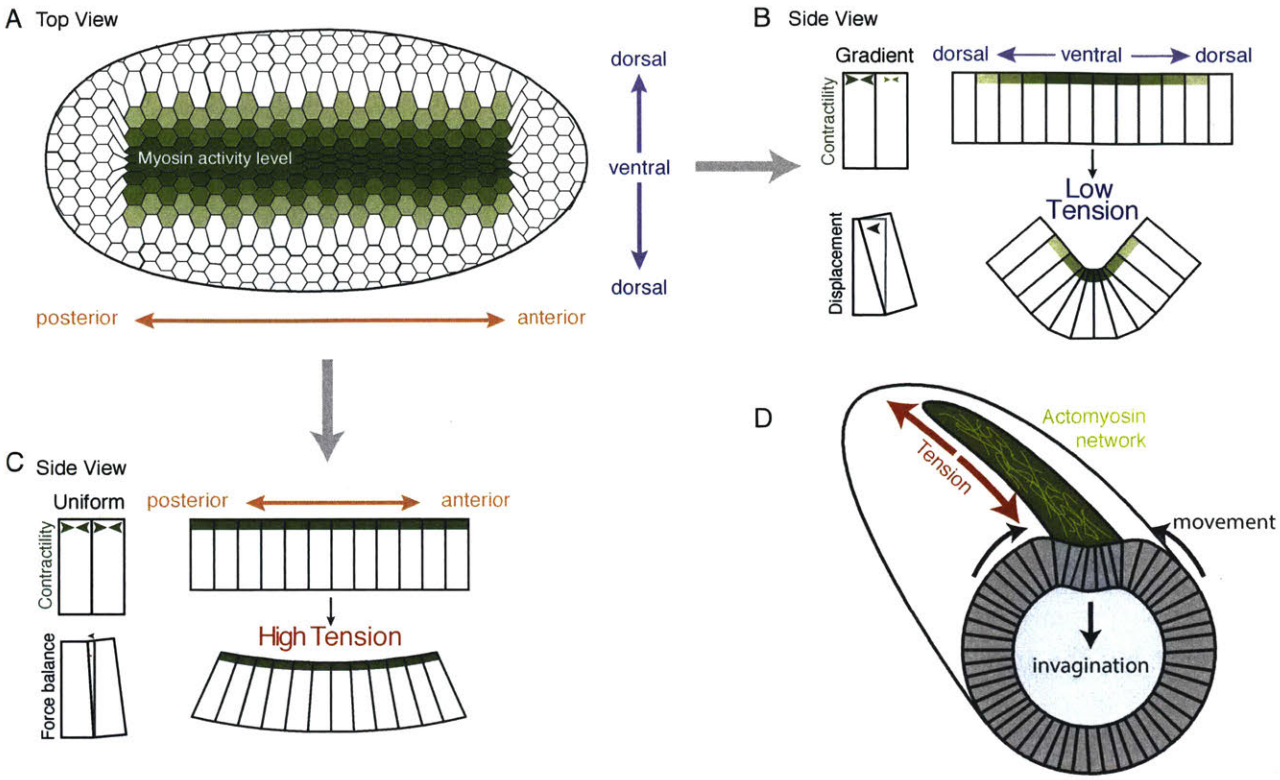

Figure 4.1: Diagram of the spatial pattern of contractility that results in *Drosophila* ventral furrow formation. (A) Surface view of the ventral surface of the embryo. Distribution and magnitude of myosin activity is in green (darker green, more myosin activity). Anterior-posterior axis is in orange and dorsal-ventral axis is in purple. (B) Diagram showing how an apical contractility gradient causes a force imbalance that allows cells to constrict and the tissue to bend along the dorsal-ventral axis. (C) Diagram showing how uniform apical contractility along the anterior-posterior axis promotes balanced forces and tension, which prevents tissue bending along this axis. (D) Diagram of the embryo in the process of folding with the orientation of actomyosin fibers diagramed in yellow.

In addition to the pre-pattern in gene expression (Heer et al., 2017; Lim et al., 2017), mechanical feedback influences cytoskeletal organization and, presumably, force generation (Chanet et al., 2017). In both experiment and theory, actomyosin meshworks orient along the axis that is most resistant to constriction, possibly allowing greater tension to accumulate along that axis (Fig. 4.1D, yellow fibers). A remarkable illustration of the integrated nature of cell force generation and organism shape is that converting *Drosophila* embryos from an ellipsoid shape to a round shape disrupts the organization of the actomyosin meshworks in cells and the anisotropic tension in the tissue (Chanet et al., 2017). While it is still necessary to find a way to specifically

perturb this feedback loop, it is possible that this mechanism is important to reinforce cues provided by the pre-pattern in gene expression. I next explore three possible pathways to further our knowledge of this system.

4.2. Why is a multi-layered signaling pathway necessary?

The most difficult questions to answer in biology are the "why" questions. In this case we are presented with the question of why there are so many levels of the signaling pathway between *twist* and apical myosin activation if its primary purpose is to simply transform one gradient signal into another gradient signal. The purpose of myosin in generating a gradient in apical area is evident, but the answer is less clear for the more upstream components. A multi-tiered setup is even more puzzling because each step of the pathway introduces additional noise into the system. This ostensibly makes it harder for an individual cell to interpret a morphogen gradient and generate the correct output, such as correct cell fate or an appropriate amount of actomyosin contractility. However, a recent study has shown that multi-layered pathways can actually improve information transfer in some situations, even when each layer is increasingly noisy (Tikhonov et al., 2015). In particular, this applies to pathways in which the downstream components of the pathway are able to access the information of more upstream components, as in a feed-forward network. Tikhonov et al. validated this model for the case of anterior-posterior patterning in the *Drosophila* embryo, in which the enhancers and promotors of the pair-rule genes are bound not just by the transcription factors immediately preceding them in the pathway, but also by more upstream transcription factors such as Bicoid. As our system also exhibits a multi-step pathway, it is worth exploring whether a similar model could describe the interactions in our pathway, and thus explain the multiple steps to interpret the gradient. For example, it is

possible that T48 may allow RhoGEF2 to directly read the accumulated levels of Twist activity independent of Fog activation of the GPCR pathway. The role of negative regulators in our system also suggests that the multiple layers of the pathway may serve to increase robustness (Richards and Saunders, 2015).

A successful application of this model would first require additional experimental evidence as well. Most importantly we need quantitative measurements of additional pathway components that have yet to be measured, including the positive regulators RhoGEF2, RhoA, and ROCK, and the negative regulators C-GAP, Gprk2 and MBS, an inhibitor of myosin that is important for proper furrow formation (Vasquez et al., 2014). In the context of these measurements, we must also address the question of whether a fluorescence measurement of protein levels is a true reflection of activity levels. We are able to approximate activity levels for myosin using our thresholding mechanism, which is based on empirical evidence and our understanding of how the myosin motor is activated (see Section 2.2.1). We do not yet have an equivalent understanding for RhoGEF2 or C-GAP. Since most of these components become localized to the apical domain when the pathway is activated, we could build models to infer the relative levels of active and inactive molecules from localized fluorescent signals. This would rely on the fluorescence intensity distribution in different parts of cells in the embryo and be validated using mutants that either over-activate or inhibit the component. Additionally, the lateral domains of embryos could be used as an internal control for background levels of fluorescence. Imaging lateral and ventral domains concurrently at a high time resolution is difficult using confocal microscopy; however, if we instead use light sheet fluorescence microscopy, a greater region of the embryo can be captured in less time. Thus, we would be able to quantify RhoGEF2 and other pathway components in both the ventral and lateral domains.

4.3. A question of timing

A more careful dissection of the time-dependent nature of the gradients of the upstream components is an important next step for generating a model of the input-output relationship between the Twist gradient and the downstream active myosin gradient. Much of the work presented here focuses on a single time point, at which the statistical significance of the gradient is assessed, while in reality the gradient of each of the components changes over time. This aspect of the gradient merits further exploration, as it is possible that the region of uniform myosin also varies across time. If this is borne out in experiments, it would be an important feature of any model of how the gradient in Twist activity causes a gradient in myosin activity. The advances presented in this dissertation allow us to compare the distribution of different components at different time points, but there is much that is unknown about the timing of these features. Of particular interest to me is how Twist activity corresponds to myosin activity on the individual-cell level. Much of the previous work in this system has focused on the variability in myosin accumulation and apical area reduction between neighboring cells (Martin et al., 2009; Vasquez et al., 2014; Xie and Martin, 2015; Xie et al., 2016). By averaging the properties of neighboring cells together, I was able to show a correspondence between input and output factors. Future analysis of this multicellular gradient requires that we address cell-to-cell variability and dynamics that naturally occur in this system.

4.4. Manipulating contractility in the embryo.

A true understanding of how contractility can cause different embryonic shapes to develop will depend on the ability to precisely control patterns of contractility in the embryo. This dissertation and other research have relied on genetic perturbations to change the pattern of

contractility in the *Drosophila* embryo. Additional perturbations can be achieved by drug injection and laser ablation, as well as an optogenetic approach to inhibit actin polymerization (Coravos and Martin, 2016; Guglielmi et al., 2015; Martin et al., 2010). An ideal tool for exploring how contractile patterning affects tissue shape would be optogenetic activation of contractility. A recently developed system has been able to activate RhoA in cell culture by optogenetically targeting the catalytic domain (DHPH) of a RhoGEF, ARHGEF11, to the plasma membrane. This was done by fusing the DHPH domain to CRY2, half of a light controlled dimerization pair, while the other half, CIBN, was targeted to the plasma membrane (Valon et al., 2017). In the presence of blue light, this system rapidly and specifically increases the force exerted by a cell as measured by traction force microscopy (Trepat et al., 2009). Adapting this system to work in *Drosophila* would allow us to more expansively probe the phase space of our mathematical model presented in Chapter 2. To implement this system in *Drosophila*, I would suggest using the GEF domain (DHPH) from DRhoGEF2. Additionally, I would suggest targeting the GEF domain specifically to the apical domain of the epithelium.

Specific experiments that I would suggest are generating a region of contractility with sharp boundaries, which would allow us to determine if there is a certain width to the graded region of myosin contractility that is required for folding. We could also find the minimum number of contractile cells necessary to form a furrow. Currently we know that embryos are still able to furrow if the domain of actomyosin contractility is widened, but we don't yet know if there is a lower limit on how wide the domain of contractility could be. I suggest doing these experiments in a *twist* or *snail* null background to eliminate existing pattering of the contractile domain. This would also allow us to test for the requirement of pathways outside of the RhoA/ROCK pathway in activation apical contractility.

Before experimenting with different shapes of contractile organization, we would need to test whether the optogenetic system was able to promote contractility in a *snail* mutant. As discussed previously, *snail* controls pathways that are possibly independent of RhoA, such as the repression of the *bearded* genes (Chanet and Schweisguth, 2012; Perez-Mockus et al., 2017). If the optogenetic system was able to generate contractility in *snail* mutant embryos, we could conclude that the control of contractility by Neuralized was functioning through RhoGEF2.

The optogenetic system would also be able to test whether the localization of RhoGEF2 to the center of the apical domain (medioapical) is required to generate contractility (Coravos and Martin, 2016; Mason et al., 2016). It is currently known that downstream of RhoGEF2, ROCK must be localized to the medioapical domain to generate contractility, but it is not yet clear whether that localization depends on the medial localization of RhoGEF2 localization (Coravos and Martin, 2016). By illuminating the tissue uniformly, RhoA would receive a uniform activation signal, but still be dynamically deactivated by C-GAP. This experiment would need to be performed in a *twist* mutant background so we could rule out the case where endogenous RhoGEF2 activity would be sufficient to polarize RhoA. I would first perform this experiment with labeled ROCK to determine whether active RhoA was able to spatial polarize in the context of uniform activation. I would also measure the ability of these cells to generate apical constriction, to determine the requirements of polarized RhoGEF2 signal to contractility.

4.5. Conclusion

Spatiotemporal patterning and tissue morphogenesis is fascinating. Here I measured the spatiotemporal pattern of active myosin in the *Drosophila* ventral furrow. I found that active myosin is present in a gradient that increases with time. The gradient was measured as a function

of cells from the ventral midline. Active myosin levels are uniform within 2-3 cells from the ventral midline. Cells 4-6 have distinct distributions of active myosin at each position creating a distribution best described as a gradient. This gradient in active myosin corresponds to a gradient in apical contractility. I defined the gradient in contractility as being uniform within 1-2 cells of the ventral midline with cells 2-4 constricting with different distributions of area at each position. I found that the gradient in active myosin and area depends on a gradient in upstream factors *twist* and the Twist target, T48. I measure Twist mRNA to be in a gradient from cells 2-12 from the ventral midline, and T48 to be in a gradient from 2-8 cells from the ventral midline. I also found that the presence of a gradient in active myosin near the ventral midline is required for normal furrow shape. Finally, I found that the position of the gradient in active myosin depends on the presence of two inhibitors of signaling downstream of Twist, Gprk2 and C-GAP. This is the first step in understanding how tissue level spatiotemporal patterning of actomyosin contractility specifically controlled, and how it affects morphogenesis.

4.6. References

Chanet, S., Miller, C.J., Vaishnav, E.D., Ermentrout, B., Davidson, L.A., Martin, A.C., 2017. Actomyosin meshwork mechanosensing enables tissue shape to orient cell force. *Nat Commun* 8, 15014.

Chanet, S., Schweisguth, F., 2012. Regulation of epithelial polarity by the E3 ubiquitin ligase Neuralized and the Bearded inhibitors in *Drosophila*. *Nat Cell Biol* 14, 467-476.

Coravos, J.S., Martin, A.C., 2016. Apical Sarcomere-like Actomyosin Contracts Nonmuscle *Drosophila* Epithelial Cells. *Dev Cell* 39, 346-358.

Guglielmi, G., Barry, J.D., Huber, W., De Renzis, S., 2015. An Optogenetic Method to Modulate Cell Contractility during Tissue Morphogenesis. *Dev Cell* 35, 646-660.

Heer, N.C., Miller, P.W., Chanet, S., Stoop, N., Dunkel, J., Martin, A.C., 2017. Actomyosin-based tissue folding requires a multicellular myosin gradient. *Development* 144, 1876-1886.

Lim, B., Levine, M., Yamakazi, Y., 2017. Transcriptional Pre-patterning of *Drosophila* Gastrulation. *Curr Biol* 27, 286-290.

Martin, A.C., Gelbart, M., Fernandez-Gonzalez, R., Kaschube, M., Wieschaus, E.F., 2010. Integration of contractile forces during tissue invagination. *J Cell Biol* 188, 735-749.

Martin, A.C., Kaschube, M., Wieschaus, E.F., 2009. Pulsed contractions of an actin-myosin network drive apical constriction. *Nature* 457, 495-499.

Mason, F.M., Xie, S., Vasquez, C.G., Tworoger, M., Martin, A.C., 2016. RhoA GTPase inhibition organizes contraction during epithelial morphogenesis. *J Cell Biol* 214, 603-617.

Perez-Mockus, G., Mazouni, K., Roca, V., Corradi, G., Conte, V., Schweisguth, F., 2017. Spatial regulation of contractility by Neuralized and Bearded during furrow invagination in *Drosophila*. *Nat Commun* 8, 1594.

Polyakov, O., He, B., Swan, M., Shaevitz, J.W., Kaschube, M., Wieschaus, E., 2014. Passive mechanical forces control cell-shape change during *Drosophila* ventral furrow formation. *Biophys J* 107, 998-1010.

Richards, D.M., Saunders, T.E., 2015. Spatiotemporal analysis of different mechanisms for interpreting morphogen gradients. *Biophys J* 108, 2061-2073.

Sweeton, D., Parks, S., Costa, M., Wieschaus, E., 1991. Gastrulation in *Drosophila*: the formation of the ventral furrow and posterior midgut invaginations. *Development* 112, 775-789.

Tikhonov, M., Little, S.C., Gregor, T., 2015. Only accessible information is useful: insights from gradient-mediated patterning. *R Soc Open Sci* 2, 150486.

Trepat, X., Wasserman, M.R., Angelini, T.E., Millet, E., Weitz, D.A., Butler, J.P., Fredberg, J.J., 2009. Physical forces during collective cell migration. *Nature Physics* 5, 426.

Valon, L., Marin-Llaurado, A., Wyatt, T., Charras, G., Trepat, X., 2017. Optogenetic control of cellular forces and mechanotransduction. *Nat Commun* 8, 14396.

Vasquez, C.G., Tworoger, M., Martin, A.C., 2014. Dynamic myosin phosphorylation regulates contractile pulses and tissue integrity during epithelial morphogenesis. *J Cell Biol* 206, 435-450.

Xie, S., Martin, A.C., 2015. Intracellular signalling and intercellular coupling coordinate heterogeneous contractile events to facilitate tissue folding. *Nat Commun* 6, 7161.

Xie, S., Mason, F.M., Martin, A.C., 2016. Loss of Galpha12/13 exacerbates apical area dependence of

actomyosin contractility. *Mol Biol Cell* 27, 3526-3536.